

PHASE TRANSITIONS OF IONIC LIQUIDS CONFINED IN CHARGED CARBON NANOPORES

Wissenschaftliche Arbeit zur Erlangung des Titels
MASTER OF SCIENCE

eingereicht von
Konstantin Schutjajew

Erstgutachterin
Prof. Dr. CHRISTINA ROTH

Zweitgutachter
Prof. Dr. Dr. h. c. MARKUS ANTONIETTI

24.09.2018

Danksagung

Ich bedanke mich herzlich bei Prof. Dr. Christina Roth and Prof. Dr. Dr. h.c. Markus Antonietti für die Übernahme des Gutachtens.

Herrn Prof. Antonietti gilt besonderer Dank für die Möglichkeit, meine Masterarbeit in seiner Abteilung anfertigen zu dürfen.

Bei Dr. Martin Oschatz und Runyu Yan bedanke ich mich für die tatkräftige Unterstützung und Anleitung sowie für die ergiebigen Diskussionen.

Ines Below-Lutz, Antje Völkel und Heike Runge danke ich für die Instandhaltung der Labore und die gewissenhaft durchgeführten Messungen.

Ich möchte mich weiterhin bei allen Mitgliedern der Abteilung Kolloidchemie für die herausragende Atmosphäre sowohl während als auch außerhalb der Arbeitszeiten bedanken. Mein Dank gilt auch meiner Familie und meinen Freunden, die stets zu mir gehalten haben und mich unterstützt haben.

Contents

List of Figures	iii
List of Tables	v
1. Introduction and Motivation	1
2. Theoretical Part	3
2.1. Room Temperature Ionic Liquids	3
2.2. Porous Carbon Materials	8
2.3. Electrochemical Energy Storage Technology	10
2.4. Kinetics of Phase Transitions	12
2.5. Electrochemical Methods	16
2.5.1. Interactions of Matter and Electricity	16
2.5.2. Double-Layer Models	18
2.5.3. Chronoamperometry	20
2.5.4. Cyclic Voltammetry	22
3. Experimental Part	29
3.1. Syntheses	29
3.1.1. Synthesis of Silica Template SBA-15	29
3.1.2. Synthesis of Ordered Mesoporous Carbon CMK-3	29
3.1.3. Synthesis of Salt Templated Carbons $\text{STC-}n$	30
3.1.4. Synthesis of Aerosil [®] Templated Carbons Aerosil [®] n - m	30
3.1.5. Synthesis of FeCl_3 Templated Carbon	30
3.2. Materials Characterization	31
3.2.1. Physisorption Experiments	31
3.2.2. Electrochemical Measurements	31
3.2.3. Differential Scanning Calorimetry	33
3.2.4. Thermal Analysis	33

3.2.5. X-ray Diffraction	33
3.2.6. Transmission Electron Microscopy	33
4. Results and discussion	35
4.1. Characterization of Carbon Materials	35
4.1.1. Salt-Templated Carbon and CMK-3	35
4.1.2. Aerosil [®] -Silica Templated Carbon	38
4.1.3. Iron(III)-Chloride Templated Carbon	43
4.2. Cyclic Voltammetry	45
4.2.1. Interaction of Ionic Liquids with Micropores	45
4.2.2. Structural Transitions at High Potentials	49
4.2.3. Influence of Lithium-Salts	56
4.2.4. Influence of Mesopore Diameter and Volume	58
4.2.5. Influence of Temperature	61
4.3. Differential Scanning Calorimetry	62
4.4. Chronoamperometry	65
4.5. Iron(III)-chloride templated carbon	68
5. Conclusion and Outlook	71
A. Appendix	73
Bibliography	77

List of Figures

2.1. Video-STM investigation of BMPTFSI at Au(111). ^[20]	5
2.2. Schematic of overscreening and crowding effects.	5
2.3. AFM images of EMImTFSI at a HOPG surface at OCP, +0.3 and -0.3 V. .	6
2.4. Different pore sizes of activated carbon.	8
2.5. Processes during the synthesis of salt templated carbons.	9
2.6. Schematic representation of the silica templating procedure. ^[28]	10
2.7. Different pore sizes of activated carbon.	10
2.8. Ragone plot of most of the current electrochemical energy storage devices. ^[2]	11
2.9. Growing nuclei of a new crystal phase. ^[30]	13
2.10. JMAK equation for different growth rates and dimensionalities.	15
2.11. Energy of an electron at the electrode and its interaction with the electrolyte.	17
2.12. Potential profile of the diffuse double layer. ^[34]	18
2.13. Scheme of a Stern-double layer and typical potential profile. ^[34]	19
2.14. Concentration profiles and current during a chronoamperometric experiment.	22
2.15. Potential vs. time during CV.	22
2.16. Reversible CV "template".	26
4.1. N ₂ physisorption measurements on CMK-3 and STCs at 77 K.	36
4.2. CO ₂ physisorption measurements on CMK-3 and STCs at 273 K.	37
4.3. Pore volumes in STCs and CMK-3 for different pore diameters.	38
4.4. N ₂ physisorption measurements on Aerosil [®] templated carbons at 77 K. . .	40
4.5. TEM-images of Aerosil [®] -templated carbons.	41
4.6. CO ₂ physisorption measurements on Aerosil [®] templated carbons at 273 K. .	42
4.7. N ₂ physisorption measurements on iron(III)-chloride templated carbons at 77 K.	43
4.8. TEM-images if iron(III)-chloride templated carbons.	44
4.9. Cyclic voltammograms of STCs and CMK-3 until 3.5 V.	46
4.10. Size comparison of RTIL ions under study.	47
4.11. Micropore-filling as an explanation of low-potential peaks in CV.	49

4.12. Cyclic voltammetry of CMK-3 in EMImBF ₄ at 2 mV s ⁻¹	49
4.13. Cyclic voltammograms of platinum in the investigated ionic liquids.	50
4.14. Comparison of CV-measurements on CMK-3 and platinum.	51
4.15. Cyclic voltammograms of STCs and CMK-3 until 5.0 V.	52
4.16. Cyclic voltammograms of CMK-3 in different concentrations of EMImBF ₄ . .	53
4.17. Cyclic voltammetry of CMK-3 in 0.5 mol l ⁻¹ TEABF ₄ in adiponitrile.	54
4.18. Cyclic voltammograms of STC-8 with and without salt addition.	57
4.19. Cyclic voltammograms of Aerosil [®] -carbons depending on mesoporosity. . . .	59
4.20. Cyclic voltammograms of Aerosil [®] -carbons depending on pore volume. . . .	60
4.21. Cyclic voltammetry on STCs and CMK-3 at r.t. and 60 °C.	62
4.22. DSC measurements of ionic liquids pure and confined in carbons.	63
4.23. Chronoamperometry of CMK-3 with shoulder during discharging.	66
4.24. Analysis of anomaly during relaxations step.	67
4.25. Cyclic voltammograms of FeTC-3 and FeTC-10 in EMImBF ₄ and EMImTFSI. .	69
A.1. XRD-patterns of investigated carbons.	73
A.2. Thermogravimetric analysis of investigated carbons.	73
A.3. TEM images of STCs.	74
A.4. CO ₂ physisorption measurements on FeTC at 273 K.	74
A.5. Cyclic voltammograms of Aerosil [®] -carbons in EMImBF ₄	74
A.6. Cyclic voltammograms of Aerosil [®] -carbons in BMImBF ₄	75

List of Tables

4.1. BET specific surface area (SSA), total pore volume (V_{tot}), and micro- and mesopore volumes from DFT (V_{micro} and V_{meso}) of the STCs and CMK-3.	36
4.2. BET specific surface area (SSA), total pore volume (V_{tot}), and micro- and mesopore volumes from DFT (V_{micro} and V_{meso}) of the Aerosil [®] templated carbon materials.	40
4.3. Volume of the micropores of Aerosil [®] carbon for different diameters.	42
4.4. BET specific surface area (SSA), total pore volume (V_{tot}), and micro- and mesopore volumes from DFT (V_{micro} and V_{meso}) of the iron(III)-chloride templated carbon materials.	44
4.5. Concentrations of EMImBF ₄ in the electrolyte in vol% and mol l ⁻¹ and charge stored in forward and backward peaks.	54
4.6. Overview over temperatures (in °C) and molar enthalpies (in kJ mol ⁻¹) of phase transitions observed in DSC.	64

1. Introduction and Motivation

As the society currently faces unprecedented problems such as global warming, environmental pollution and an increasingly precarious geopolitical situation, renewable energy sources are in the focus of attention as the only option for a sustainable and long-termed energy supply, ranging from low energy systems such as communication and individual mobility up to the electric grid mains. Unfortunately, environmentally clean energy sources, be it wind, solar or tidal, have the inconvenient property to be available only intermittently, so that excess energy must be stored temporarily to make up for times of calm air or a cloudy sky. To meet the needs of these rather large scale applications, methods like (photo)-electrolysis or redox-flow systems may be best suitable. Integration of renewable energy into daily life, especially for public and personal transportation or mobile devices poses different challenges. The development of lithium batteries has introduced a revolution on the market of microelectronics and even lithium battery powered vehicles are currently being marketed as part of the solution for today's problems of fossil fuel shortage and air pollution. However, lithium batteries, although wide spread and well elaborate, still have severe drawbacks. Safety concerns due to the propensity of lithium to violently react with air and moisture and environmental issues caused by exploitation of the resources needed for lithium batteries are key problems besides the inability to manage high power densities raise the demand for safer and more sustainable solutions.^[1]

The electrochemical double layer capacitor (EDLC) is a possible antipole to the lithium battery. The energy therein is traditionally stored via adsorption of the ions to the electrode surface and formation of an electric double layer. Those devices can be charged and discharged in a matter of seconds and offer high security and environmental sustainability, which is due to chemically stable carbon electrodes and mostly non-flammable electrolytes. In trade it can only reach a tenth of the energy density of lithium batteries. Great efforts have been invested in increasing the energy density of capacitors by tuning electrolytes, electrode materials or even coupling the double layer formation to reversible surface redox reactions, but the capacity of battery technology still remains out of reach.^[2]

More recently, the utilization of so called room-temperature ionic liquids (RTIL) as elec-

trolytes has opened a prospect to solve the problem of lacking energy density in EDLCs. This special class of "molten salts" not only has electrochemical stability windows (ECW) of above 4 V, which is beneficial as the energy stored in a capacitor generally depends quadratically on the applied voltage, but is also non-flammable and can be regarded as environmentally less damaging than common organic solvents. Most importantly, theoretical and experimental studies^[3–7] showed an anomalous behaviour of RTILs when confined in a porous carbon environment that can be attributed to direct interaction with the pores as well as to phase transitions of the RTIL itself, both leading to a change in coordination geometry and number and thereby to a change in surface charge. In the study of Yan et al.^[7] it was supposedly even possible to observe such processes in some particular cases even with cyclic voltammetry, which in turn promises a new pathway of energy storage that is energetically and mechanistically located in between of redox reactions and classical double layer formation.

Hence, the aim of this work is to provide evidence for the phenomenon of potential induced rearrangement of ionic liquids in porous carbons and especially to extend the previous research activity to other carbon/ionic liquid systems to systematically study the relationship between the structure of the electrode and its influence on the ability of the ionic liquid to undergo discussed phase transitions. Influence of temperature and electrolyte composition will be considered, as they are key factors that influence the intrinsic RTIL structure and energetics. Established synthesis methods and commercially available ionic liquids will be employed to specifically tune the porosity of the outcoming carbon, as they provide control over the product's properties at a constant quality. Cyclic voltammetry (CV) will be the technique of choice to study the ionic liquid rearrangements, as it has proved itself useful in previous work and is sensitive to electrochemical potential, i.e. the energetic properties of the process. This thesis states an attempt to understand, which prerequisites are necessary to induce a phase transition in ionic liquids, how to achieve them to appear independently of electrolyte decomposition to ensure reversibility and hopefully, to serve as a basis for future work on how to incorporate this alternative energy storage mechanisms into useful and sustainable technology.

2. Theoretical Part

2.1. Room Temperature Ionic Liquids

Room temperature ionic liquids are defined as molten salts, which are liquid below 298 K.^[8] The first example of an RTIL was ethylammonium nitrate, as demonstrated in 1914 by Paul Walden.^[9] He was also the first to deduce its purely ionic composition from its high conductivity. Syntheses of tetraalkylammonium chloroaluminates and chlorocuprates in the 1950s and 1960s extended the number and chemistry of RTILs.^[10] Chloro- and bromoaluminates had been extensively studied in the 1980s as solvents with catalytic properties in chemical synthesis and as battery electrolytes. However, these RTILs cannot be handled in the atmosphere, as already trace amounts of water lead to their decomposition under hydrogen halide formation.^[11] In the 1990s the discovery of air- and moisture-stable RTILs based on alkyl imidazolium, with most prominent examples 1-ethyl-3-methylimidazolium tetrafluoroborate (EMImBF₄) and bis(trifluoromethylsulfonyl)imide (EMImTFSI), opened the way to current widespread applications of RTILs in science and technology.^[12,13] Today a large variety of combinations of cations (alkylated derivatives of ammonium, pyrrolidinium or imidazolium) and anions (halides, pseudohalides and weakly coordinating anions such as BF₄⁻, PF₆⁻, OTf or Tf₂N⁻) are commercially available and their number is growing.^[8] Important properties such as polarity and liquid temperature range can be adjusted by introducing alkyl chains of different lengths or even functional groups into the ions. Additionally, RTILs can often be readily mixed with each other or organic solvents, so that for every application an RTIL based solvent system can be prepared. This diversity of potential ionic liquid combinations has coined them the term "designer solvents" and raised a lot of interest in their use as solvent in synthesis and catalysis.^[14]

As RTILs are essentially salt melts, they exhibit a number of typical features, such as low or negligible vapor pressure, high charge density, high ionic conductivity, and a wide range of thermal and electrochemical stability. The main features, that distinguish RTILs from ordinary salt melts and keep them liquid at room temperature, are the considerable amount of non-polar constituents, mainly located at the cation, the anisotropic distribution of the

electric charge over the ions and their rather low symmetry. The hydrophobic groups tend to arrange in non-polar regions, while anisotropy and asymmetry prevent the RTIL from adopting a stable crystal structure.^[4] On the other hand, exactly these properties cause the unique ordering of the RTIL in the liquid phase that marks them off even from closely related molten salts. Earlier it was believed that ionic liquids to a significant extent consist of ion pairs, held together either by coulomb forces or hydrogen bonds. This is justified by the evaporation of RTILs as ion pairs,^[15] early dielectric spectroscopy measurements, that report up to 8 % of ethylammonium nitrate ions being associated into pairs,^[16] as well as molecular orbital calculations, that suggested possible hydrogen bonding between anion and cation of imidazolium halides.^[17] Gebbie et al.^[18] used a surface force apparatus to measure force-distance relationships across an EMImTFSI interface, from which they calculated, that only less than 0.1 % of the ionic liquid is present as dissociated ions. However, more recent NMR and dielectric spectroscopy studies could not find signatures of ion pair formation in a series of RTIL cations including the imidazolium ion, indicating their extremely short lifetimes. Current theoretical simulations are in line with these observations and explain them by the fact, that each ion in an RTIL is surrounded by a shell of counterions in a way, that their charge is completely screened, known as coulombic ordering. The formation of ion pairs would thus disrupt this structure and is therefore unfavorable.^[8] Although the basic principle of coulomb ordering tends to be a bit simplifying and does not take into account specific ion geometries, its usage is still appropriate, because it is a very general concept and can serve as a good fundamental model to understand further interaction mechanisms of ionic liquids at solid interfaces, especially electrified and porous ones.

It can be easily imagined that the structure of an ionic liquid at a solid interface significantly differs from that of the bulk ionic liquid, even if no electric potential is applied, as the continuous solvation of the single ions is interrupted at the solid's surface, so that due to self-assembly properties of the ionic liquid its interface can be described as layered or lamellar in perpendicular direction to the surface plane.^[8] Interactions with electrified solids can be even more diverse. Microscopy methods including scanning tunneling (STM) and atomic force microscopy (AFM) are well established to study the behaviour of RTILs on atomically homogenous surfaces such as the Au(111) phase which can be reproduced easily and at a constant quality. The observations made in these studies include the change of the image upon application of a potential from an unordered or blurry picture to the appearance of patterned structures where the dimensions of the repeating units match molecular sizes.^[19] Wen et al.^[20] performed video-STM studies on the said Au(111) surface using butyl-methylpyrrolidinium bis(trifluoromethylsulfonyl)imide (BMPTFSI) and were able to measure po-

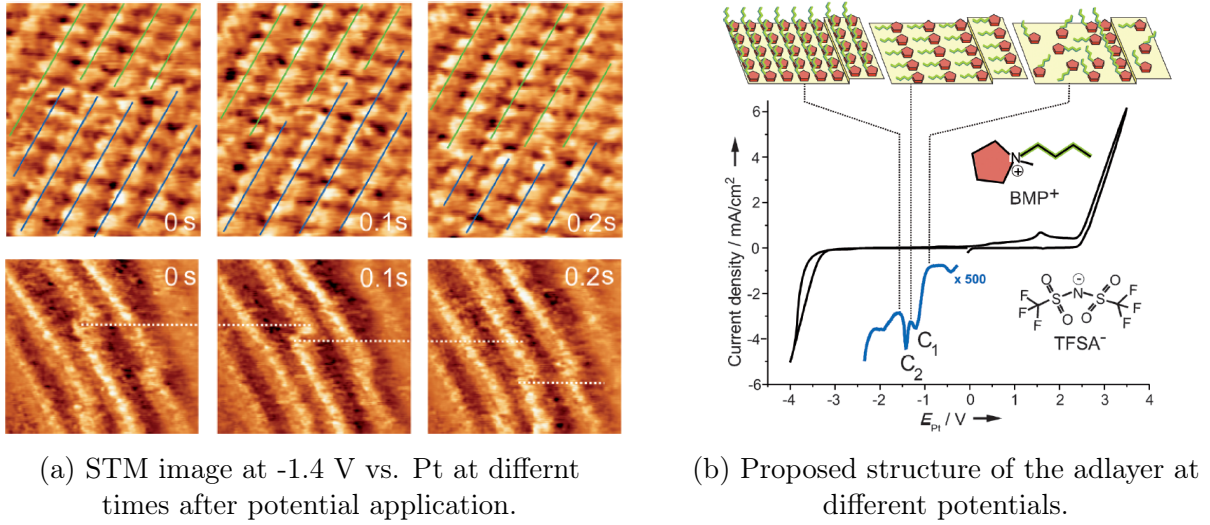


Figure 2.1.: Video-STM investigation of BMPTFSI at Au(111).^[20]

tential dependent adlayer structures where the molecular conformation of the BMP^+ ion adapted to maximize the ion density (figure 2.1). While this study can shed some light on the RTIL adlayer structure, it is not very close to the situation at real electrodes, as it deals with only one monolayer of adsorbed ionic liquid, meaning that the anion/cation ratio within the layer is exactly one. Moreover, an investigation of only the first layer of ions cannot take into account effects that this layer has on the constitution of the subsequently adsorbed ions.

Important theoretical work on the structure of ionic liquids in the perpendicular direction to the electrode was carried out by Bazant et al.^[21] The group used the Landau-Ginzburg approach to calculate the charge density with respect to the distance from the electrode as a function of the applied potential and by that provided a phenomenological description of experimental and simulation data. Application of a comparably low potential as seen in figure 2.2 at $10 \frac{kT}{e}$ (translates to approx. 0.26 V at room temperature) leads to the construction of a tightly adsorbed layer of ions. Due to correlation effects arising from intermolecular interactions, this layer overcompensates the charge introduced by the electrode surface, so that the following ion layer is richer in counter ions. This happens until charge neutrality is reached and causes a lamellar and periodic perpendicular structure of the ionic liquid. The effect is called *overscreening*.

Further increase of potential leads to the growth of the first assembly of ions, charged oppo-

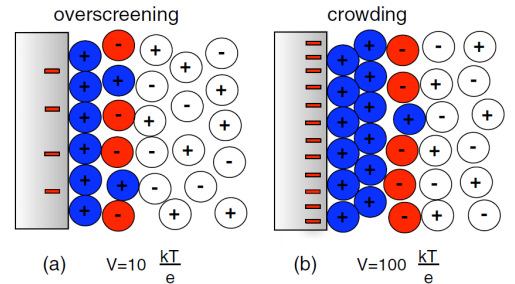


Figure 2.2.: Schematic of overscreening and crowding effects.

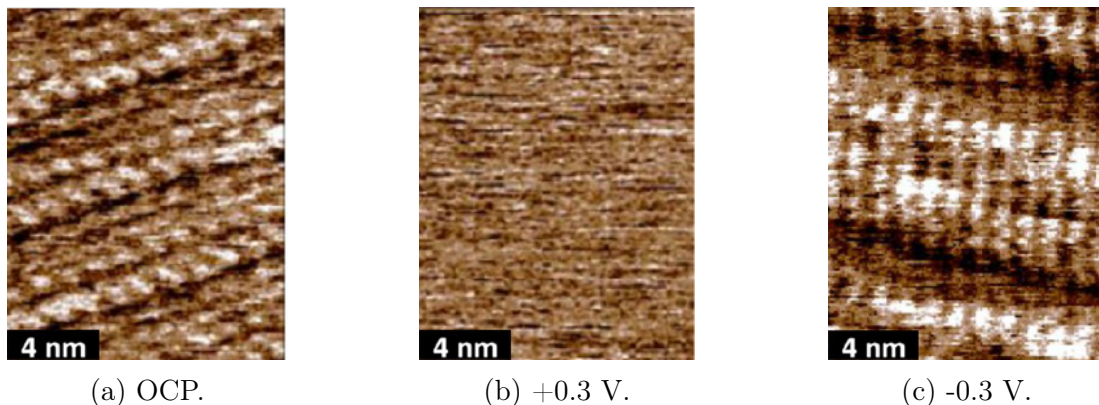


Figure 2.3.: AFM images of EMImTFSI at a HOPG surface at OCP, +0.3 and -0.3 V, with unresolved image at positive and larger ion rows at negative potentials.^[22]

sitely to the electrode and is entitled *crowding* (figure 2.2 at $100 \frac{kT}{e} \approx 2.6V$). Analogously to the concept of coulombic ordering these basic models of the electrochemical double layer in ionic liquids are potentially oversimplified and must be adjusted to the given combination of RTIL and electrode surface. In an AFM investigation of EMImTFSI at a highly ordered pyrolytic graphite (HOPG) surface Elbourne et al. observed potential induced multilayer structuring of RTIL.^[22] The authors found double rows consisting of more or less mobile ions present at open circuit potential (OCP), that disappeared at +0.3 V vs reference, from which it was concluded that the less mobile phase consists of BMIm⁺ cations. At more negative potential the cation rows were densified and enlarged. The more compliant anion phase was less well resolved, indicating a facile response of the electrochemical double layer to potential differences (figure 2.3).

However, under conditions as present in real electrochemical devices one will never be able to describe the system by using an idealized plane surface model, as porous materials are applied in the most cases. It is a known fact that gases and liquids behave significantly different under confinement in pores and RTILs are not an exception. The group of Kiyohara et al.^[3] modelled an electrochemical cell by means of molecular dynamics simulations with pore diameters of the 1.1 to 20 fold of an ion diameter and calculated the surface charge density for an increasing and subsequently decreasing potential applied, resembling a cyclic voltammetry experiment. They assumed the forces between ions and pore to be attractive and counterbalanced by the repulsive forces of the similarly charged ions. The investigation resulted in a constantly ramping charge density for rather large pores (minimum twofold ion diameter) and a jumpwise rise in charge density after a certain potential was surpassed, if pore diameter was set to 1.1 times that of the ion. On the backward scan the charge

density was neutralized not at the same, but at a lower potential than that of the charge jump, so that a hysteresis was observed. The origin of this feature was identified as a first order surface phase transition of the RTIL. The study thereby explained earlier experimental findings of Largeot et al.,^[6] who investigated electrochemical double layer capacitors with EMImTFSI as electrolyte and electrodes of different pore sizes and found an exceptionally high capacitance if the pore width was just above RTIL ion diameter.

The nature of this phase transition could be elucidated by Futamura et al.^[5] in their investigation of EMImTFSI and EMImBF₄ at microporous carbon materials with pore diameters of 0.7 and 1.0 nm through simulation assisted small angle X-ray scattering experiments. They were able to show that monolayer confinement could break the otherwise present coulombic ordering of the RTIL and lead to co-ion pair formation, where the excess charge density that is introduced by the close proximity of coions was supposed to be balanced by mirror charges in the electrode that corresponds exactly to the energy necessary to overcome the coulombic repulsion. The population of EMIm⁺ cations and respective anions in the first coordination sphere around the anion was used as a measure for the degree of coulombic ordering. At 0 V in the bulk electrolyte the coordination shell consisted of 95 % cations, while under confinement the number increased to 23 %. An applied potential facilitated this transition, as a higher fraction of other anions was then reported around the center anion (34 %). The presence and contribution of phase transitions in RTILs under micropore confinement is therefore already well established theoretically as well as experimentally so that finding a way into application for energy storage must be the next logical step.

Yan et al.^[7] made a number of intriguing observations when they studied a series of micro- and mesoporous carbons that raised questions to the mechanisms of energy storage in electrochemical double layer capacitors that to that point seemed well understood and also indicated the presence of additional mechanisms of interaction. The carbon materials included one purely microporous sample STC-1 and carbons with an gradually increasing mesopore volume (STC-2 to 16, STC = salt templated carbon, numbers describe porogen/carbon source ratio). Introduction of even a small amount of mesopores increased the gravimetric capacitance of the cell drastically, while the specific surface area, which from the point of view of the basic condensator equations is considered often the key criterion for the performance of a capacitor, only increased by about 15 %. Further, a rough comparison of the surface area available in the cell to the amount and size of the ions suggested a densely packed ion-layer, while the measured gravimetric capacitance would require an unrealistically high double layer compression beyond physically reasonable values. A signal at high potentials (>3 V) in the cyclic voltammograms of those carbons, too early in onset potential and too reversible

to be ascribed to the electrolyte decomposition, served as another indication to postulate an alternative process employable for energy storage in RTIL based electrochemical double layer capacitors. Lai et al.^[23] incorporated nitrogen and sulphur atoms into CMK-3 carbon and deposited manganese(IV)-oxide on it, thereby decreasing pore volume and surface area and achieved higher capacitance values than for the untreated CMK-3. These results together plead towards a process that includes an order/disorder transition in the case that the pore geometry and surface properties meet the conditions to facilitate this processes. Structural transitions like the ones suggested by the described study could have the tempting advantage of being highly reversible while occurring at high molar enthalpies and therefore enhance the energy density of double layer capacitors to finally close the gap to established energy storage technologies, if only the requirements for the processes to occur could be found and rationalized and at the same time the electrolyte degradation occurring in parallel could be suppressed.

2.2. Porous Carbon Materials

Carbon is found in the fourth group of the second row of the periodic table and its ability to form up to four bonds with most of the other elements gives rise to countless compounds and modifications, be it in organic or inorganic chemistry. As an element it occurs in two allotropes that are the basis for a variety of derived structures with unique properties and applications.

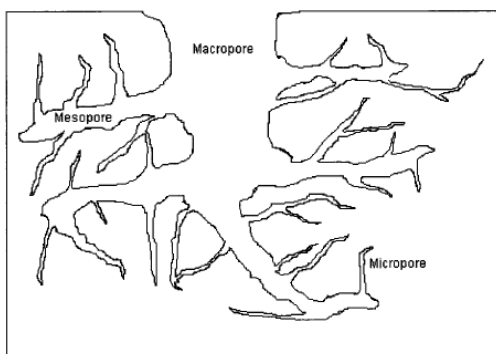


Figure 2.4.: Different pore sizes of activated carbon.

While diamond is the hardest material found in nature and an electrical insulator, graphite is one of the softest substances, a very good electrical, and the best thermal conductor known due to its structure of sp^2 hybridized atoms connected in planes with a delocalized π -electron system. Monolayers (graphene) or cylindrically arranged layers of graphite (carbon nanorods) can be artificially produced and have found application in science and technology.^[24] A large and industrially important class of carbons are the so

called activated carbons that, although on an atomic scale disordered, have some interesting structural properties on a higher level, the probably most important being porosity. Porous carbons can be prepared in a large scale in manifold ways, starting from a variety of precursors including biological waste, tars or pitches. Heat treatment as well as an activation

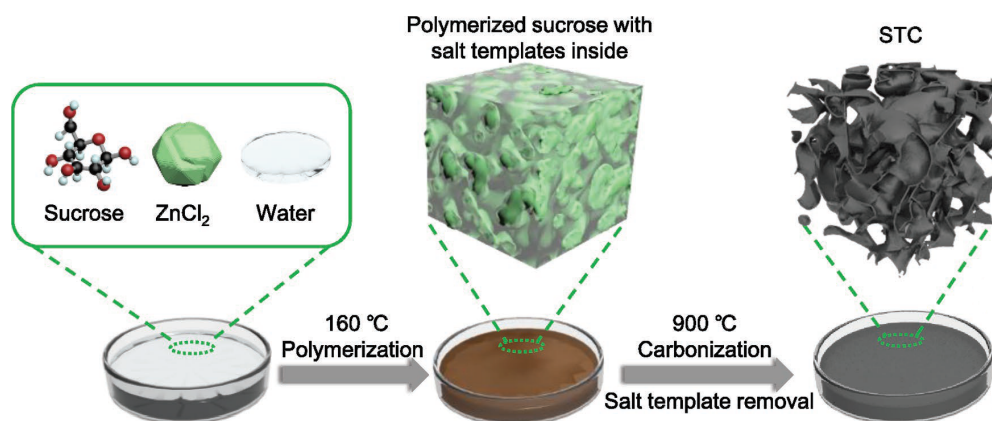


Figure 2.5.: Schematic representation of the processes during the synthesis of salt templated carbons.^[7]

process is required, to introduce pores into the material, the activation processes are divided into physical ones, i.e. reaction with oxidizing gases (CO_2 , H_2O) and chemical ones, where H_3PO_4 and KOH are important reactants. The resulting pore structure is in those cases mostly not very uniform and mainly micropores that are too small for the interaction with host molecules are generated. Introduction of larger meso- or even macropores (figure 2.4 requires alternative methods. Two important approaches in the synthesis of especially mesoporous carbons that will be also applied during this work include the generation of pores by means of low boiling salts^[7,25] and the hard templating with silica precursors.^[26,27]

In the first method a carbon source, here sucrose, is dissolved together with ZnCl_2 in water and in the first step left at temperatures of max. 160 °C under atmospheric conditions. During this treatment, the sucrose undergoes a polycondensation under acid catalysis and forms a polymer around the solid ZnCl_2 . The pore structure is preformed at this point and can be tuned by adjusting the amount of ZnCl_2 added. Carbonization at 900 °C transforms the polymer into a carbon material and causes partial evaporation of ZnCl_2 , of which residues are washed out with hydrochloric acid subsequently. The resulting substance is denoted as salt-templated carbon and characterized by a significant micropore volume of relatively large micropores (≈ 0.8 nm) almost irrespective of the ZnCl_2 amount added and a variable amount of mesopores of narrow size distribution ranging from 2 to 4 nm.

The introduction of larger mesopores at narrow size distribution is not easy to achieve using the salt templating approach and the formerly described method is a rather exceptional example. Therefore it is more established to use the silica hard templating technique as it allows a precise definition of pore geometry of the carbon, which ultimately depends on the shape of the silica template particles. After removal of the silica a carbon material

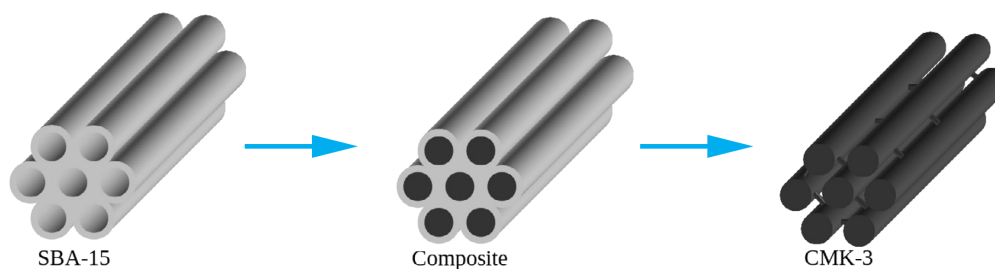


Figure 2.6.: Schematic representation of the silica templating procedure.^[28]

remains, that is an exact negative replica of the template. A famous example for a silica templated carbon is the mesoporous CMK-3 produced from the ordered silica molecular sieve SBA-15 (figure 2.6).^[26] During synthesis the template is impregnated with an acidic sucrose solution, so that the sucrose fills the pores of the silica completely and polymerizes inside of them. The sample is subjected to the same polymerization and carbonization conditions as the salt templated carbon above and the silica is removed by washing either in sodium hydroxide or hydrofluoric acid solutions. The resulting carbon possesses mesopores with a very narrow size distribution and only a negligible amount of active micropores.

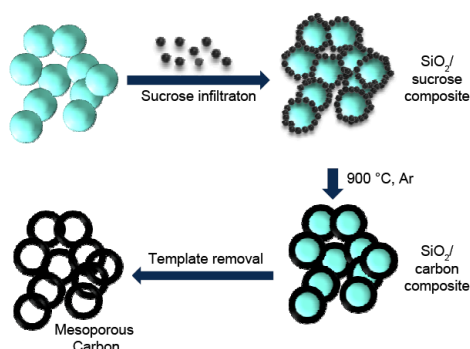


Figure 2.7.: Different pore sizes of activated carbon.

Efficient control over the pore size can also be achieved by using industrial silica template Aerosil® instead of the elaborate SBA-15 precursor.^[27] Those globular particles of defined diameters can be employed in a similar synthetic procedure to yield mesoporous carbon materials where the pore size is controllable by the silica particle size and is usually larger than in carbons obtained from SBA-15 templation. It is due to the formation of secondary and primary particles through aggregation and agglomeration, that al-

though the carbon is derived from a spherical template, the pore shape is more a slit- or channel-like one than a spherical one.

2.3. Electrochemical Energy Storage Technology

The demand for energy storage technologies is constantly increasing. Batteries, mostly based on Lithium, have occupied the market for low-power applications, such as mobile consumer electronics, owing to their high energy-density in the order of magnitude of 100 Wh/kg.

However, the charging and discharging rate is limited by the kinetics of the chemical reaction involved in energy storage and therefore batteries are not suitable for applications, in which high power densities are required. In contrast, the energy storage mechanism of an electric capacitor relies on the formation of an electrochemical double-layer, a very fast and reversible, purely physical process. The well established special class of capacitors termed electrochemical double layer capacitor (EDLC) is capable of handling about the ten-fold power density of a battery but only about a tenth of the energy density. Additionally, they are able to survive by orders of magnitudes more charge/discharge cycles than a typical battery.^[2]

To overview the relationship between energy storage capacity and power density, it is convenient to classify the energy storage technology for example by means of plotting the specific energy against the specific power in a so called Ragone plot as shown in figure 2.8. It is obvious from this graph that supercapacitors represent a bridge between two extremes, namely the battery¹, capable of handling high amounts of energy, but only over a rather long period of time and on the other hand film or electrolytic capacitors that can deal with high power bursts but are unable to store much energy. Supercapacitors basically still rely on the buildup of an electrochemical double layer, but it is attempted to overcome the energy density limitation in different approaches;

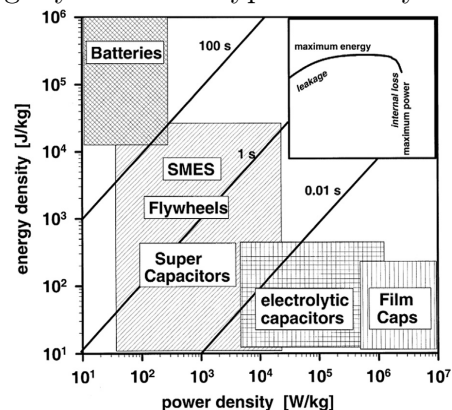


Figure 2.8.: Ragone plot of most of the current electrochemical energy storage devices.^[2]

1. By increasing the electrode surface area (electrochemical double layer capacitor, EDLC).^[29] The electrodes are then usually comprised of microporous carbon, possible electrolytes include aqueous, organic and ionic liquid based ones. Aqueous electrolytes have of course the highest conductivity at the cost of a narrow electrochemical window of approx. 1 V, while organic solutions are less conductive but can be run at up to 3 V in the case of acetonitrile. Ionic liquids have even larger electrochemical windows and are at the same time well conductive. The operating voltage is a crucial factor for an EDLC, as the amount of energy stored in such a cell depends quadratically on the potential difference.
2. Introducing surface functional groups that undergo reversible reactions to store energy (pseudocapacitor).^[2] Such pseudocapacitors can store energies exceeding those of

¹Redox-flow batteries and fuel cells basically surpass batteries in specific energy and usually have even lower specific powers, but will not be discussed here.

EDLCs, but redox reactions always bear the danger of a faster degradation of the cell, which in the worst case can lead to failure of operation of the cell.

3. Combining a high surface area and surface functional groups to build a hybrid supercapacitor can yield a device, that has an performance between those of an EDLC and a pseudocapacitor.

Potential fields of application for a supercapacitor would be for example the recapturing of energy, that is released during the breaking process of vehicles. The high amount of energy occuring in a short period of time requires the storage system to be able to convert it rapidly. Supercapacitors are perfectly suited for this application and at the current state could be combined with a battery to increase the energy storage capacity. If the specific energy could be increased, for example as discussed in previous sections, they could also become a standalone solution or even could be applied in larger scale systems.

2.4. Kinetics of Phase Transitions

As phase transitions will be an important topic throughout this work, their thermodynamic fundamentals have to be briefly reviewed. The common theoretic model for phase transformations which is widely accepted and has found application in fields including crystal structure rearrangement of metals or surface alterations of thin films is the nucleation and growth theory founded by the mathematicians and metallurgists W. A. Johnson, R. F. Mehl, M. Avrami and A. N. Kolmogorov.^[30–33] When a phase A is e.g. supercooled, the phase transition begins not homogenously throughout the entire volume, but rather at small crystal nuclei of the under given conditions more stable phase B. The size of the nuclei is dependent on temperature and concentration and upon reaching a critical size, that is given by the equilibrium between crystal lattice energy and surface tension, they begin to grow at a constant rate until the phase A is completely transformed to phase B or they impinge upon each other. The transformation of a phase A to the phase B can be mathematically described, following some basic assumptions:

1. There are "germ nuclei" of the new phase present in the old phase. Their number per unit volume is denoted as \bar{N} and can be controlled by temperature and time of heating.
2. The number of germ nuclei at a time t , $N \equiv \bar{N}$ can decay in two ways: a) it can become an active growth nucleus with the probability of n , or b) it can be incorporated into another growing new phase.

3. Growth ceases as soon as two grains of the new phase overlap each other.
4. The ratio of the growth rate of a nucleus G and activation probability n is constant within the isokinetic range of the phase: $\frac{G}{n} \equiv \alpha$

If overlapping of two grains of a new phase leads to the termination of growth, then the nonoverlapped volume v' of a crystal can be considered as untransformed. Then it holds, that the ratio of nonoverlapped volume v' to the extended volume v_{1ex} , which is the volume of the new crystal phase including the volume of the overlapping regions of the single grains, if they were to grow infinitely (dashed areas in figure 2.9), is equal to the density of untransformed matter $(1 - V)$, as expressed in equation 2.1.

$$\frac{v'}{v_{1ex}} = 1 - V \quad (2.1)$$

For this equation to be valid, it must hold for any randomly selected nucleus throughout the crystal. However, this expression was subject to the restriction, that only nonoverlapped volume is considered. Complete randomness can be restored, by taking into account those grains that would have been transformed into growth nuclei, if they would not have been ingested by another grain. Including these "phantom grains" into the treatment, one can state the following expression for the extended volume density V_{1ex} :

$$V_{1ex} = \overline{N} \int_0^\tau e^{-z} v(r, z) dz \quad (2.2)$$

with:

z : time

v : transformed volume, where $v(r, z) \equiv v_{1ex}(r, z)$

τ : characteristic time scale, $ndt = d\tau$

Equation 2.1 can now be applied to the nonoverlapped volume of the grain. Summing over all volumes, including the phantom ones one arrives at:

$$\frac{V_1'}{V_{1ex}} = \overline{N} \int_0^\tau e^{-z} v(r, z) dz \quad (2.3)$$

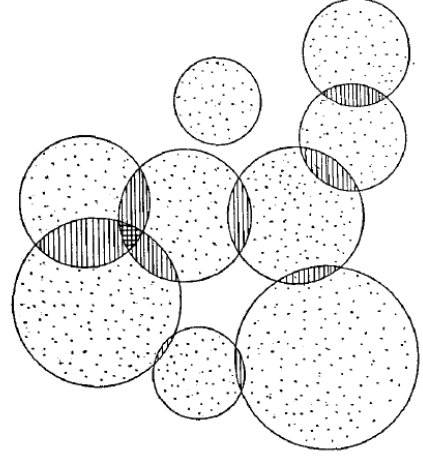


Figure 2.9.: Growing nuclei of a new crystal phase.^[30]

If the new structure is very fine grained, one can invoke as an approximation, that $V'_1 = V$ and get:

$$\frac{V}{(1-V)} = V_{1ex} \quad (2.4)$$

This approximation holds only for fine grained phases, within the isokinetic and isothermal assumptions and can be solved for different growth geometries, that can in turn be simplified to achieve an equation that contains a rate constant and a factor k that describes the dimensionality of the growth process.

$$\frac{V}{(1-V)} = Bt^k \quad (2.5)$$

with:

B : rate constant

k : factor describing dimensionality of growth, $k = D + 1$

If a more general and precise expression is needed, one must consider instead of the volumes of the of the grain regions their increments dv_1 and dv_{1ex} . Using the same reasoning as in the beginning and taking the relative densities of the grains one arrives at a differential equation:

$$\frac{dV}{dV_{1ex}} = 1 - V \quad (2.6)$$

Integration and rearrangement yields an expression known as the Johnson-Mehl-Avrami-Kolmogorov, or after their initials, JMAK equation:

$$V = 1 - \exp(-V_{1ex}) = 1 - \exp(-Bt^k) \quad (2.7)$$

From this equation one can then assess the rate constant and growth dimensionality of a phase transition process. As can be taken from figure 2.10, which shows the influence of transition rate B and JMAK factor k on the resulting curve. The JMAK factor has a much stronger impact on the time needed to achieve a full conversion of phase A to B. Also B and k values have different influences on the curvature of the graph, so that fitting experimental data is expected to be reliable.

The theory has been largely extended over time and can actually deliver even more information about symmetry or the rate determining steps. But for such a precise treatment data from more accurate sources is necessary than will be available from electrochemical

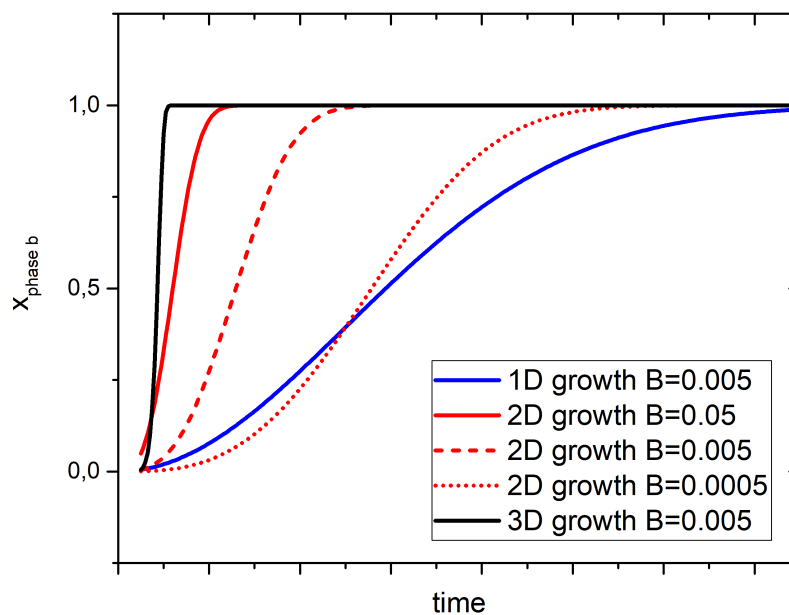


Figure 2.10.: JMAK equation plotted for 1D, 2D and 3D growth with rates of 0.05, 0.005 and 0.0005 for 2D growth.

measurements, as especially cyclic voltammetry data is not unambiguous in terms of distinguishing between redox reactions and other processes and not always signals can be definitely assigned to one specific process.

2.5. Electrochemical Methods

2.5.1. Interactions of Matter and Electricity

An electrochemical cell in its simplest form is built up of two electrodes that serve as electron conductors, connected over a chemical phase that is ion conducting, the electrolyte. The circuit is closed externally, by connecting the electrodes over an electron conductive material (e.g. copper cable), but usually in addition a potentiostat is found inbetween, that controls the measurement parameters during the experiment. An electrical potential can generally be measured between the electrodes, when a process at the electrode/electrolyte interface is taking place or vice versa a voltage can be applied externally to induce one. The nature of these interfacial processes should be discussed later. Microscopically, the role of the voltage is to change the electrochemical potential of the electrons in the electrode, which is also known as the *Fermi energy* E_F and can be translated into a free energy with the unit kJ mol^{-1} by considering the charge of a mole of electrons.

$$\Delta G = -FE \quad (2.8)$$

The Fermi-energy is defined as the energy, at which the occupation probability in the distribution of electrons over the energy levels of the Fermi-Dirac distribution equals 0.5, which for the electrode depends on the work function of the electrode material and for the electrolyte on the electrochemical potentials of the relevant species. The equilibrium condition for an inert electrode in direct contact with the electrolyte is that the phases' Fermi energies are equal, meaning that at the beginning of a reaction, when the equilibrium condition is not met, higher energy electrons will cross the junction, until equilibrium is reached.

$$E_F^M = E_F^s \quad (2.9)$$

The electric potential applied can therefore influence the state of the electrochemical system, as shown in figure 2.11, where a reduction and an oxidation reaction are schematically represented. Making the potential more negative, one raises the energy of the electron until it matches that of the unoccupied orbital of the species present in the electrolyte and the electron is transferred across the interface. Oppositely, by shifting the potential of the electron to more positive values, one reduces its energy and an electron from the electrolyte can find a more favorable state at the electrode. The occurrence of electrode reactions is observed as an electric current and can encompass by far more processes, than simple redox reactions that were chosen in the example for illustration purposes.

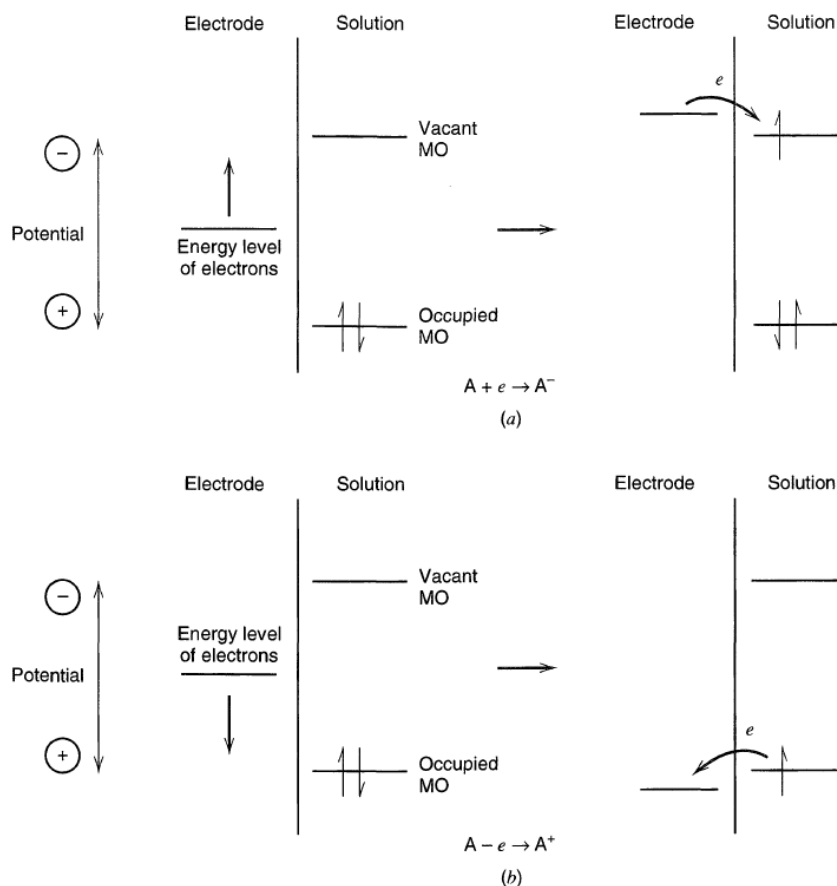


Figure 2.11.: Energy of an electron at the electrode and its interaction with the electrolyte. (a) for a reduction, (b) for an oxidation reaction.^[34]

Several types of processes can take place at an electrode even simultaneously and have been classified into faradaic and non-faradaic ones. Faradaic processes are defined as those, that follow Faradays equivalence law, meaning that the current recorded is connected proportionally over the number of electrons exchanged per formula conversion to the rate of a chemical reaction in the system. Faradaic processes are characterized by electrons, crossing the electrode/electrolyte interface, usually being chemical redox reactions. Following this argumentation, during non-faradaic processes electrons are not exchanged between electrode and electrolyte and include adsorption and desorption processes as well as all kinds of changes of electrode area and solution composition, but most important is the polarization of the electrode and the herewith connected capacitive current flow during electrochemical double layer formation, for which several models have been developed.^[34]

2.5.2. Double-Layer Models

The simplest model is named Helmholtz model after its inventor and views the electrode as ideally polarizeable and electrically conductive, so that the charge on the electrode is located solely at the surface. The charge is counter-balanced by the ions of the electrolyte that can adsorb to the electrode only in one layer and their charge can come as close as the ion radius. The electrolyte itself is a dilute solution of ions in a dielectric medium, i.e. the solvent. The electrons and the ions align at the electrode/electrolyte junction and oppose each other in a structure called double layer. In fact, this model can be described mathematically like a parallel-plate capacitor, so that the capacitor's basic equation applies, where σ is the differential charge density with respect to area, d the distance and U is the voltage drop between the plates.

$$\sigma = \frac{\epsilon\epsilon_0}{d}U \quad (2.10)$$

The potential gradient between electrode and electrolyte is therefore linear. The Helmholtz layer is also referred to as rigid double layer, as movement of the adsorbed ions is not considered. This is one of the weaknesses of the model, since the thermal motion of the ions adjacent to the bulk electrolyte disturbs the ordered double layer and can lead to significant discrepancy between theory and experiment. Furthermore, the radius of the ions is often underestimated, as solvation is neglected in the first approximation. Therefore one often uses the hydrodynamic or effective radius, which takes the ions' solvation shell into consideration.

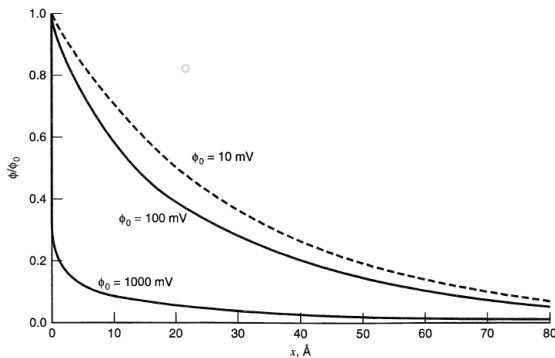


Figure 2.12.: Potential profile of the diffuse double layer.^[34]

In an attempt to overcome the disadvantages of the Helmholtz model, Gouy and Chapman proposed their theory. In a statistical-mechanical approach, they regarded ions as point charges and divided the electrolyte perpendicularly to the electrode surface into layers of thickness dx , so that a Boltzmann term could be employed and by that included the thermal movement, that randomizes the order of adsorbed ions. In figure 2.12 potential profiles of a diffuse double layer

are calculated according to the Gouy-Chapman model for electrode polarizations of 10, 100 and 1000 mV. They show a gradual decrease of potential for relatively low electrode voltages (10 and 100 mV) and an unrealistically dense double layer for the highest calculated polarization, so that the potential profile is covered by the ordinate. This is due to the assumption

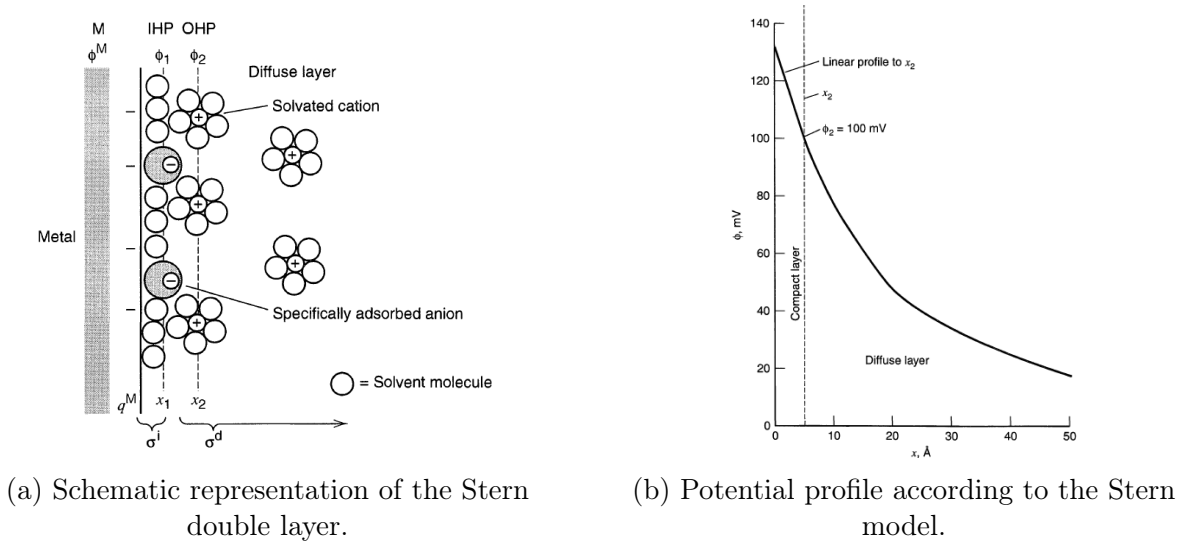


Figure 2.13.: Scheme of a Stern-double layer and typical potential profile.^[34]

of ions as point charges, that can come infinitesimally close to the electrode surface. The same happens for very concentrated electrolytes in the order of magnitude between 0.1 and 1.0 mol l⁻¹, so that the model fails for high electrolyte concentrations and high polarization and is therefore unsuitable especially for ionic liquid electrolytes due to the absence of solvent. However, the potential reaching into the bulk of the electrolyte is, although estimated as too long ranging compared to experiment, a valuable achievement of the model.

The Stern model makes up for the drawbacks and combines the strengths of both of the above mentioned models, by using the Helmholtz rigid double layer in the proximity of the electrode and the diffuse Gouy-Chapman double layer for the electrolyte closer to the bulk. It takes into account the finite size of the ions, specific adsorption, and for dilute electrolytes a layer of solvent molecules can be modelled. Closest to the electrode surface is the inner Helmholtz plane, that is made up of specifically adsorbed ions or molecules. This layer is defined to be rigid and its thickness equals to the distance of the ions' charge centers (x_1). Solvated ions from the electrolyte cannot penetrate the inner Helmholtz plane and therefore adsorb in a subsequent layer, the outer Helmholtz plane, that propagates into the bulk exactly as far as the hydrodynamic radius of the adsorbing ion x_2 (figure 2.13a). In the potential profile, the electrolyte is described with the Helmholtz model in the region of $0 \leq x \leq x_2$ and for $x \geq x_2$ using the Gouy-Chapman model as can be seen in figure 2.13b. The advantage is not that significant in the presented example, as potential and electrolyte concentration are not too high and would fit the diffuse double layer model well, but becomes obvious, when treating cases like the one shown in figure 2.12 at 1000 mV potential. Introducing a

plane of closest approach, as done in the Stern model, would yield a better description of the reality. Although more sophisticated models, that include the type of solvent, metal or even reactions in the inner Helmholtz plane have been developed, the Stern model broadly remains the standard model, as it combines sufficiently precise predictions while remaining well comprehensible.^[34] It should be stressed at this point, that the described double layer models as well as the following theoretical treatment of the standard electrochemical methods are assuming 1) a solvent based electrolyte, where the electroactive species is surrounded by a dielectric and 2) a plane electrode surface (in the first approach). These conditions do not hold (or only in a limited range) in the investigated case of ionic liquids in porous environment. It should be kept in mind that the ionic liquid is not a solution, therefore the dielectric constant is not easily available, and furthermore the diffusion of single components is very limited or even hindered due to the IL's intrinsic coulombic ordering.^[35]

2.5.3. Chronoamperometry

In Chronoamperometry a constant potential is applied to the cell and its current response is measured as a function of time (hence the name). It is common practice in the study of redox reactions, to first apply a voltage, at which no faradaic reaction takes place, E_1 and then jump to a potential E_2 , where the educt species cannot exist at the electrode surface any longer and thus reacts immediately to the product. It does not matter, how fast or slow the rate of the reaction is, as the potential can always be set high enough, to fulfill the condition of a purely mass transport limited reaction. For a mathematical treatment one starts with solving the diffusion equation for a general electrode reaction of the type:



with:

Red: Reduced species.

Ox: Oxidized species.

To arrive at expressions for the current-time relationship and a concentration profile of the system, one starts with Fick's second law under the boundary conditions that at the beginning of the reaction the concentration of reduced species is equal throughout the electrolyte (1), the concentration in the bulk C_{Red}^* remains constant (2), and that the concentration of reduced species is zero at all times besides $t = 0$ (3), (equation 2.12).

$$\frac{\partial C_{Red}(x, t)}{\partial t} = D_{Red} \frac{\partial^2 C_{Red}(x, t)}{\partial x^2} \quad (2.12)$$

with boundary conditions:

$$\begin{aligned} (1) \quad & C_{Red}(x, 0) = C_{Red}^* \\ (2) \quad & \lim_{x \rightarrow \infty} C_{Red}(x, t) = C_{Red}^* \\ (3) \quad & C_{Red}(0, t) = 0 \quad (\text{for } t > 0) \end{aligned}$$

Solving this differential equation by means of Laplace transformation under the chosen boundary conditions yields a formulation of the concentration profile during a chronoamperometric experiment:

$$C_{Red}(x, t) = C_{Red}^* \operatorname{erf} \left[\frac{x}{2(D_{Red}t)^{1/2}} \right] \quad (2.13)$$

The current can be expressed, by considering Ficks first diffusion law for the mass flux $J_{Red}(0, t)$:

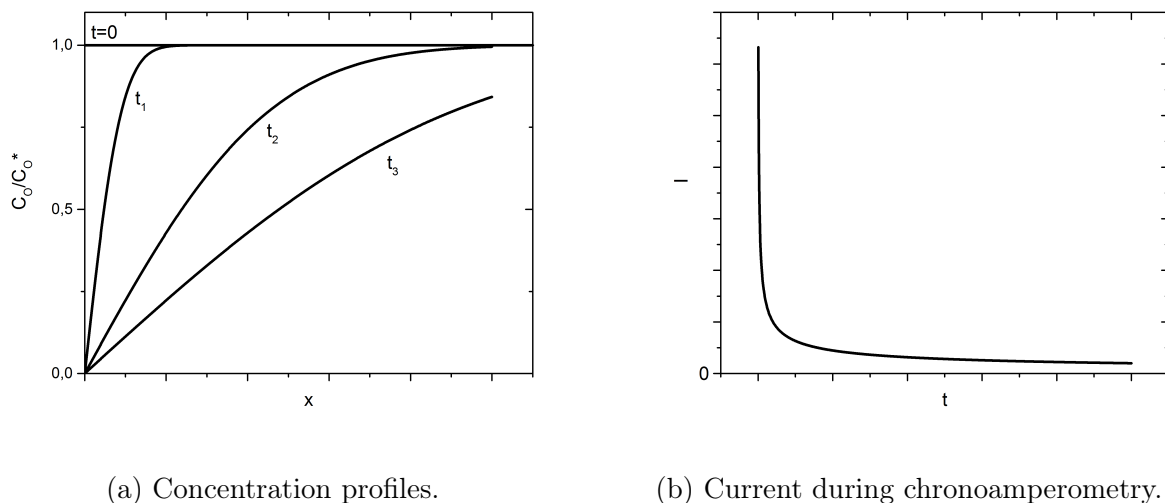
$$- J_{Red}(0, t) = \frac{I(t)}{nFA} = D_{Red} \left[\frac{\partial C_{Red}(0x, t)}{\partial x} \right]_{x=0} \quad (2.14)$$

After inverse Laplace transformation and rearrangement a fundamental electrochemical relationship for the temporal evolution of the electric current during a constant potential experiment is found and called Cottrell-equation after its inventor:

$$I(t) = \frac{nFAD_{Red}^{1/2}C_{Red}^*}{\pi^{1/2}t^{1/2}} \quad (2.15)$$

The implications of these results are represented graphically in figure 2.14. At $t = 0$ the concentration equals to that of the bulk, as required by the boundary condition (1). With ongoing time, the concentration at the electrode depletes more and more and the concentration gradient expands into the bulk solution. The current response (figure 2.14b) can be concluded from the concentration profiles; at first an infinitely high current sets in as a consequence of the immediate depletion of surface concentration of Red. The current levels off with progressing time and approaches zero for infinitely long reaction times.

However, there is always a non-faradaic current found in addition to the redox current, which arises from the formation of an electrochemical double layer which even outweighs the faradaic in supercapacitors. The capacitive current can be simply and accurately de-



(a) Concentration profiles.

(b) Current during chronoamperometry.

Figure 2.14.: Concentration profiles for times $t = 0$ and $t_1 < t_2 < t_3$ (a), and current during a chronoamperometric experiment.

scribed with a declining exponential function as in a conventional electronic component. The product RC can be measured and is known as the time constant of the cell.^[34]

$$I = I_0 \exp\left(-\frac{t}{RC}\right) \quad (2.16)$$

2.5.4. Cyclic Voltammetry

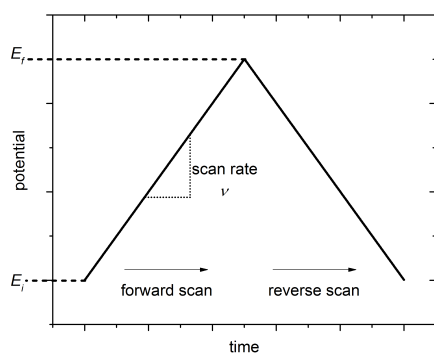


Figure 2.15.: Potential vs. time during CV.

While in chronoamperometry the cell was subjected to a fixed potential, in cyclic voltammetry the potential is swept from an initial value E_i , at which no faradaic reaction occurs, to the redox potential of the reaction and even beyond until it is reversed at E_f . The voltage is ramped at a constant scan rate ν , so that the potential-time profile from figure 2.15 is achieved. Again, one has to solve the diffusion equations, to obtain the current response curve, but in contrast to chronoamperometry, where is simply assumed,

that the concentration of *Red* is zero for $t \neq 0$, because the potential was set high enough to fulfill this condition, in cyclic voltammetry the concentration ratio of *Red* and *Ox* has to be

defined at any potential point. This requires understanding of basic electrode kinetics and the associated concept of thermodynamic reversibility. Starting from the general case of an oxidation reaction, where oxidized and reduced species are in an equilibrium with forward and backward rate constants k_f and k_b .



Under the assumption of first order kinetics one can formulate the reaction rates of the forward reaction v_f and that of the backward reaction v_b as the product of rate constant and concentration of the reactand at the electrode surface.

$$v_f = k_f C_{\text{Red}}(0, t) = \frac{i_a}{nFA}, \quad v_b = k_b C_{\text{Ox}}(0, t) = \frac{i_c}{nFA} \quad (2.18)$$

The difference of the forward and backward rates yields the total rate and direction of the reaction. With nFA as a factor one establishes a connection to the *anodic* and *cathodic* current, as the currents corresponding to the forward or backward reaction. The assignment of the terms anodic and forward is arbitrary and will be used according to IUPAC recommendations.^[36]

$$v = v_f - v_b = k_f C_{\text{Red}}(0, t) - k_b C_{\text{Ox}}(0, t) \quad (2.19)$$

$$I = i_a - i_c = nFA [k_f C_{\text{Red}}(0, t) - k_b C_{\text{Ox}}(0, t)] \quad (2.20)$$

According to previous sections, increasing the electrode potential one adds free enthalpy of activation ΔG^\ddagger to the reduced species. The scaling of ΔG^\ddagger with applied potential is represented by the electron transfer coefficient α in the case of the anodic and by $(1 - \alpha)$ in the case of the cathodic current. The free enthalpy of activation ΔG^\ddagger of forward and backward reactions ΔG_a^\ddagger and ΔG_c^\ddagger can be formulated with respect to the equilibrium redox potential of Red and Ox.

$$\Delta G_a^\ddagger = \Delta G_{0,a}^\ddagger + \alpha F (E - E^0) \quad (2.21)$$

$$\Delta G_c^\ddagger = \Delta G_{0,c}^\ddagger - (1 - \alpha) F (E - E^0) \quad (2.22)$$

The rate constants can furthermore be well approximated with the Arrhenius-equation:

$$k_f = A_f \exp\left(-\frac{\Delta G_a^\ddagger}{RT}\right), \quad k_b = A_b \exp\left(-\frac{\Delta G_c^\ddagger}{RT}\right) \quad (2.23)$$

By combining equations 2.21 and 2.23 the potential dependence of the rate constants can be expressed.

$$k_f = A_f \exp\left(-\frac{\Delta G_{a,0}^\ddagger}{RT}\right) \exp\left[\frac{\alpha F}{RT} (E - E^0)\right] \quad (2.24)$$

$$k_b = A_b \exp\left(-\frac{\Delta G_{c,0}^\ddagger}{RT}\right) \exp\left[-\frac{(1 - \alpha)F}{RT} (E - E^0)\right] \quad (2.25)$$

In the special case when the surface concentrations of Red and Ox are equal, it holds that $E = E^0$ and $k_f C_{Red} = k_b C_{Ox}$. Therefore $k_f = k_b$ and can be simplified to the standard rate constant k^0 . The equations 2.24 can be simplified and a complete current potential relationship can be established (equation 2.26).

$$I = nFAk^0 \left\{ C_R(0, t) \exp\left[\frac{\alpha F}{RT} (E - E^0)\right] - C_O(0, t) \exp\left[-\frac{(1 - \alpha)F}{RT} (E - E^0)\right] \right\} \quad (2.26)$$

Rearrangement and changing from E^0 to any potential at equilibrium E_{eq} yields the Butler-Volmer equation of the kinetically limited current at any potential.

$$I = nFAk^0 \left\{ \frac{C_R(0, t)}{C_R^*} \exp\left[\frac{\alpha F}{RT} (E - E_{eq})\right] - \frac{C_O(0, t)}{C_O^*} \exp\left[-\frac{(1 - \alpha)F}{RT} (E - E_{eq})\right] \right\} \quad (2.27)$$

The validity of the Butler-Volmer can be easily proven, by considering that in a system in equilibrium no current will flow, since the forward and backward reaction rates are equal and the surface concentrations have adapted to bulk concentration at a certain potential E_{eq} . In this case one can simply write equation 2.28 and see that it collapses to the Nernst equation 2.29:

$$nFAk^0 \left\{ \frac{C_R(0, t)}{C_R^*} \exp \left[\frac{\alpha F}{RT} (E - E_{eq}) \right] = \frac{C_O(0, t)}{C_O^*} \exp \left[-\frac{(1 - \alpha)F}{RT} (E - E_{eq}) \right] \right\} \quad (2.28)$$

$$\exp \left(\frac{RT}{F} E_{eq} - E^0 \right) = \frac{C_O^*}{C_R^*} \iff E_{eq} = E^0 + \frac{RT}{F} \ln \left(\frac{C_O^*}{C_R^*} \right) \quad (2.29)$$

If on the other hand surface concentration and potential do not match, then the system is out of equilibrium and will attempt to reach this state, which in turn causes a current to flow. That means that if the potential is applied externally to the system and scanned from E_i to E_f , the concentrations at the surface will adapt as fast as possible. So the question remains, how fast can the concentration follow the dictated potential? This question in fact asks for the system's thermodynamical reversibility. A thermodynamically reversible process is defined as one that, if excited from equilibrium by external factors, even in an infinitesimally small increment immediately adjusts to find a new equilibrium state. Of course a truly reversible process can only be achieved in theory, as it would take an infinite time to go from state A to state B in infinitesimally small steps. So one can only ask for reversibility on a certain time scale and the answer to the question is found in the rate constant k_0 , which describes, how many elementary reactions are taking place per unit time. As long as equilibrium conditions apply, its magnitude does not matter, as no net reaction is happening, for example like in the beginning of the CV experiment. As soon as the potential is changed, the backward and forward rate constants are suddenly not the same any longer and now the magnitude of the net current crucially depends on the equilibrium rate constant k^0 . If k^0 is large, in other words if many molecules are commuting between reduced and oxidized state, then the ratio of Red to Ox will immediately adapt to the given potential even at low excitations. The system is in this case not kinetically hindered and called Nernstian or reversible. If the reaction rate is sluggish, then a rather large voltage is needed to achieve the proper surface concentration. This excess voltage is the overpotential and a characteristic for irreversible systems.

The diffusion equations introduced in the beginning of the section are solved with different boundary conditions employed. For a reversible system one sets in the Nernst equation as the boundary condition for the concentration at the electrode surface, thereby implicitly assuming, that the concentration immediately follows the potential at any scan rate. Kinetic limitations are completely disregarded and the problem to be solved is caused solely by diffusion. Due to the mutual dependence of voltage on time, concentration on voltage and

current on concentration the mathematics behind the solution are rather difficult and their treatment by far exceeds their benefits and the scope of this work, hence only the most important intermediate results and their implications will be discussed. The time dependence of the potential is given by:

$$E(t) = E_i + \nu t \quad (2.30)$$

The Nernst equation is to be applied as boundary condition, but has to be rearranged, to be expressed as a function of time.

$$f(t) = \frac{C_{Ox}(0, t)}{C_{Red}(0, t)} = \exp \left[\frac{nF}{RT} (E_i - \nu t - E^0) \right] \quad (2.31)$$

Several steps involving Laplace transformation, removal of dimensions and substitutions are required to arrive at a solution for the current flowing during a CV experiment.

$$i = nFAC_{Red}^* (\pi D_{Red} \sigma)^{1/2} \chi(\sigma t) \quad (2.32)$$

It turns out that the shape of the reversible CV can be calculated numerically from an integral equation and put into a dimensionless "template", $\chi(\sigma t)$, where $\sigma t = (nF/RT)\nu$, and only scales with experimental parameters like concentrations and diffusion coefficients. The relationships of key characteristics of such a reversible curve like peak potential or half-wave potential to each other are untouched by system properties. The shape of a reversible CV is shown in figure 2.16 for a reduction process. For potentials positive of E^0 , no

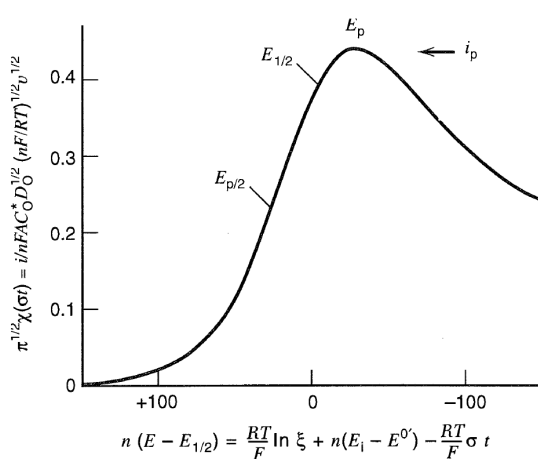


Figure 2.16.: Reversible CV "template".

reaction takes place. Upon decreasing the voltage a current is measurable and the concentration of the educt is diminishing. As the potential falls below E^0 , the concentration in front of the electrode is largely depleted so that the current runs through a maximum and declines, as diffusion through the ever thicker layer of depleted electrolyte becomes thicker. The figure shows only one scan direction, where the potential ramp is not reversed. Unfortunately, only a vanishing minority of model systems can suffice the reversible CV model and therefore the irreversible approx-

imation must be employed. In this extreme case one assumes that the electrode kinetics are

so slow that an immense overpotential must be applied to get the reaction running. At such a high potential, the reaction rate of the backward reaction is negligibly low compared to that of the forward reaction, so that only the forward reaction is considered and the boundary condition can be written as follows, using the Butler-Volmer equation.

$$\frac{i}{nFA} = D_{Ox} \left[\frac{\partial C_{Ox}(x, t)}{\partial x} \right]_{x=0} = k_f(t) C_{Ox}(0, t) \quad (2.33)$$

Solving this boundary value problem in an analogous manner one obtains a function that works in a similar way like the one described for the reversible system with the difference that the template function $\chi(b, t)$ additionally contains information about the electrode kinetics.^[34]

$$i = F A C_{Ox}^* \left[\pi D_{Ox} \nu \left(\frac{\alpha n F}{RT} \right) \right] \chi(b, t) \quad (2.34)$$

The CV curve can now have a different appearance with respect to slope, peak height or the leveling-off region and therefore provides more information than the Nernstian case. However, for the stated reasons one must be careful applying the CV theory to supercapacitor systems especially, if RTILs are used as electrolytes. First of all, RTILs are solvent free and therefore highly concentrated electrolytes that in addition are ordered in the liquid state, so that diffusion is by far not as facile as in a solvent based electrolyte. Basic diffusion laws, on which the theory is essentially built up, may not apply in that case. Moreover, in supercapacitors most of the current in the CV measurements comes from non-faradaic reactions, mainly the formation of an electrical double layer. Special processes that lead to the increase of surface charge density, be it filling of pores or RTIL rearrangement, do not fulfill the characteristics to be treated like faradaic reactions and must be considered under a different point of view. Furthermore, effects of porosity can cause ambiguous implications, as they have a strong influence on the shape of the CV signal of a redox reaction, so that they can be falsely taken for a non-faradaic surface process. The experiments have hence to be designed in such a way that all effects can be clearly distinguished from each other, as to the best of the author's knowledge no sufficient theory exists for CV on RTILs on porous electrodes.

3. Experimental Part

3.1. Syntheses

3.1.1. Synthesis of Silica Template SBA-15

SBA-15 was prepared following a standard procedure.^[37] In a representative synthesis 33.4 g poly(ethylene oxide)-poly(propylene oxide)-poly(ethylene oxide) block-copolymer (Pluronic® P 123 Sigma-Aldrich) was dissolved in 600 ml water by stirring for 12 h at 25 °C before adding 19.3 g of fuming hydrochloric acid and stirring for another 12 h, so that a homogenous solution was obtained. 71.8 g of tetraethyl orthosilicate (TEOS, 98 %, Sigma-Aldrich) was added and the reaction mixture was then stirred for 24 h at 25 °C. The resulting dispersion was heated in an autoclave at 130 °C for 24 h, filtered off and the solid was washed with approx. 500 ml of an equivoluminal water/ethanol mixture before drying over night at 60 °C. The product was calcinated under atmospheric conditions at 550 °C with a heating rate of 100 K/h for 5 h.

3.1.2. Synthesis of Ordered Mesoporous Carbon CMK-3

CMK-3 was prepared following a standard procedure.^[26] In a representative synthesis 2 g of SBA-15 was impregnated with a solution of 2.5 g sucrose and 0.28 g H₂SO₄ conc. in 10 ml water. The mixture was placed in a drying furnace at 100 °C for 6 h, and the temperature was increased to 160 °C for another 6 h. After the treatment the product turned dark brown and black upon polymerization of the sucrose. The sample was again impregnated using a solution of 1.6 g sucrose and 0.18 g H₂SO₄ conc. in 10 ml water and subsequently subjected to a second drying step similar to the first one. The product was carbonized in a tubular furnace under argon flow at 900 °C for 2 h at a heating rate of 150 K/h. The silica template was removed by refluxing the solid at 120 °C in 5 M NaOH over night. The product was filtered off, washed with approx. 2 l water and dried at 60 °C.

3.1.3. Synthesis of Salt Templated Carbons STC- n

STCs were prepared according to the method of Yan, et al.^[7] The variable n denotes the mass ratio of ZnCl_2 to sucrose. The synthesis is described exemplarily for STC-1. 5 g of sucrose and 5 g of ZnCl_2 were dissolved in 20 ml of water. 500 mg of H_2SO_4 conc. was added and the mixture was transferred into a drying furnace, where it underwent a heating procedure similar to that of CMK-3 (6 h at 100 °C, 6 h at 160 °C). Carbonization was carried out in a tubular furnace under N_2 flow at 900 °C for 2 h with a heating rate of 60 K/h. To remove inorganic salt residues, the resulting solid was stirred in 1 l of a 1 M HCl over night, filtered off, and washed with approx. 1 l of water. The washing step was repeated until the powder X-ray diffraction (XRD)-pattern showed no more reflections, typically 3 times.

3.1.4. Synthesis of Aerosil[®] Templated Carbons Aerosil[®] n - m

Aerosil[®]-carbons were synthesized analogously to CMK-3. Two types of the fumed silica were used as templates for synthesis, differing mainly in particle size; Aerosil[®] 90 and 380. Mass ratios of silica to sucrose of 1:1, 1:2 and 1:4 were chosen. The variable n denotes the type of silica used, while m stands for the sucrose/silica ratio. A typical synthesis started with the impregnation of the desired mass of the silica precursor with a solution of 2 g sucrose and 0.2 g H_2SO_4 conc. in 10 ml water. The resulting mixture was placed in a drying furnace at 100 °C for 6 h and the temperature was increased to 160 °C for another 6 h. The dark brown to black mass was transferred to a porcelain boat and carbonized at 900 °C for 2 h at a heating rate of 60 K/h. For samples with silica sucrose ratios of 2 and 4, the silica template was removed by refluxing the solid at 120 °C in 5 M NaOH over night. The product was filtered off, washed with approx. 2 l water, and dried at 60 °C. For carbons with a 1:1 template/sucrose ratio, the silica was removed by stirring in 500 ml of a 4 M $[\text{NH}_4][\text{F}_2\text{H}]$ solution for three days. The product was filtered off, washed with about 2 l of a 1:1 ethanol/water mixture and stirred in an $[\text{NH}_4][\text{F}_2\text{H}]$ solution for another three days, until thermogravimetric analysis (TGA) suggested an amount of residual template lower than 3 %. After filtration and repeated washing in 2 l of a 1:1 ethanol/water the carbon was dried at 60 °C.

3.1.5. Synthesis of FeCl_3 Templated Carbon

Iron(III)-chloride $\cdot 6 \text{H}_2\text{O}$ was used as a template for the synthesis of porous carbon materials. A solution of 3 g or 10 g $\text{FeCl}_3 \cdot 6 \text{H}_2\text{O}$ was dissolved at 60 °C in 5 ml water and 2 g sucrose

were added. The mixture was dehydrated at 100 °C and the resulting dark brown solid with some brown crystals was carbonized at 900 °C under N₂ atmosphere for 2 h at a ramp rate of 60 K/h. The product was washed thoroughly by stirring it in 1 l of 6 M HCl over night three times. After filtration the carbon was dried at 60 °C.

3.2. Materials Characterization

3.2.1. Physisorption Experiments

N₂-physisorption experiments have been carried out on a Quadrasorb apparatus (Quantachrome Instruments) at -196 °C. Before measurement, about 40-70 mg of sample have been degassed under vacuum at 150 °C for 20 h. Specific surface areas have been calculated from the multipoint BET-method ($p/p_0 = 0.05 - 0.2$). Total pore volumes have been determined at $p/p_0 = 0.95$. Pore size distributions have been calculated from the adsorption branch of the isotherm using the quenched solid density functional theory (QSDFT) method for N₂ on carbon assuming cylindrical and slit shaped pores at a temperature of -196 °C.

Pores with a diameter smaller than 1.5 nm have been evaluated from CO₂ adsorption experiments at 0 °C on a Quadrasorb apparatus. The pore size distribution was calculated using the non-local density functional theory method (NLDFIT) with CO₂ as adsorptive and carbon as the adsorbent for relative pressures below $p/p_0 = 0.03$.

3.2.2. Electrochemical Measurements

For the electrochemical characterization the carbon materials were fabricated into free standing electrodes, by mixing with a polytetrafluoroethylene solution (PTFE, 60 % in water, Sigma-Aldrich) in a mass ratio of 9:1 in ethanol and homogenization in an ultrasonic bath for several minutes. The dispersion was poured on a glass plate and mixed with razor-blades under air flow, so that upon evaporation of ethanol a mass of rubber-like consistency formed. It was dried for approx. 4 h then placed on an aluminum foil and rolled to a sheet of approx. 120 µm thickness using a commercially available roll mill. The sheet was then punched into free standing electrodes of 10 mm diameter and dried at 60 °C over night. The areal loading of the electrodes depends on the properties of the type of carbon used and was determined before each measurement for normalization of the electrochemical data. The measurements were performed with a Biologic MPG-2 potentiostat using a Swagelok cell where two platinum current collectors were sandwiching the electrodes and a separator (Dreamweaver®)

Silver 20) of 13 mm diameter. The cell was assembled in a glove box with water and oxygen contents lower than 0.1 ppm. Electrochemical measurements included cyclic voltammetry in two-electrode configuration in the potential range of 0-3.5 and 0-5 V at a scan rate of 2 mV/s, electrochemical impedance spectroscopy for determination of the cell resistance, and chronoamperometry. In CV-curves the mass specific differential capacitance C_d was calculated according to the following equation:

$$C_d = \frac{2I}{0.9m\nu} \quad (3.1)$$

Where m is the mass of one complete electrode and ν is the scanrate. 1-ethyl-3-methylimidazolium tetrafluoroborate (EMImBF₄, >98 %, Iolitec GmbH), 1-butyl-3-methylimidazolium tetrafluoroborate (BMImBF₄, >98 %, Iolitec GmbH), 1-ethyl-3-methylimidazolium bis(trifluoromethyl-sulfonyl)imide (EMImTFSI, >98 %, Iolitec GmbH) and diethylmethyl(2-methoxyethyl)ammonium bis(trifluoromethylsulfonyl)imide (DEMETFSI, >98 %, Iolitec GmbH) were employed as electrolytes. The RTILs were stored over molecular sieve (4 Å) in a glove box (water and oxygen content <0.1 ppm). For the respective measurements the RTILs were diluted with Adiponitrile (ADN, 99 %, Sigma-Aldrich). Both compounds were completely miscible in the given volume ratios.

The influence of Li-ion coordination on the phase transitions was studied by dissolving Li-salts (LiTFSI and LiPF₆, 99 %, Sigma-Aldrich) in EMImTFSI at concentrations of 0.25 M, 0.5 M, and 1 M for LiTFSI and only at 0.5 M for LiPF₆ due to the solubility of the latter. An electrochemical cell was then assembled in the same way as described previously with the solution employed as the electrolyte and subjected to the standard cyclic voltammetry procedure.

The temperature-dependence of the phase transitions under consideration were investigated performing cyclic voltammetry experiments at an elevated temperatures of 60 °C, by placing the cell in a drying furnace.

Chronoamperometry was conducted to measure the electrical response of the rearrangement of the RTIL on an applied potential. The cell under went five CV cycles in the potential range between 0 and 3.5 V to obtain a constant CV curve, followed by a discharging step at 0 V for 60 s. A potential of 4.0 V was then applied for 30 s and finally the cell was left at the previously measured open circuit potential (OCP) (0.8 V) for up to 50 s.

3.2.3. Differential Scanning Calorimetry

Differential scanning calorimetry was performed on a Netzsch DSC 204 F1 Phoenix using an aluminum pan with a pierced lid under atmospheric conditions at a heating rate of 10 K/min in the range of -90 to 150 °C. The three RTILs as well as the carbon materials under investigation were first measured purely. Then the ionic liquids were impregnated into the carbons in an amount, that corresponded to approx. one half of the total pore volume of the respective carbon, using an ultrasonic bath for several hours. Calculations of phase transition enthalpies were later normalized to the molar amount of ionic liquid in the sample.

3.2.4. Thermal Analysis

Thermogravimetric analysis (TGA) was conducted on a Netzsch TG 209 F1 Iris in a temperature range between room temperature and 1000 °C at a heating rate of 5 K/min. The sample was placed in a platinum crucible and subjected to a constant synthetic air flow. Elemental analysis (EA) was performed on a vario MICRO CHNS analyser by elementar.

3.2.5. X-ray Diffraction

X-ray diffraction measurements were carried out on a Bruker D8 in Bragg-Brentano geometry in a 2θ range of 10° to 70° with a resolution of 0.03°. $\text{Cu}_{K\alpha}$ radiation ($\lambda = 1.54 \text{ \AA}$) and a NaI scintillation detector were used. The sample was placed horizontally on a silicon single-crystal sample holder.

3.2.6. Transmission Electron Microscopy

The materials were further characterized with transmission electron microscopy (TEM) on an EM 912 microscope by Omega/Carl-Zeiss Oberkochen. The samples were prepared by dispersion in ethanol in an ultrasonic bath for 10 min, followed by dropwise application of the dispersion on a carbon-coated copper TEM grid and drying at room temperature.

4. Results and discussion

4.1. Characterization of Carbon Materials

4.1.1. Salt-Templated Carbon and CMK-3

A series of salt-templated carbons with expectedly high amount of micropores (< 2 nm) throughout the series and an increasing mesopore content¹ (≈ 4 nm) from STC-1 to STC-8 was synthesized by polycondensation of a sucrose/ ZnCl_2 solution and subsequent pyrolysis under inert atmosphere.^[7] Residual ZnCl_2 was washed out in HCl , so that from thermogravimetric analysis an ash content of less than 3 % was detected (see figure A.2).

These carbon materials were selected for the further study, as the formation of peaks in cyclic voltammetry at potentials higher than 4 V was initially observed there. Those peaks are believed to originate from specific interactions at the border between the surface of the mesopores of the carbons and the ionic liquid. The possibility to adjust the mesopore volume by varying the ZnCl_2 /sucrose ratio in those type of carbons is therefore very useful to study the relationship between mesopore volume and shape as well as position of the peak in the CV.

Additionally, CMK-3 carbon with very uniform and ordered pores of approximately 4 nm diameter and a negligible amount of micropores was prepared to serve as a reference sample to investigate the influence of micropores on the CV response. Preparation of this material followed a standard procedure, including impregnation of the silica-precursor SBA-15 with a sucrose solution, polycondensation of the mixture and carbonization under inert gas.^[26] Refluxing the product in 5 M NaOH resulted in a practically complete dissolution of the silica as indicated by the ash content of less than 2 % as measured with TGA.

The X-ray diffraction patterns of all mentioned materials showed only two broad peaks at $2\theta = 24^\circ$ and 44° demonstrating the amorphous structure of the carbon and the absence of inorganic residues from the porogen (see figure A.1).

¹The classification of pores by their respective size will proceed after IUPAC recommendations, with macropores being larger than 50 nm in width, micropores being smaller than 2 nm, and mesopores having a size in between.^[38]

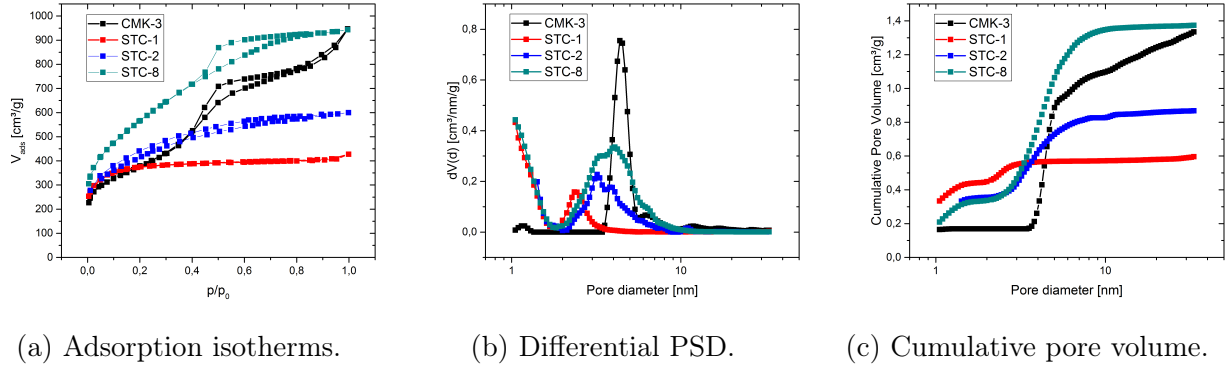


Figure 4.1.: N_2 physisorption measurements at 77 K and corresponding pore size distributions of CMK-3, STC-1, STC-2 and STC-8.

Gas adsorption was carried out to determine specific surface area, pore volume and pore size distribution (PSD). N_2 at 77 K and CO_2 at 273 K were used as adsorptives. CO_2 -measurements are specifically useful for the investigation of micropores.

N_2 adsorption isotherms, the differential pore size distribution and the cumulative pore volumes of STC-1, STC-2 STC-8 and CMK-3 are depicted in Figure 4.1. Table 4.1 gives an overview over the most important pore properties of the carbons.

STC-1 exhibits a type Ia isotherm,^[38] being concave to the p/p_0 -axis with a rather sharp inflection point at low relative pressures. This type of isotherms is typical for purely microporous materials with pore widths lower than 1 nm. Fitting the isotherm to a QSDFT kernel with pores of cylindrical and slit shape reveals that a small amount of mesopores of about 2.5 nm in diameter contributes to the total pore volume (Figures 4.1b and 4.1c). The N_2 adsorption isotherm of STC-2 is levelling off smoother than that of STC-1 and can therefore be classified as type I(b), indicating a broader pore size distribution of micropores and a significant amount of small mesopores. While the BET surface area is only slightly higher than

Table 4.1.: BET specific surface area (SSA), total pore volume (V_{tot}), and micro- and mesopore volumes from DFT (V_{micro} and V_{meso}) of the STCs and CMK-3.

	SSA [m ² g ⁻¹]	V_{tot} [cm ³ g ⁻¹]	DFT	
			V_{micro} [cm ³ g ⁻¹]	V_{meso} [cm ³ g ⁻¹]
CMK-3	1331	1.35	0.17	1.17
STC-1	1380	0.63	0.45	0.15
STC-2	1472	0.92	0.36	0.51
STC-8	2051	1.45	0.52	0.81

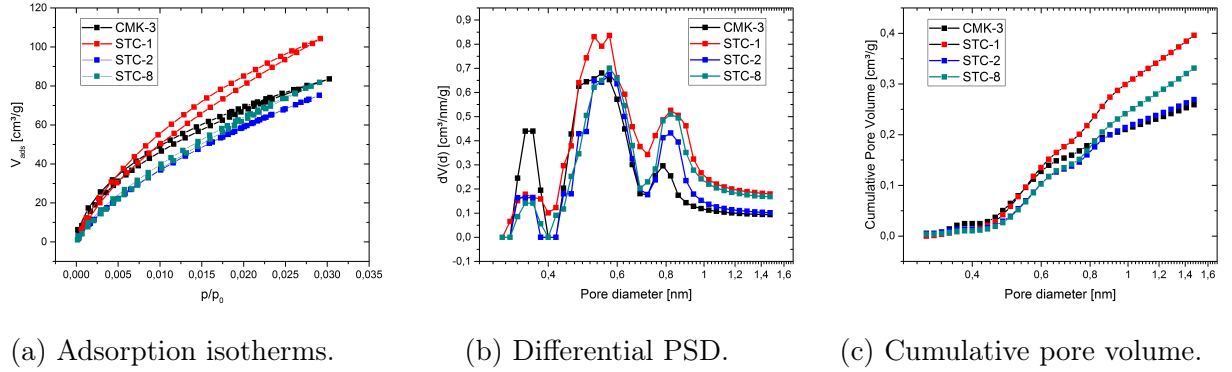


Figure 4.2.: CO₂ physisorption measurements at 273 K and corresponding pore size distributions of CMK-3, STC-1, STC-2 and STC-8.

in the case of STC-1 (1472 vs. 1380 m²g⁻¹), the total pore volume is increased by a factor of 1.5. DFT calculations support those findings. Both samples have approximately the same volume of micropores but both, the volume and size of the mesopores of STC-2 are increased. For the carbon material with the highest amount of porogen, STC-8, an isotherm of type IVa with a H4 hysteresis loop in the relative pressure range of 0.4 to 0.9 is found, which is characteristic for micro-mesoporous carbons. Compared to the previous two samples of the series, the specific surface area as well as the total pore volume are significantly increased to 2051 m²g⁻¹ and 1.45 m³g⁻¹ respectively. From DFT it is evident, that the micropore volume again remains almost unaffected, whereas the mesopore volume and size are higher as compared to STC-1 and STC-2. Nitrogen adsorption isotherms of CMK-3 are of type IVa with a H2(a) hysteresis in the relative pressure region of 0.4 to 0.8. The total adsorbed volume at low pressures is the lowest throughout the series. The shape of the hysteresis loop additionally points at a pore shape, where the diameter of the pore entrance is lower than that of the pore interior and thus pore blocking effects must be considered. The material exhibits a large total pore volume of 1.35 m³g⁻¹ and a comparably low specific surface area of 1331 m²g⁻¹, suggesting a mostly mesoporous pore structure. DFT calculations reveal a very narrow pore size distribution around 4 nm and an almost negligible amount of micropores. CO₂ adsorption at 273 K was employed to investigate the micropore structure of the carbons in more detail. With its low kinetic dimension of 0.33 nm and a high saturation vapor pressure the use of CO₂ as an adsorptive offers the opportunity to study extremely narrow micropores between approximately 0.4 and 1 nm at moderately low pressure and within short equilibration times.^[38] Analysis of the isotherms with NLDFT reveals that micropores of three diameters, 0.35 nm, 0.55 nm and 0.8 nm, are present in all of the prepared carbons

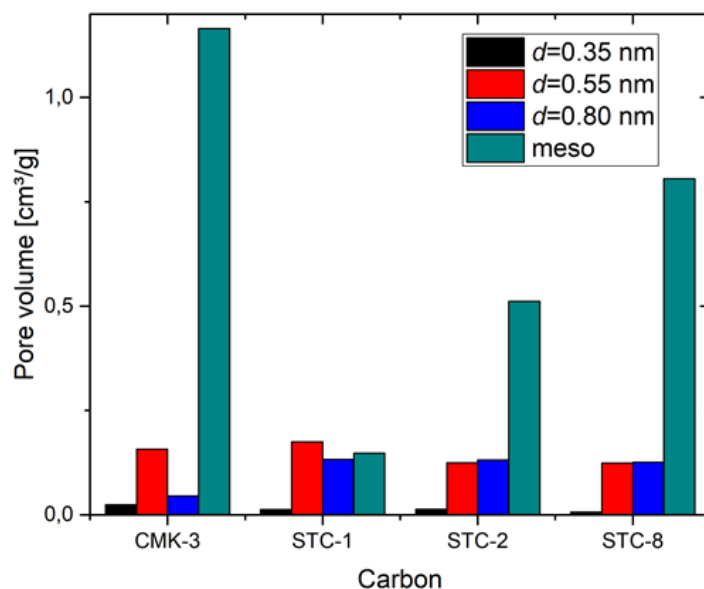


Figure 4.3.: Volume of the micropores and mesopores in STCs and CMK-3 for different diameters.

(see figure 4.2). The carbons obtained from the salt-templating approach seem to have a similar micropore structure, consisting of an almost negligible volume of 0.35 nm sized pores (around $0.01 \text{ cm}^3\text{g}^{-1}$) and in equal amounts pores of 0.55 and 0.80 nm diameter, respectively ($0.13 - 0.18 \text{ cm}^3\text{g}^{-1}$, see figure 4.3). CMK-3 pore structure is different from that of the STCs in terms of a lower total micropore volume and especially a drastically lower volume of pores with a diameter of 0.8 nm, which are most interesting for this work as they are large enough, to fit most of the ions of the RTILs. This makes the CMK-3 carbon a useful reference sample, as interactions of electrolyte ions with the micropores can be ruled out; yet this issue should be stressed later in this work.

4.1.2. Aerosil[®]-Silica Templated Carbon

For further experiments a number of hard-templated carbons have been prepared in a similar way to CMK-3. Instead of using SBA-15 as a silica-template, the commercially available fumed silicas Aerosil[®]90 and Aerosil[®]380 have been employed in different ratios to sucrose. Aerosil[®] is an amorphous silica powder that is produced via flame spray pyrolysis of silicon tetrachloride together with elemental hydrogen and oxygen to produce silicon dioxide and hydrogen chloride. If the spherical primary particles that are formed

within seconds are kept in the flame for a prolonged time, they firstly grow larger and then begin to aggregate and agglomerate in a colder region of the flame. The number in the name denotes the specific surface area of the particular sample and is inversely proportional to the average primary particle size.^[39] The mean particle size can thus be expected to be around 20 nm for Aerosil[®]90 and 8 nm for Aerosil[®]380, so by choosing the type of Aerosil[®] during carbon synthesis one can adjust the pore size of the product. Altering the template/sucrose ratio provides control over the carbon pore volume pore volume. Following this reasoning six carbon samples have been prepared, using Aerosil[®]90 and Aerosil[®]380 in sucrose/silica ratios of 1:1, 2:1 and 4:1. Accordingly the number in the name of the corresponding carbon represents the sucrose/silica ratio (e.g. Aerosil[®]90-2 for a ratio of 2:1). The higher the template loading, the larger the pore volume is expected to be. The purpose of these materials is to prove in later cyclic voltammetry experiments, if the current signal at potentials higher than 4 V is related rather to the pore size or the pore volume and thereby to allow statements about the signal's physicochemical origins.

Nitrogen adsorption isotherms at 77 K have been measured and the data are presented in table 4.2. The shape of all isotherms can be classified as type IV(a) with an H4 type hysteresis (figure 4.4a). The hysteresis is found at higher relative pressures for Aerosil[®]90, Aerosil[®]90-2 and Aerosil[®]90-4 ($0.7 < p/p_0 < 1.0$), than for Aerosil[®]380, Aerosil[®]380-2 and Aerosil[®]380-4 ($0.7 < p/p_0 < 0.9$), indicating larger pores for the Aerosil[®]90 carbons than for the Aerosil[®]380 templated ones. Additionally a drastic increase of adsorbed nitrogen at relative pressures close to the condensation point is found for carbons with a sucrose/silica ratio of one and to some extent also for the ratio of two, which is due to the presence of some external surface. Carbons with a sucrose/silica ratio of four have the lowest amount of micropores and very distinct hystereses at the same relative pressures as their pendants with higher template fraction. At relative pressures approaching one the isotherms level off having adsorbed almost the same amount of nitrogen, indicating a comparable total pore volume and no considerable external surface area.

While these findings justify the approach of adjusting pore size and volume by varying type and amount of template, they also unveil two problems; firstly, that too much template results in percolation of the pore structure leading to mainly external surface area and secondly, that aggregates and agglomerates of the primary Aerosil[®] particles lead to a pore geometry that is not fully homogenous and spherical, especially for the larger Aerosil[®]90 particles. As a result, fitting of the adsorption data was done with a DFT-kernel of slit/cylindrical shaped pores, rather than a spherical one. The mesopores of the materials were found to be narrowly distributed at around 16 nm for Aerosil[®]90 and around 8 nm for Aerosil[®]380. The

RESULTS AND DISCUSSION

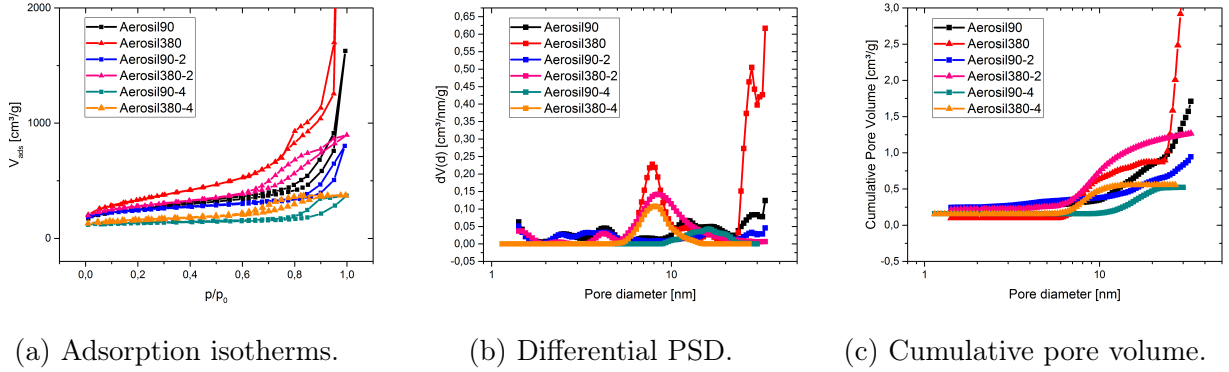


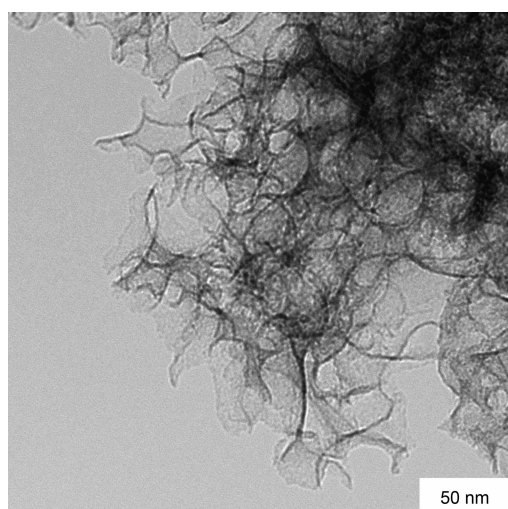
Figure 4.4.: N_2 physisorption measurements at 77 K and corresponding pore size distributions of Aerosil[®] templated carbons.

pore volumes followed the expected trend and increased with increasing template loading, although for the case of Aerosil[®]380 the pore volume seems to be lower at the first glance in the cumulative volume plot.

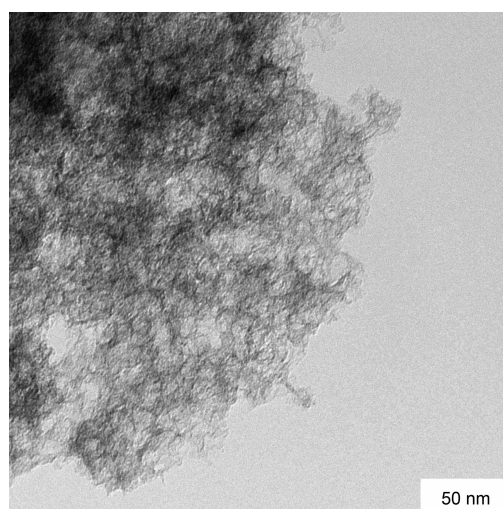
Also the amount of external surface is reduced with decreasing template fraction as can be seen from the constant slope in the pore volume vs. diameter plot in figure 4.4 at high diameters. TEM images support the gas adsorption data well. For the Aerosil[®]-carbons with equal amount of sucrose and silica one can observe a sponge-like structure with spherical "holes" in it that are strongly interconnected with each other. The size of these holes is significantly larger for Aerosil[®]90 than for Aerosil[®]380 templated carbon, which is in line with the aforementioned data. With decreasing template amount Aerosil[®]380 templated carbon densifies, but keeps its sponge-like pore structure. Finally, Aerosil[®]380-4 appears as a dense grain, where no pores can be recognized in the TEM image. Aerosil[®]90-2 particles can also be described as rather dense and pores cannot be seen neither for Aerosil[®]90-2 nor

Table 4.2.: BET specific surface area (SSA), total pore volume (V_{tot}), and micro- and mesopore volumes from DFT (V_{micro} and V_{meso}) of the Aerosil[®] templated carbon materials.

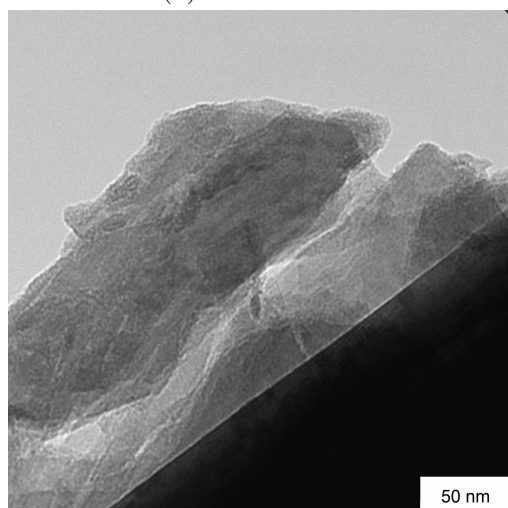
	SSA [m ² g ⁻¹]	V_{tot} [cm ³ g ⁻¹]	DFT	
			V_{micro} [cm ³ g ⁻¹]	V_{meso} [cm ³ g ⁻¹]
Aerosil90	891	1.18	0.20	0.98
Aerosil90-2	881	0.79	0.26	0.64
Aerosil90-4	490	0.44	0.16	0.36
Aerosil380	1236	1.61	0.10	0.90
Aerosil380-2	987	1.28	0.23	0.64
Aerosil380-4	567	0.58	0.15	0.40



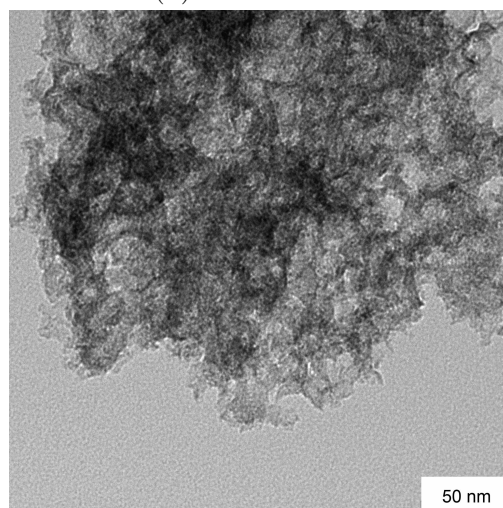
(a) Aerosil®90.



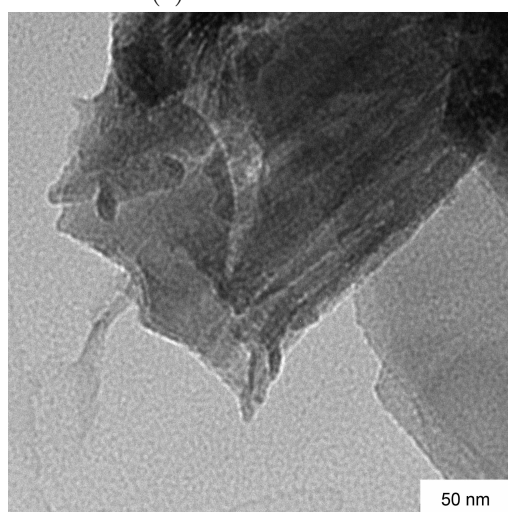
(b) Aerosil®380.



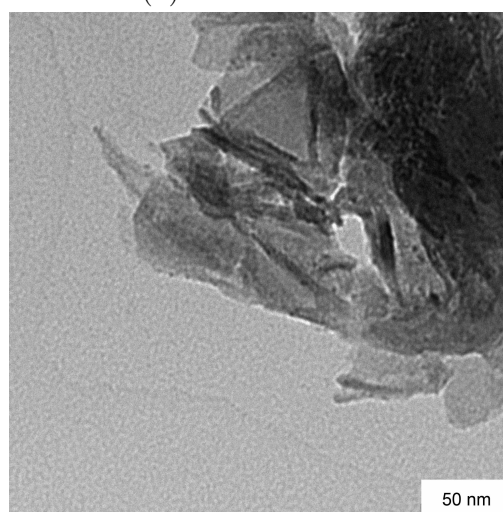
(c) Aerosil®90-2.



(d) Aerosil®380-2.



(e) Aerosil®90-4.



(f) Aerosil®380-4.

Figure 4.5.: TEM-images of Aerosil®-templated carbons.

RESULTS AND DISCUSSION

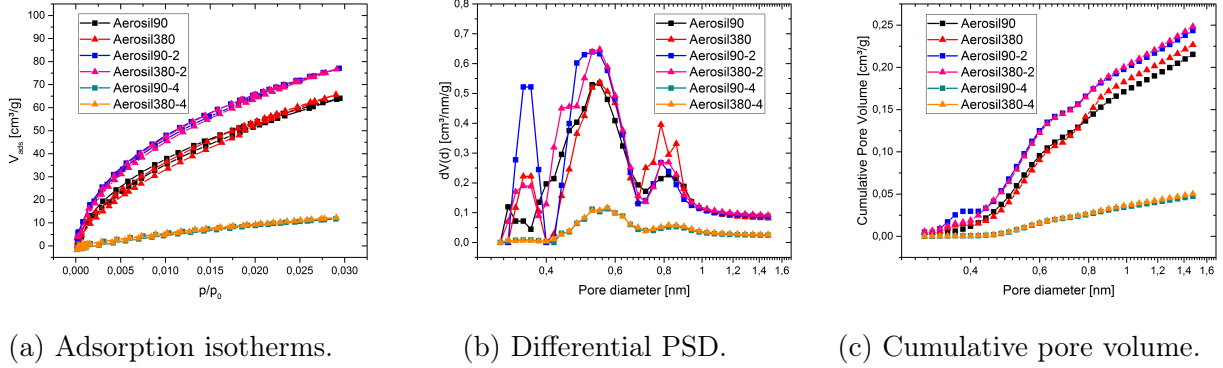


Figure 4.6.: CO₂ physisorption measurements at 273 K and corresponding pore size distributions of Aerosil[®] templated carbons.

for Aerosil[®]90-4. CO₂ adsorption at 273 K was performed to investigate the microporosity of Aerosil[®]-carbons (figure 4.6). The isotherms of the carbons with the same sucrose/silica ratio are practically identical and the amount of adsorbed gas is the highest for a sucrose/silica ratio of two, slightly lower for a ratio of one and in the samples with the least amount of template the adsorbed volume was by far the lowest. From NLDT calculations it turns out that the micropore structure can be constructed of pores of the same three diameters as it is the case for the first carbon series; 0.35, 0.55 and 0.80 nm. The major part of the micropore volume is comprised by pores of diameters up to 0.55 nm (around 0.12 cm³g⁻¹) and only a minor amount comes from 0.8 nm pores (around 0.05 cm³g⁻¹) for Aerosils[®] 1 and 2. In Aerosils[®] 4 the micropore volume is negligibly small. In table 4.3 an overview over the micropore distribution is given.

Table 4.3.: Volume of the micropores of Aerosil[®] carbon for different diameters.

	Pore volume of micropore sizes [m ³ g ⁻¹]						
	0.35 nm	0.55 nm	0.80 nm		0.35 nm	0.55 nm	0.80 nm
Aerosil90	0.01	0.12	0.05	Aerosil380	0.01	0.10	0.07
Aerosil90-2	0.03	0.12	0.05	Aerosil380-2	0.02	0.13	0.05
Aerosil90-4	0.00	0.02	0.02	Aerosil380-4	0.00	0.02	0.02

4.1.3. Iron(III)-Chloride Templated Carbon

In an attempt to use an alternative porogen to ZnCl_2 , $\text{FeCl}_3 \cdot 6 \text{H}_2\text{O}$ was tested for this purpose. The idea behind it was that due to its low melting point of 60°C it could be possible to dissolve the sucrose *directly* in the $\text{FeCl}_3 \cdot 6 \text{H}_2\text{O}$ melt. As the solubility of sucrose in the salt melt is not high enough, water had to be added. During the dehydration of the sucrose the temperature did not exceed 100°C to avoid the formation of oxides and hydroxides of iron. The further synthesis followed the established method and yielded a material consisting solely of carbon as indicated by XRD and TGA measurements (figures A.2 and A.1). Nitrogen adsorption at 77 K was performed on iron(III)-chloride templated carbons (figure 4.7). Both materials prepared with this method exhibit type Ia isotherms of nearly identical shapes, but at different adsorbate volumes, where that of FeTC-10 contains a small hysteresis, indicating a mainly microporous structure with slightly different micropore volumes. This finding is supported by DFT pore size analysis. Most of the pore volume is composed of pores smaller than 1 nm and only a minor fraction comes from pores sized 2.2 nm. Surface areas as well as total pore volume are also roughly the same. CO_2 adsorption at 273 K shows controversial results for the two investigated carbon materials (figure A.4). While both samples appear to have pores sized mostly 0.6 and 1.0 nm as well as a high amount of undefined pore sizes, FeTC-3 has a significantly higher pore volume than FeTC-10. This is unexpected, as a higher amount of FeCl_3 was supposed to increase the pore volume. TEM-images (figure 4.8) were measured, to gain insights about the carbons' pore structure. FeTC-3 appears there in more densely packed grains than FeTC-10 and no significant surface structure is observed. For FeTC-10, on the other hand, the image shows that the surface is covered by small holes that give the material a coarse appearance. The presence of a certain

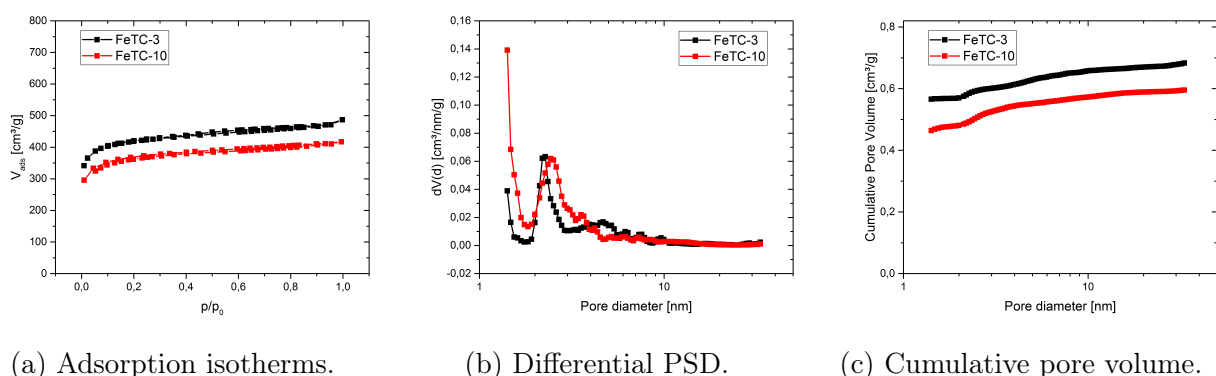


Figure 4.7.: N_2 physisorption measurements at 77 K and corresponding pore size distributions of iron(III)-chloride templated carbons.

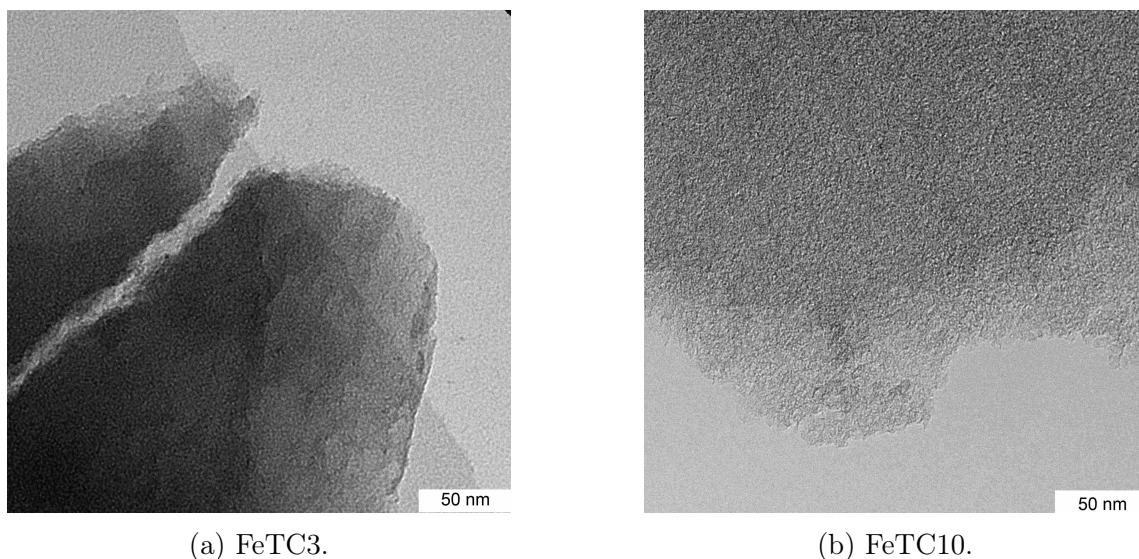


Figure 4.8.: TEM-images of iron(III)-chloride templated carbons.

fraction of mesopores is further implied by the lower weight of FeTC-10 electrodes compared to FeTC-3 electrodes (3.5 vs. 7.0 mg per electrode, equal thickness), as the presence of additional mesopores would decrease the density of the sample. These findings are in line with the results from nitrogen adsorption experiments. All in all this approach apparently offers the opportunity to influence the microporosity of the carbon material, which could possibly be useful in future syntheses. Possibly other ratios of starting materials, especially a lower amount of porogen, pH-variation or change of polymerization/carbonization parameters could be applied to influence the result of the preparation. A drawback of the method is of course that the porogen could not be recovered afterwards, because iron oxides and hydroxides have been formed to a large extent.

Table 4.4.: BET specific surface area (SSA), total pore volume (V_{tot}), and micro- and mesopore volumes from DFT (V_{micro} and V_{meso}) of the iron(III)-chloride templated carbon materials.

	SSA [m^2g^{-1}]	V_{tot} [cm^3g^{-1}]	DFT	
			V_{micro} [cm^3g^{-1}]	V_{meso} [cm^3g^{-1}]
FeTC-3	1535	0.73	0.57	0.11
FeTC-10	1361	0.63	0.48	0.11

4.2. Cyclic Voltammetry

4.2.1. Interaction of Ionic Liquids with Micropores

CV measurements have been conducted on carbon materials with different pore size distributions and with imidazolium based RTILs, namely EMImBF₄, BMImBF₄ and EMImTFSI. These liquids have been selected due to their relatively high conductivity, low viscosity and, most importantly, their wide ECW of 4.7 V for EMImBF₄ and BMImBF₄ and >5 V for EMImTFSI as stated by the manufacturer as well as Zhang et al.^[40,41] The aim of this measurement series is to investigate the origin of peaks in the cyclic voltammograms that should have a purely rectangular shape for an ideal capacitor according to equation 4.1.

$$Q = CU \rightarrow I = C \cdot \frac{E}{t} \quad (4.1)$$

The discussion of current signals will be mainly divided into such, taking place at comparably low potentials (up to 2 V) and those happening at higher cell voltages above 4 V, because different processes are assumed to be responsible for them. Note that in the cyclic voltammograms instead of the current density the specific differential capacitance is plotted. This is due to the fact that every current flowing through a capacitor is expected to be a consequence only of charging and discharging of the electrochemical double layer and not of chemical reactions. Therefore the specific differential capacitance offers a better comparability of the capacitors performance as it is also normalized to the scan rate. However, processes exceeding double-layer charging including chemical reactions will play an important role in this work, so sometimes the less usual quantity "current density" will be used.

The occurrence of peaks in the CV indicates processes at the surface of the electrode that go beyond the formation of a conventional electrochemical double layer. As this work is dealing with highly porous materials with pore sizes in the order of magnitude starting from one single ion to multiple layers of ions, current signals in the CV, especially in the low-potential region, may stem from filling or emptying of pores, depending of the charge of the ion and the pore wall, respectively. As this process introduces a change in surface charge, an electric current is expected to flow.^[19]

A necessary requirement for this phenomenon to take place is the presence of pores of a suitable size, to accommodate the respective ions. If this condition is met, not only a current peak in the CV-measurement is expected to be observed, but also an enhancement of differential capacitance, as is predicted in theoretical and experimental work.^[3,6] It has been shown by Futamura et al.^[5] using X-ray scattering together with Monte-Carlo simulations

on EMImTFSI using so called carbide derived carbons with precisely adjustable pore size that the coulombic ordering present in bulk RTILs is less pronounced under confinement of the ions in pores with a diameter slightly larger than the size of an ion. Instead of the ions being surrounded shell-wise by their respective counterions, an excess amount of either positively or negatively charged ions was found inside of the nanopore environment. The surplus charge is expected to be screened via the formation of counter charges in the pore walls of the carbon.^[35]

A first indication of some of those effects can be found in the cyclic voltammograms of car-

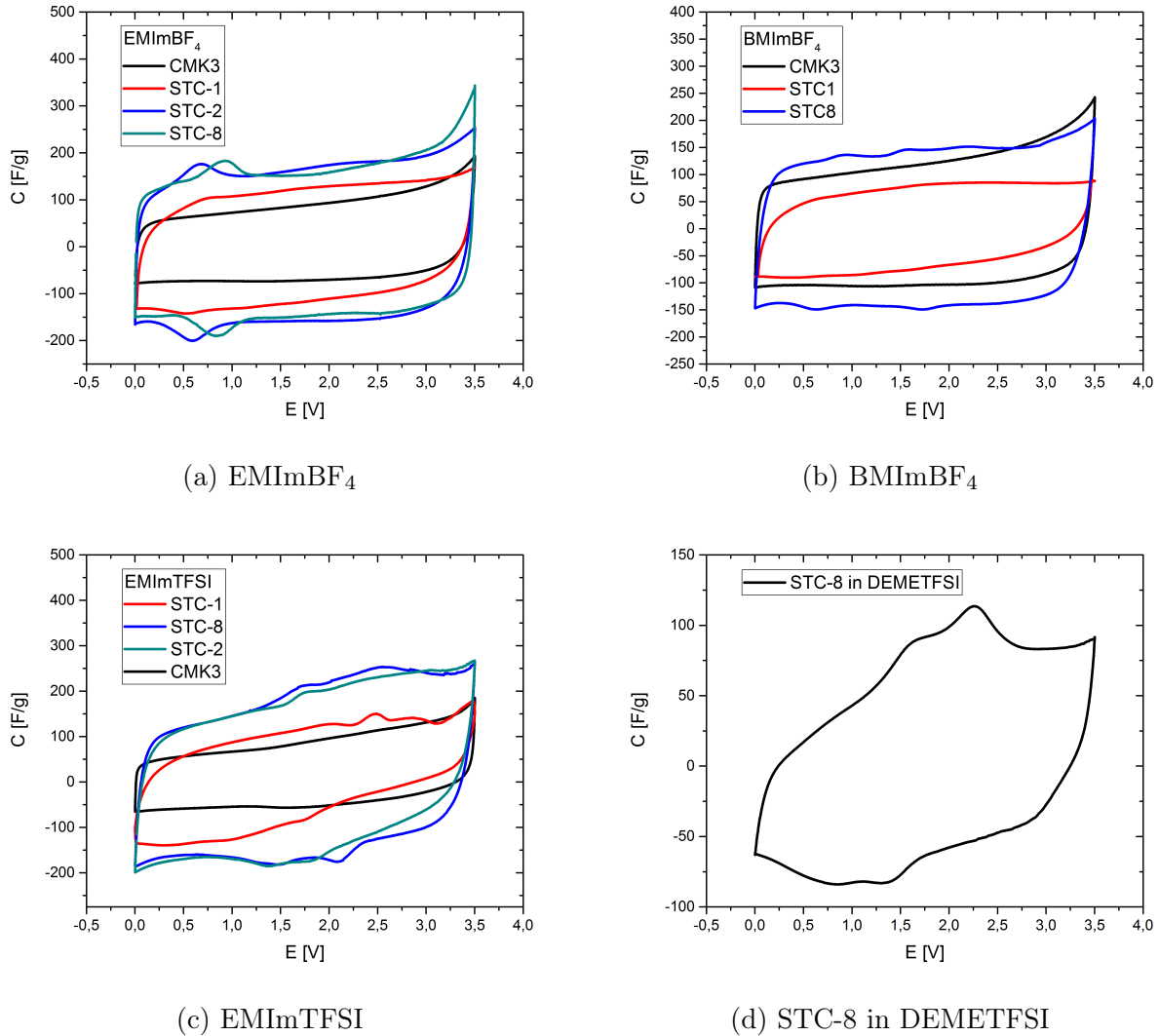


Figure 4.9.: Cyclic voltammograms of CMK-3, STC-1 and STC-8 in EMImBF₄, BMImBF₄ and EMImTFSI at 2 mV s⁻¹ and of STC-8 in DEMETFSI.

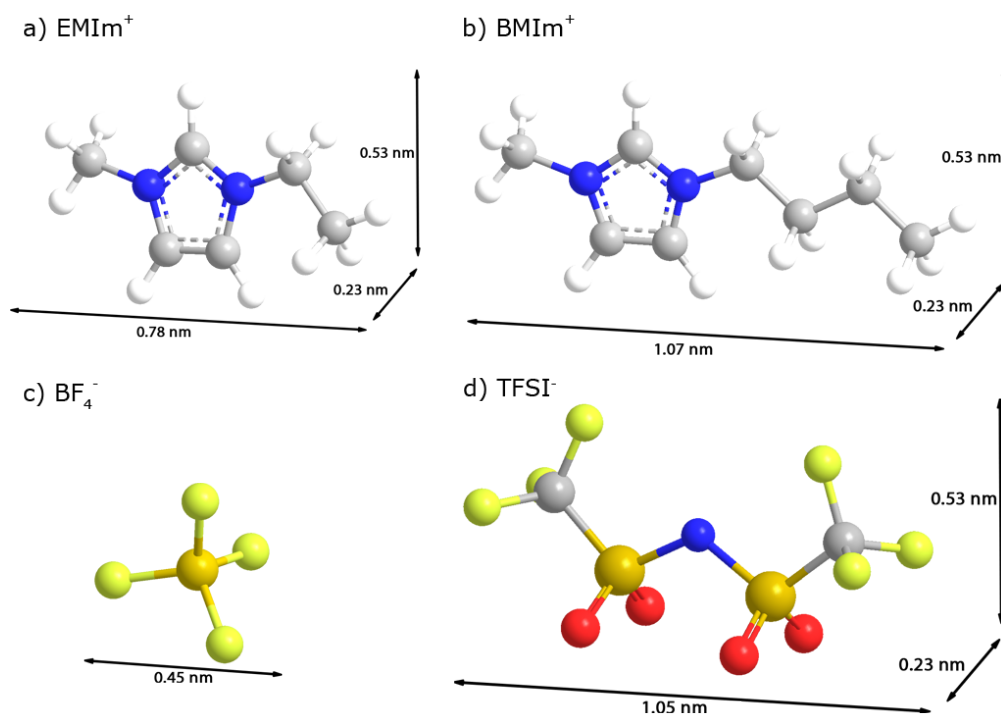


Figure 4.10.: Size comparison of RTIL ions under study as estimated from Chem3D.

bons of the STC-series and CMK-3 in EMImBF₄ in the potential range of 0 - 3.5 V (figure 4.9a). The almost purely mesoporous carbon CMK-3 ($d \approx 4$ nm) shows no peaks and the lowest differential capacitance of the three materials under investigation. STCs exhibit a higher differential capacitance, especially STC-8, of which the micropores are interconnected by a large amount of mesopores and therefore more micropores are easier accessible to the ions. Also it is notable that STC-8 and STC-2 as well as STC-1 to some extent show peaks in the forward and reverse scans of the CV at around at 0.9 V and 0.6 V respectively that can be attributed to filling and emptying of pores with ions. As can be seen from figure 4.10, the dimensions of both, the EMIm⁺ and the BF₄⁻ ions are small enough to enter the micropores of the STCs centered around 0.8 nm.

The peak does not exhibit the typical shape of a faradaic redox process but is more of a symmetrical appearance that implies an event that takes place exclusively at the electrode surface. Also it is known from previous work that this signal will appear even after numerous cycles with almost unchanged current and voltage signature, rather untypical for a redox process.^[7]

Increasing the cation size by changing the electrolyte to BMImBF₄ leads to a slight decrease in differential capacitance for STC-8, whereas the capacitance of STC-1 diminishes

to approximately half of the current present in EMImBF₄ as electrolyte. Also the peak at ≈ 0.9 V is now only vaguely perceivable for the former sample and completely absent for the latter one. The behaviour of CMK-3 remains unchanged apart from the minor increase in differential capacitance for BMImBF₄.

As we return to the smaller EMIm⁺ cation but change the anion to the somewhat larger molecule TFSI⁻, some remarkable differences can be observed compared to both EMImBF₄ and BMImBF₄. While CMK-3 still does not show any peaks in the CV, the cyclic voltammograms of STC-1 and STC-8 on the contrary are characterized by two peaks at around 2.0 and 2.5 V in the forward and backward scan instead of the small peak at 0.9 V that was present in the measurement of the carbons in EMImBF₄. Again this effect is more pronounced for STC-8 due to its pore structure. As the CV changed its shape only upon change of the anion of the electrolyte, it can be concluded that the peaks that dominate the CVs in the relatively low voltage range arise mainly from reversible processes that involve the respective anion of the RTIL employed as electrolyte. Experiments with STC-8 in DEMETFSI corroborate this assumption, since it features analogous signals to those of the measurements in EMImTFSI. Again the reversibility of the peaks, in particular the fact that they remain unaltered after multiple CV-cycles, and the correlation to the pore structure of the carbons suggest that no faradaic reaction but rather a pore filling/emptying process is responsible for their occurrence. Furthermore it seems like the aforementioned effect can be ascribed to rearrangements of the anion, which is in line with the findings of Wen et al.^[20] who studied pyrrolidinium based RTILs at a gold surface and suggest that the imidazolium-ions cover the surface in a uniform layer with the ring parallel to the surface, irrespectively of the applied potential.

All in all the micropore-filling mechanism and its current signature is visualized in figure 4.11. Before application of a potential, the micropores are apparently not filled with ionic liquid and the ions in the bulk are arranged in a close-range order with each ion surrounded by a shell of counter ions as proposed by the model of coulombic ordering. Entering the micropores would require decoordination of counterions from each other, which means a disruption of coulombic ordering that is energetically unfavorable (figure 4.11, 1). With increasing cell voltage, an electrochemical double layer is formed continuously, where the RTIL ions do not yet enter the micropores but only gather at external surface or, if present, in larger mesopores (figure 4.11, 2). When a certain potential is reached that is high enough to overcome the attractive forces between the counterions, the ions are compelled into the micropores of the carbon (figure 4.11, 3). The charge of the ions is now compensated by the pore walls (indicated in blue in figure 4.11). The sudden increase in surface charge over time and the energy coming from decoordination of the ions is recorded as a current peak in the CV.

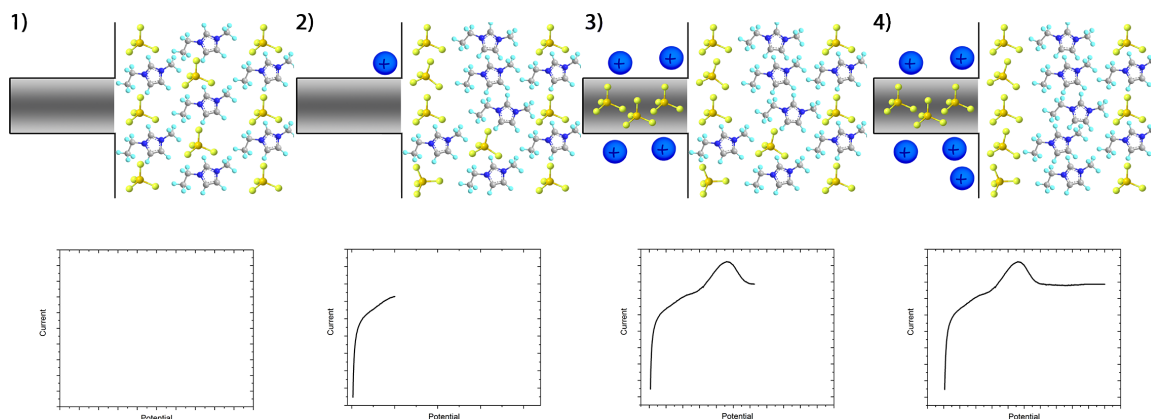


Figure 4.11.: Schematic of micropore-filling as an explanation of low-potential peaks in cyclic voltammetry on EMImBF₄ as a model electrolyte.

Keeping in mind that the position of a signal on the potential axis essentially correlates to the activation energy of the process causing it and assuming that at the moment, when the ion enters the micropore the attractive electrostatic force of the pore wall is equal to those of the coordination of the ion one should be able to estimate the coordination energy. For that, measurements in a three-electrode setup, where the reference potential is fixed, are necessary. After the pore is filled with electrolyte, the cell continues charging by further building up the electrochemical double layer. This model does not only explain peaks in cyclic voltammetry curves, but also has the process of filling and emptying a pore with RTIL ions upon application of an electric potential been studied and proved by Futamura et al.^[5] using small-angle X-ray scattering.

4.2.2. Structural Transitions at High Potentials

Beyond the signals at low cell voltages of the CV, there is one feature that almost all of the measurements performed yet have in common that is the drastic increase in current at potentials higher than 3 V. Figure 4.12 shows the first five CV cycles in the potential range between 0 and 5 V of CMK-3 carbon. To ensure reproducibility the measurement to 5 V was preceded by 5 cycles between 0 and 3.5 V to obtain a constant CV-characteristic. It can be observed that at a potential above 3.5 V a current sets in and runs through a peak at approximately 4.6 V.

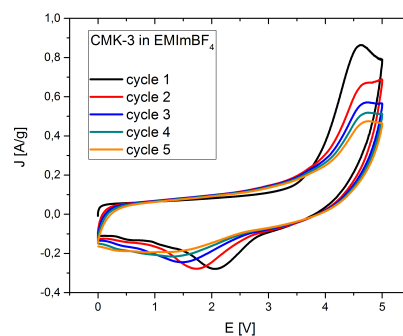


Figure 4.12.: Cyclic voltammetry of CMK-3 in EMImBF₄ at 2 mV s⁻¹.

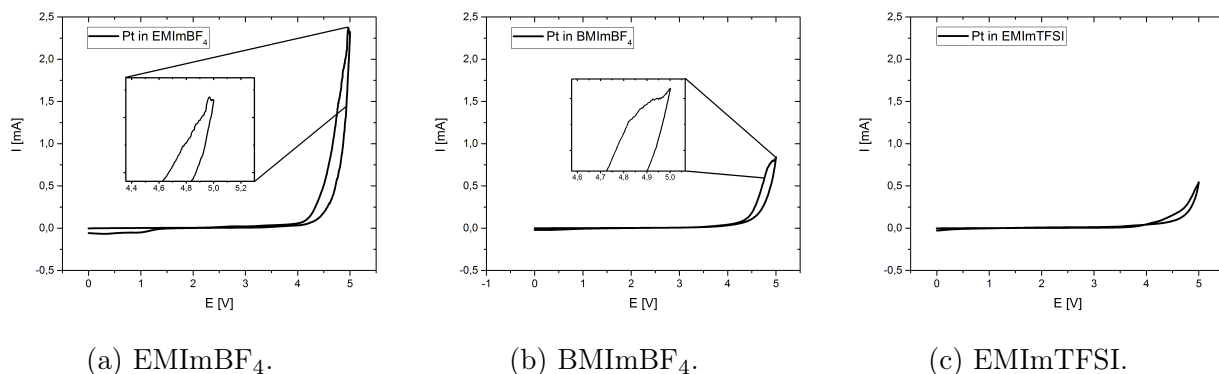


Figure 4.13.: Cyclic voltammograms of platinum in the investigated ionic liquids. Insets show noise originating from decomposition of the electrolyte (0-5.0 V, $\nu = 2 \text{ mV s}^{-1}$).

In the reverse scan a cathodic signal occurs, starting at 3.0 V and traversing a maximum at 2.1 V. During the following cycles both, forward and backward peaks become smaller, while the onset of the forward peak remains almost constant and that of the reverse peak is shifted to lower potentials. This is observed analogously in all three investigated RTILs. The first explanation that comes to ones mind is of course the irreversible decomposition of the ionic liquid. Although the degradation of the electrolyte would be expected to yield a constantly increasing current in the CV, without the formation of a peak as the concentration of electrochemically active species would be extremely high in that case, one could imagine that due to the high amount of small pores the current could reach a maximum at some point, when there is no more electrolyte left inside those pores.

To verify this suspicion, Swagelok-type electrochemical cells were constructed in a two-electrode setup with two platinum discs as the electrodes. Instead of only one layer of separator, three layers were used to soak up the electrolyte that is usually absorbed by the carbon felt. The cells were subjected to the same testing procedure as the ones containing carbon. After measuring the impedance at open circuit potential they were cycled to 3.5 V five times and then to 5 V another five times. The scan rate was again 2 mV s^{-1} and the experiment was carried out for all three involved RTILs. From those measurements it is evident that the electrolysis of the RTIL begins well above 4.0 V for all three samples and causes a relatively high current, especially if the surface area of the platinum discs is compared to the one of the carbon materials that is by orders of magnitude higher (figure 4.13). The leveling off at the end of the curves is not to be confused with the peaks described above, as it is caused by the reaction products of the decomposition reaction, which are unable to leave the electrode surface fast enough to allow diffusion of new electrolyte. Insets in figure 4.13

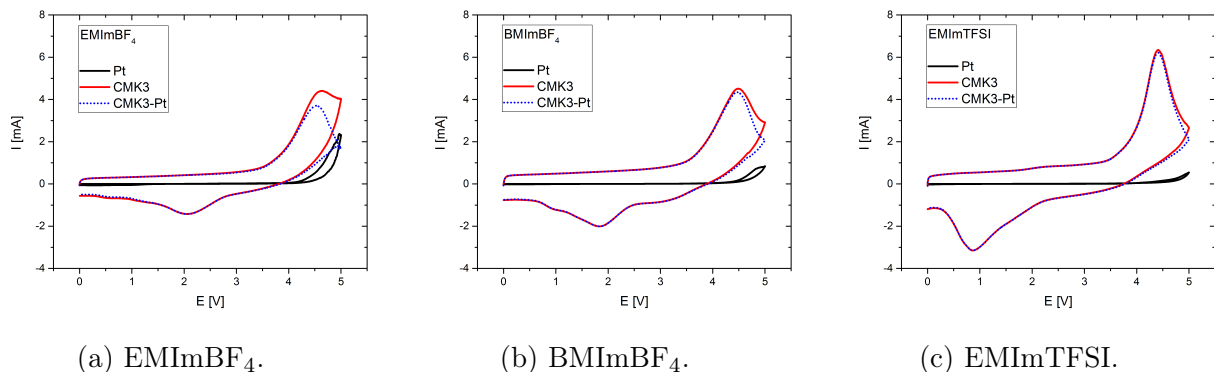


Figure 4.14.: Comparison of CV-measurements on CMK-3, platinum and the difference current.

show the noise resulting from that behaviour. From the current at maximum cell voltage one can estimate that the stability of the RTILs follows the order $\text{EMImBF}_4 > \text{BMImBF}_4 > \text{EMImTFSI}$. Moreover at the platinum electrode no reverse peak can be observed in contrast to the carbon sample. It can be therefore concluded that there is a second process taking place at the carbon electrode besides the electrolyte degradation. If the two processes are happening independently from each other, the current from the platinum electrode can be subtracted from the one on carbon as shown in figure 4.14, where the first cycle of CV-measurements of CMK-3 (red) in the three investigated RTILs are plotted together with the platinum background (black) and the difference between the two (blue dotted). Note that herein the current is plotted, not normalized to the mass of the electrode, although electrodes from the same carbon usually have roughly the same mass. The peak on the forward scan begins at similar potentials for all three ionic liquids around one Volt earlier than the decomposition of electrolyte on platinum. The correction mostly affects the region of the cyclic voltammogram after the peak having the highest impact on EMImBF_4 . The signal on the backward scan is present only in carbon samples and is positioned around 2 V for EMImBF_4 and BMImBF_4 and around 1 V for EMImTFSI . If the reverse peak belongs to the backward process of the first peak, then the peak separation is unusually high. Due to the fact that even after subtraction of the background there is still a current flowing, there must also be electrolyte decomposition happening on the surface of the carbon. However, this approach yields more symmetrical curves that resemble classical CV-measurements even less than the raw data. These findings plead against a redox reaction being alone responsible for the characteristic shape of the presented cyclic voltammograms. Carbons from the STC series have also been subjected to cyclic voltammetry in the three ionic liquids. In all cases

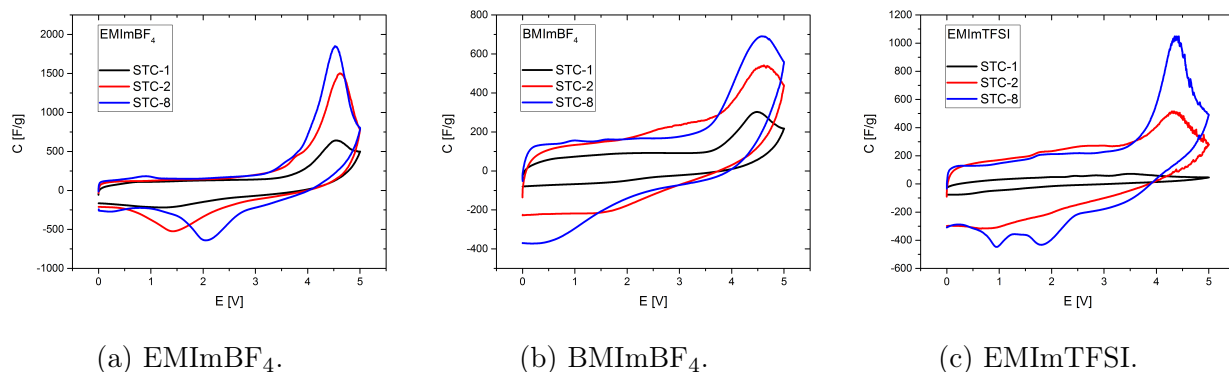


Figure 4.15.: Cyclic voltammograms of STC-1, -2 and -8 in EMImBF₄, BMImBF₄ (0-5.0 V, $\nu = 2 \text{ mV s}^{-1}$).

the forward peak size (height and area) increases from STC-1 to STC-8, which is clearly connected to the total mesopore volume of the carbon material studied. Also the size of the ions plays an important role in those measurements; for EMImBF₄ and BMImBF₄, with their compact BF₄⁻ anions and imidazolium cations with small or at least flexible alkyl chains (see figure 4.10) the peak is even visible in STC-1, which is mainly microporous with a small fraction of mesopores sized around 2.5 nm. In these ionic liquids even the reverse signal that scales with the mesopore volume can be measured. For the combination of EMIm⁺ and the bulky and rigid TFSI⁻ anion the high potential peak is only present for carbons with more and larger mesopores STC-2 and STC-8, while on STC-1 the current only levels off until it almost reaches zero and of course no signal appears on the backwards scan. In STC-2 and STC-8 reverse signals have been measured, particularly interesting is STC-8, where two distinct peaks appear in the CV. The area of the backward peak (if present) and therefore the amount of charge stored during the process is between 62 and 72 % of the forward peak, meaning that if those two peaks can be assigned to the same process, it is not completely reversible. These results imply that the process taking place at the carbon apart of electrolyte corrosion requires the presence of pores large enough to accommodate a certain amount of ions. If these pores are not available, no peak will be measured, despite the fact that a potential chemical reaction could easily take place at the outer surface of the carbon particles. Based on the previous measurements one could imagine that a process resembling the one in the micropores is happening also on mesopores with suitable sizes where ions adsorbed on the electrode undergo a structural rearrangement entering a more or less ordered state than the initial one. Mesopores of a suitable size are a necessary requirement for this process, as they are assumed to stabilize the formation of the new structure in analogy to

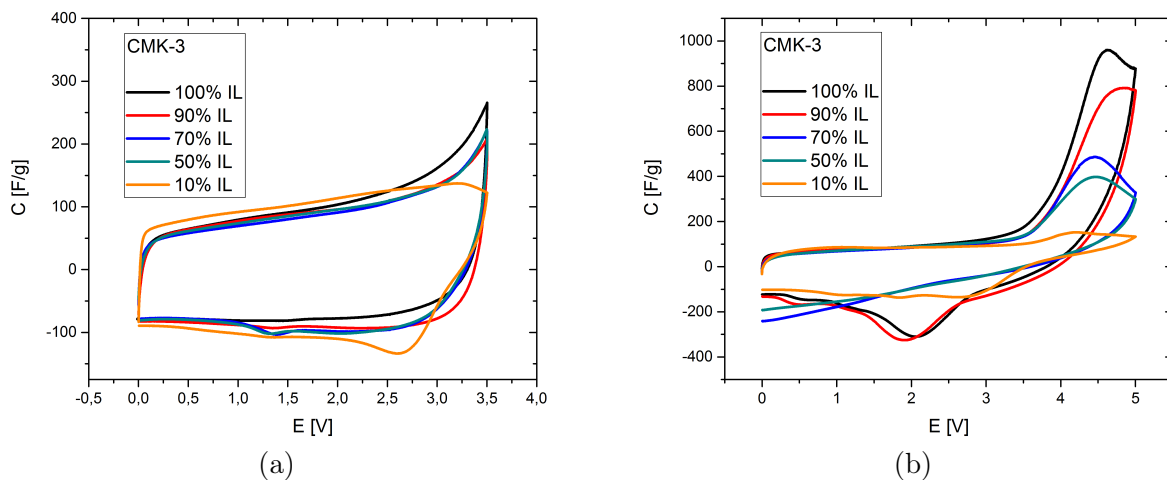


Figure 4.16.: Cyclic voltammograms of CMK-3 in different concentrations of EMImBF₄ ((a) 0-3.5 V, (b) 0-5.0 V, $\nu = 2 \text{ mV s}^{-1}$).

the meniscus formation of adsorbed gas. This is only possible in an electrolyte composed of pure ionic liquid, where the ions can interact directly with each other without an additional dielectric. To prove this point EMImBF₄ was diluted with adiponitrile, an organic solvent that is stable in an extremely wide electrochemical window ($\approx 8 \text{ V}$) in volume percentages of 90, 70, 50, and 10 % and cyclic voltammetry was measured on CMK-3. In figure 4.16a cyclic voltammograms of CMK-3 in the potential range of 0 to 3.5 V are depicted. The differential capacitance remains roughly the same throughout the concentrations of 100 to 50 % but experiences an increase for a 10 vol% electrolyte. Figure 4.16b shows the first cycle of the measurement up to 5 V. From the classical electrochemical point of view one would expect a linear decrease of the peak current with the concentration of electrochemically active species. This is clearly not the case in the presented measurements. Instead the forward peak current decreases slightly at 90 vol% of ionic liquid concentration, while the reverse peak remains almost unchanged (see table 4.5). At concentrations of 70 and 50 vol% the forward peak currents are reduced more abruptly and the reverse peak is smeared out and not recognizable any more, at 10 vol% EMImBF₄ almost no forward peak is visible. Another interesting observation from this measurement is that on the backward scan of the last measurement the current remains close to zero until almost 3 V and only from then a constant negative current sets in that can be described as mainly capacitive. Note that 10 vol% corresponds to 0.65 mol l^{-1} , so a too low concentration of ions is not likely to be the reason for this behaviour. The charge stored during the process was estimated from the integration of the current over the time, taking the connection between start and endpoint

of the integral as a baseline. It turns out that the charge of forward and backward scan are constant between 100% and 70% of ionic liquid concentration and roughly equal to each other. Although this is indicative of a reversible process, the results of the integration are not very accurate as the end of the peak is not visible in every measurement and therefore can be regarded only as an estimate.

Table 4.5.: Concentrations of EMImBF₄ in the electrolyte in vol% and mol l⁻¹ and charge stored in forward and backward peaks.

C_{EMImBF_4} [%]	C_{EMImBF_4} [mol l ⁻¹]	Q_f [C g ⁻¹]	Q_r [C g ⁻¹]
100	6.50	73.0	76.4
90	5.85	72.1	74.4
70	4.55	79.4	-
50	3.25	57.3	-
10	0.65	-	-

This experiment gives some insights into the nature of room-temperature ionic liquids under mesopore confinement at high electrode potentials. At first, ions of the oppsite charge of the electrode are adsorbed to the carbon surface; an electrochemical double layer is formed until no further adsorbable ions are present in the electrolyte any longer. In the CV this corresponds to the decrease of current from potentials higher than 3.5 V in 10 vol% EMImBF₄.

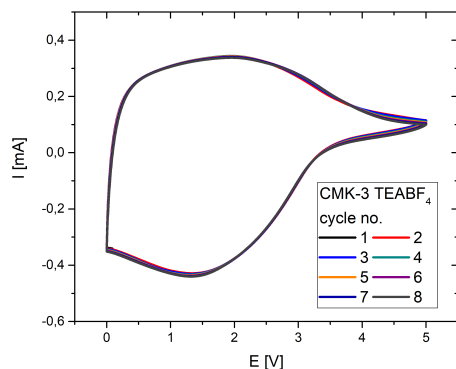


Figure 4.17.: Cyclic voltammetry of CMK-3 in 0.5 mol l⁻¹ TEABF₄ in adiponitrile.

For low concentrations of RTIL the energy storage mechanism follows a simple double layer compression mechanism, where with increasing potential more and more ions gather at the electrode surface until they are maximally close to each other. The same process can be observed in the CV measurement of a solution of 0.5 mol l⁻¹ tetraethylammonium tetrafluoroborate (TEABF₄) in adiponitrile as seen in figure 4.17. It has a very similar CV signature to that of the measurement of EMImBF₄ in 10 vol% concentration with a nearly constant current up

to potentials of 3.4 V and leveling off at higher cell voltages. The backward scan is almost symmetrical to the forward one and the experiment can be repeated at least eight times without significant change in current. This measurement not only proves that the anion, which is otherwise prone to hydrolysis or other decomposition pathways and thus a bottle-

neck for the electrochemical stability, is inert in the chosen potential range, but also that the formation of an electrochemical double layer can indeed run into a limitation under specific circumstances. At higher ionic liquid concentrations enough ions are available to allow the complete coverage of the carbon surface with several monolayers of unsolvatized ions of the ionic liquid. The thickness of one monolayer is therefore equal to the ion diameter. For such an electrolyte given a flat and homogenous electrode surface ions are expected to adsorb to the surface in a monolayer upon charging the cell. Due to intermolecular effects between the ionic liquid ions, the charge of the electrode is overcompensated by the layer in direct contact with the electrode, the Stern layer, which results in the formation of a second monolayer, with an excess of counter ions. All in all electroneutrality is conserved. This process, which is known as *overscreening*, occurs already at small potentials (< 1 V) and remains present even at higher voltages. Further charging leads to the expansion of the first monolayer into a multilayer of ions of the same charge, known as *crowding*. This double layer model can barely be applied in confined space, like in a mesopore of carbon because i) the pore is too narrow to accomodate such a large amount of ions and ii) while on a flat surface the double layer expands into the bulk electrolyte, in a pore two opposite double layers can only spread into the bulk until they have to interact with each other. Therefore, a completely different electrolyte structure can be present at high potentials inside of a mesopore.

Of course it is known from several other fields that matter confined in porous materials can behave in a totally different manner than in bulk. Ionic liquids break their intrinsic coulombic ordering, gases liquify at lower pressures via capillary condensation. Therefore it can be proposed that if the pore size is right and the electrolyte is not too dilute, at higher potentials, when already one or multiple monolayers are formed at the electrode surface, the electrolyte undergoes a structural transition into a differently ordered state. This leads to a change in coordination number and the coordination energy of the ions is released into the electrode walls. This in turn, can be measured with voltammetric methods. A connection between pore volume and height of the phase transition peak was established until now for three systematically chosen RTILs, while the size of the ions were also taken into account. As can be easily imagined, the presence of a dielectric has an important influence on the possibility of formation of such ordered structures, so that the non-linear behaviour of the peak height on the electrolyte concentration can serve as another evidence for this concept.

4.2.3. Influence of Lithium-Salts

Due to its small size and high charge density Li-ions can exhibit strong coordinative or even covalent interactions with numerous compounds. Gouverneur et al.^[42] have conducted electrophoretic NMR on 0.25 and 0.50 M solutions of LiTFSI in EMImTFSI and LiBF₄ in EMImBF₄ to deduce the diffusion coefficients of Li⁺. They found that Li⁺ diffusion coefficients are mostly equal to those of the corresponding anion and also the charge of the diffusing species was not +1 as expected, but -1 and -2 respectively. They concluded that Li⁺ is not present as a free ion but rather in clusters like [Li(TFSI)₂]⁻ and [Li(BF₄)₃]²⁻.

In the work of Elbourne et al.^[22] atomic force microscopy (AFM) was performed on a highly ordered pyrolytic graphite (HOPG) surface covered with EMImTFSI at potentials between -0.3 and +0.3 V with and without addition of Li⁺ and Cl⁻ ions. They found the pure IL to be arranged in rows along the surface of HOPG grains with the EMIm⁺ ions adsorbed to the surface via π - π stacking interactions and the TFSI⁻ less ordered in between, especially at more negative potentials. Upon addition of 0.1 wt% the group was not able to detect the Li⁺ ions, but found an increase in size of the TFSI⁻ region. They could also show that Li⁺ adsorbs to the electrode surface at negative potentials more readily than EMIm⁺.

With these results in mind LiPF₆ was added in a concentration of 0.5 and LiTFSI in concentrations of 0.25, 0.50 and 1.00 mol l⁻¹ to EMImTFSI and the solutions were used as electrolytes. Although LiPF₆ was reported to be soluble similarly to LiTFSI,^[43] it was not possible to dissolve the former salt in higher concentrations than 0.5 mol l⁻¹ and even then the solution seemed turbid. The goal was, to see whether the presence of Li⁺ ions could change the appearance of the CV measurement by forming adducts or interfering with the structure of the double layer. The measurements were performed on the micro-/mesoporous carbon STC-8, because it showed the most complex cyclic voltammograms that were expected to be influenced most probably by Li⁺-salt addition. In figure 4.18 the CV-measurements are shown. In the potential range between 0 and 3.5 V no significant differences can be seen between Li-free and Li-containing electrolyte. Addition of LiPF₆ causes the forward peak to disappear and the two backward signals to smoothen. Interestingly the progress of the forward scan resembles very much that of STC-1 in EMImTFSI, where no phase transition could be observed due to small mesopores. Figures 4.18e and 4.18f show the subsequent voltammetry cycles until 5 V. It is evident that the shape remains nearly the same with LiPF₆ added and that the current is diminishing less during cycling than it is the case for the pure ionic liquid. 0.25 mol l⁻¹ LiTFSI in the electrolyte causes the peak height of the forward signal to increase slightly, but further increase of the concentration reduces its size

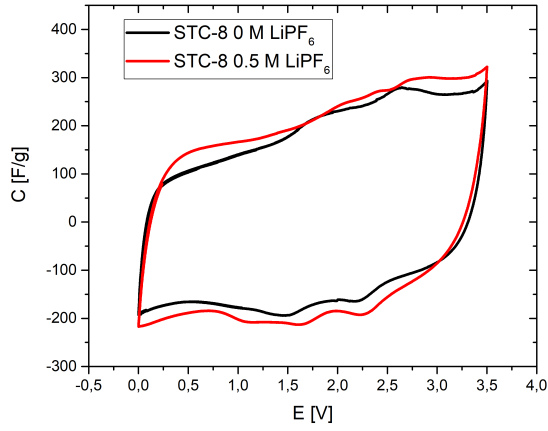
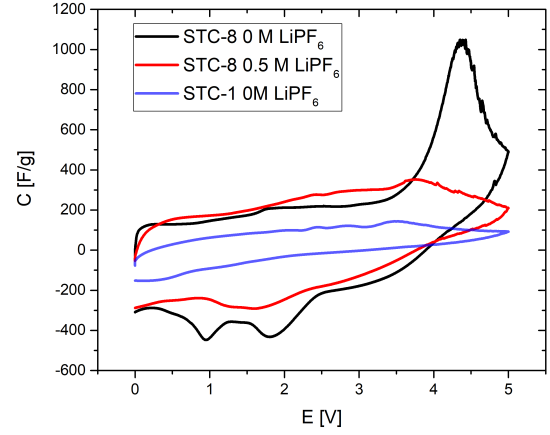
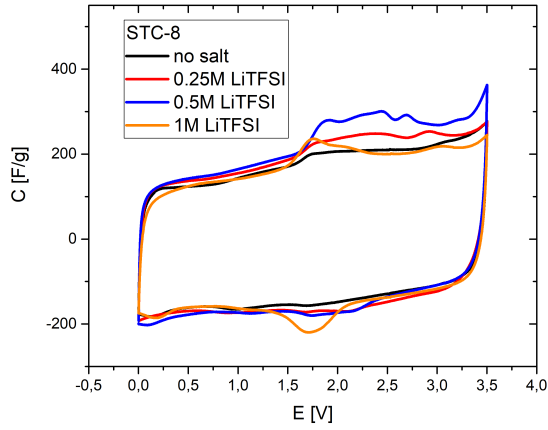
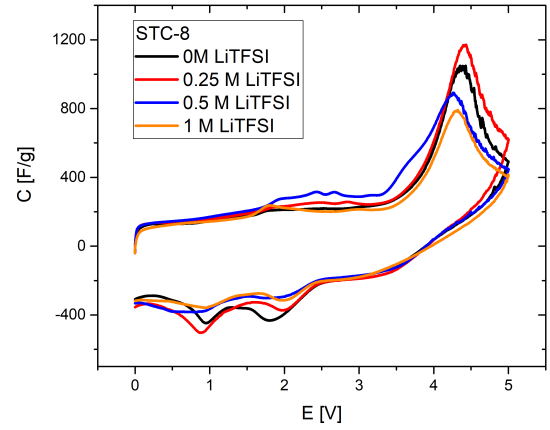
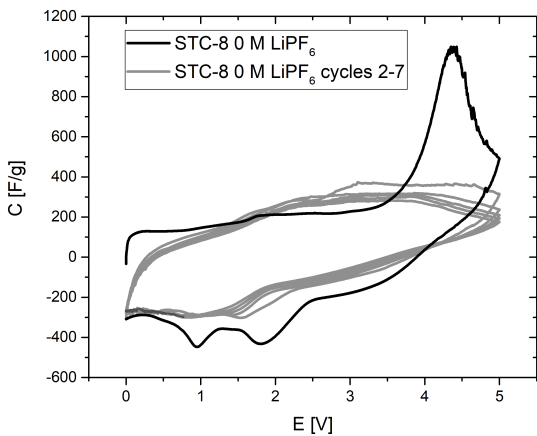
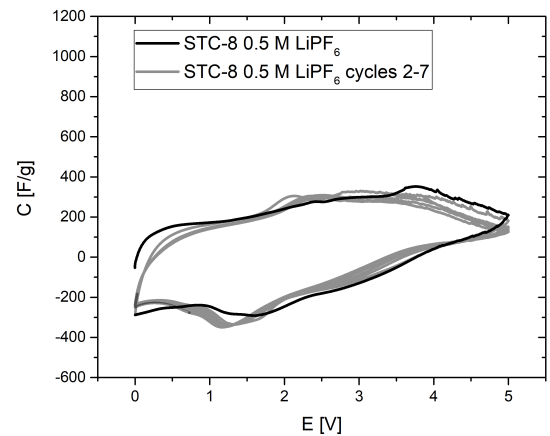

 (a) LiPF_6 0-3.5 V.

 (b) LiPF_6 0-5 V.

 (c) LiTFSI 0-3.5 V.

 (d) LiTFSI 0-5 V.

 (e) STC-8 without LiPF_6 cycling.

 (f) STC-8 with 0.5 M LiPF_6 cycling.

Figure 4.18.: Cyclic voltammograms of STC-8 with and without addition of LiPF_6 and LiTFSI . STC-1 without salt addition is shown for comparison in (b). Cycles 2-7 with and without addition of LiPF_6 ($\nu = 2 \text{ mV s}^{-1}$).

and also shrinks the two backward peaks. All in all the effect is not as extreme as it is with LiPF_6 . Addition of salts to the electrolyte was found to have a considerable impact on the voltammetric behaviour of an RTIL based capacitor. Introduction of Li^+ ions without another anion at 0.25 mol l^{-1} has almost no impact on the CV-curve, while higher concentrations cause the suspected phase transition peak to decrease in height, in both forward and backward directions. The fact that the heights of forward and backward peaks are scaling together points out that they originate from the same physical process. Li^+ ions therefore tend to impede the order/disorder transition at the electrode surface, but are neither able to prevent the decomposition of the electrolyte nor to influence the specific differential capacitance of the cell.

Dissolution of LiPF_6 however, caused the high potential peak as well as the two small ones on the reverse scan to disappear almost completely, which can be interpreted as the suppression of the said double layer rearrangement. It is standing to reason that this is due to the effect of the introduced PF_6^- anion influencing the structure of the electrochemical double layer. In crystallography it is a well known fact that highly symmetrical molecules usually have less crystal structure polymorphs than asymmetrical ones. With its octahedral symmetry, the PF_6^- anion could influence the adlayer structure in a way that the high-potential phase becomes more unfavorable, due to increased symmetry. Hence, it stands out to test other symmetrical anions' (e.g. BF_4^-) impact on double layer rearrangements. The findings from this experiment corroborate the concept of an ordering transition occurring in mesoporous carbons at high potentials, as there already exists experimental evidence for similar effects that is in line with the outcome of this work. Furthermore the other explanation for the CV signals, electrolyte degradation, seems unlikely to be influenceable by the addition of Li-salts to the ionic liquid.

4.2.4. Influence of Mesopore Diameter and Volume

The necessity of mesopores for the presumed phase transition at high electrode potentials has clearly been shown in previous sections. As a next step a relation between some basic properties of the mesopores and the peak height and potential, at which it occurs has to be established. Especially the influence of mesopore size and volume are subject to this investigation. A minimum pore size required can be estimated from previous measurements which lies between 2.5 and 4.0 nm, depending on ionic liquid composition, but is there also a maximum pore size, at which the stabilization of the new ionic liquid phase ceases? For this purpose, carbon materials templated with Aerosil®90 and Aerosil®380 were synthesized, the

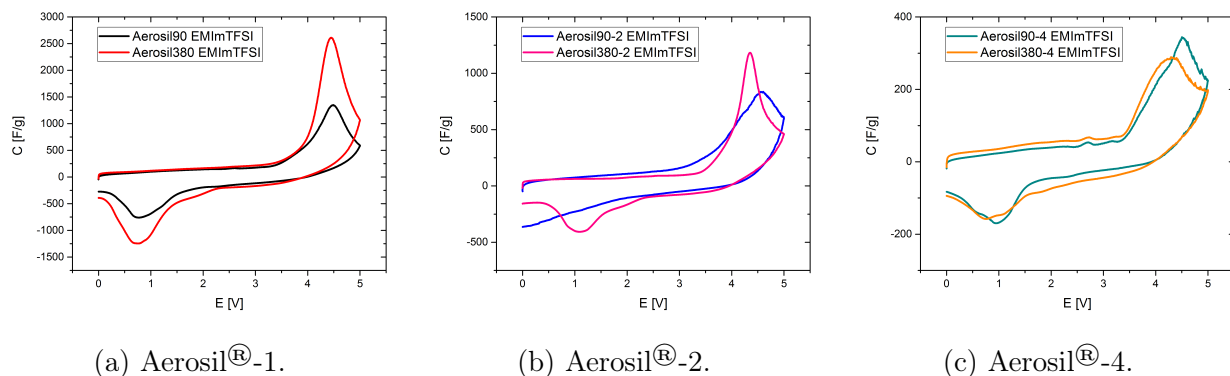


Figure 4.19.: Comparison of cyclic voltammograms of Aerosil[®]-carbons in EMImTFSI depending on pore sizes and pore volumes (0-5.0 V, $\nu = 2 \text{ mV s}^{-1}$).

pore sizes of which were centered around 8 and 16 nm, respectively. To make sure that effects from possible differences in pore volume of the different pore sized carbons are not confused with actual effects of pore size, the carbons have been prepared in different template ratios, so that the pore volume was also adjusted. Samples of two different pore sizes with three different pore volumes each were synthesized. The samples with the highest pore volume had additionally a large amount of external surface, the influence of which could also possibly be assessed here. In figure 4.19 cyclic voltammograms of Aerosil[®]s with different pore sizes in the three volume grades in EMImTFSI are presented that show that for a prevailing mesopore diameter of 8 nm the onset and maximum of the CV signal appears at lower potentials and with a higher peak current, except for Aerosil[®]-4, where the peak currents are almost similar. The same is measured similarly in the other two ionic liquids as can be seen in figures A.5 and A.6. If it is assumed that in the mesopores of 8 and 16 nm the same rearrangement process is taking place, then the occurrence of the peak at lower potentials in carbons with 8 nm pores corresponds directly to a lower activation energy at those materials. Therefore it does not seem reasonable, to assume that even larger pores are beneficial for the utilization of the structural change for energy storage. The peak height increases much more with increasing pore volume for smaller sized pores than for larger pores, being almost of equal height for Aerosil[®]-4 and much higher for the more porous Aerosil[®]-1. Even though there is a relationship to the BET surface area, the peak height increases much faster than the surface area as becomes evident from figure 4.20. Another remarkable observation is that BMImBF₄ has a much smaller peak current, which, while still scaling well with the pore volume, is less dependent on the predominant pore size of the carbon. That points out that the phase transition is less pronounced in this particular ionic liquid. At the same time

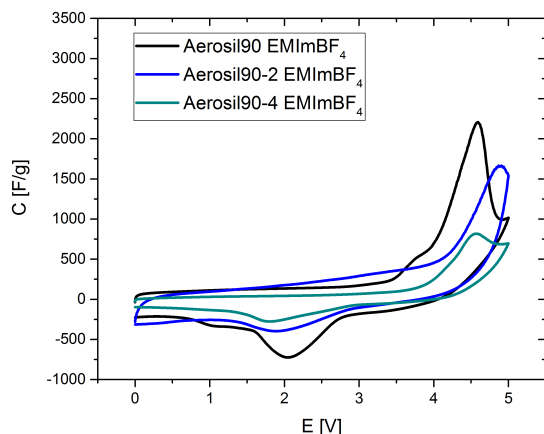
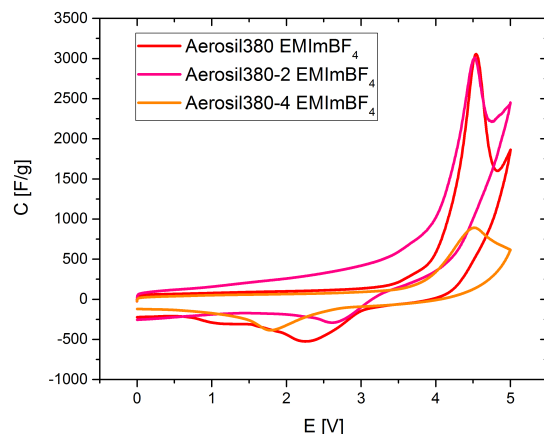
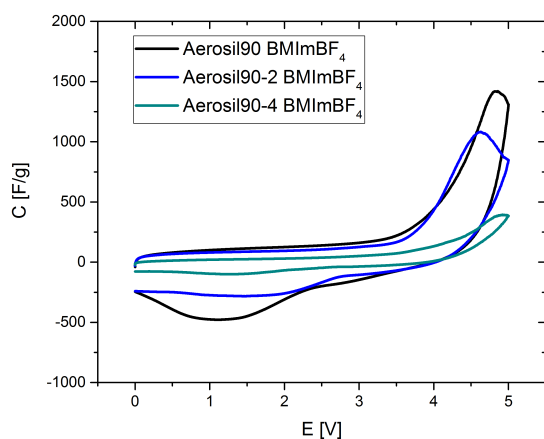
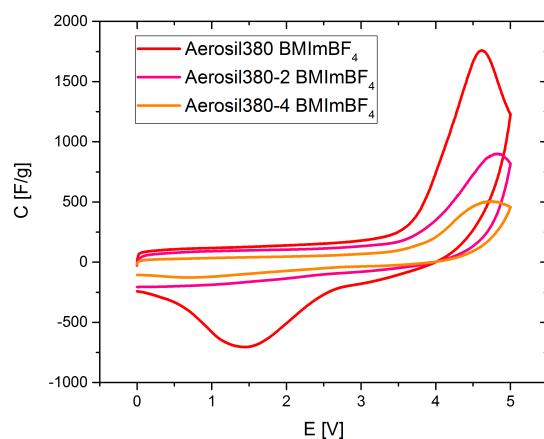
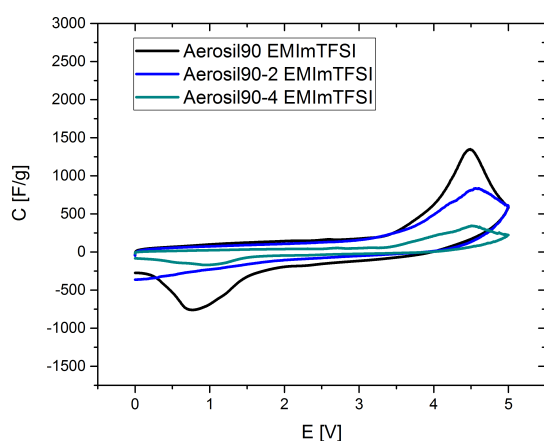
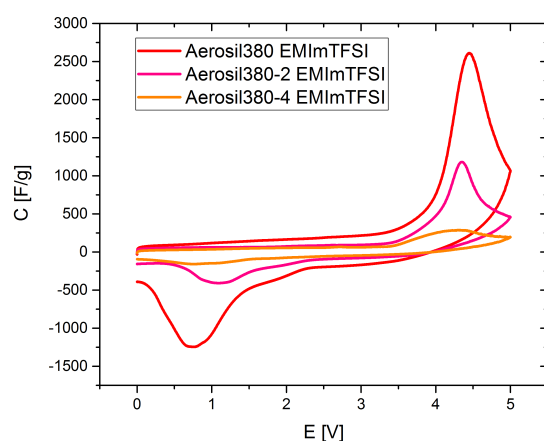

 (a) EMImBF₄ Aerosil[®]-90.

 (b) EMImBF₄ Aerosil[®]-380.

 (c) BMImBF₄ Aerosil[®]-90.

 (d) BMImBF₄ Aerosil[®]-380.

 (e) EMImTFSI Aerosil[®]-90.

 (f) EMImTFSI Aerosil[®]-380.

Figure 4.20.: Cyclic voltammograms of Aerosil[®]-carbons of different pore sizes depending on their pore volume in all three investigated ionic liquids (0-5.0 V, $\nu = 2 \text{ mV s}^{-1}$).

it is known that BMImBF₄, due to its high internal disorder induced by the comparably long alkyl chain is not able to undergo any kind of phase transitions even not having a melting point (see later sections). This parallel in phase change behaviour indicates against a faradaic character of the peak's origin.

4.2.5. Influence of Temperature

As for most of the physicochemical processes the temperature is expected to play a significant role for the potential induced phase transition observed in mesoporous carbon materials as well. Higher temperatures could either facilitate the rearrangement by destabilizing the coulombic ordering of the ionic liquid through thermal disordering and therefore lower the potential, at which the transition occurs. On the other side, if the discussion was to be based on the Gibbs-Helmholtz equation, one would expect the temperature to enter over the entropy term TdS .

$$dG = dH - TdS \quad (4.2)$$

If the enthalpy dH is negative and the new structure has a higher ordering, then the entropy should be negative and the value of TdS more negative for higher temperatures, so that dH becomes less negative and the other way around for a lower final ordering and a positive entropy. For a positive enthalpy value lower entropy in the new state corresponds to an even higher dG and vice versa for less ordered states with positive enthalpies. Unfortunately one cannot make a point about the thermodynamics of the process discussed here due to the lack of an external reference for the potential. One can only assume from general crystal structure analogies that coordination of more counterions into the solvation shell of an ion is connected to a decrease in energy for the system, and even this assumption is rather bold, as in the present case one probably has to deal with structures, where ions of same charge are in close proximity to each other, so that the question, whether coordination is energetically favorable or not remains subject to further research.

To obtain insights into this topic, cyclic voltammetry has been performed with EMImBF₄ on microporous carbon STC-1, where the high-potential peak was comparably small at room temperature, on carbon, with both, micro- and mesopores, STC-8, and ordered mesoporous carbon CMK-3 at 60 °C. In the last two cases the peak was very prominent already at room temperature.

One can see from these measurements that the peak does not become any higher in the cases of STC-1 and STC-8, but rather the background current increases. What can be observed

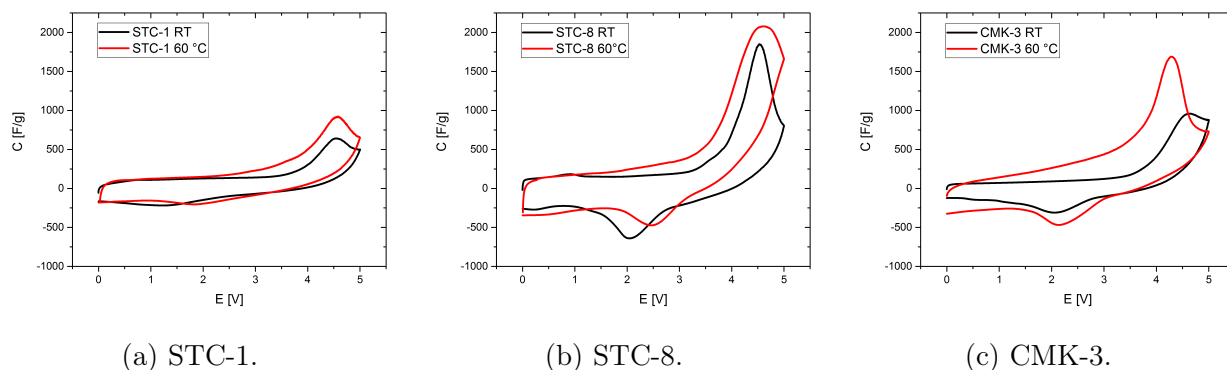


Figure 4.21.: Cyclic voltammetry on STC-1, STC-8 and CMK-3 in EMImBF₄ at room temperature and 60 °C (0-5.0 V, $\nu = 2 \text{ mV s}^{-1}$).

anyway, is the earlier onset of the peak current by approximately 300 mV. For CMK-3 the increase of temperature plays a much more significant role. There the beginning of the peak is located around 600 mV more negative than at room temperature and the heights of peak and background current are both significantly higher at an elevated temperature. Noteable is also the fact that forward and reverse peak are closer to each other at 60 °C, possibly indicating a more facile transition.

While this experiment all in all does not give as much information about the phenomenon under study as hoped, two conclusions can be drawn from it. The earlier onset of the peak and the lower separation of forward and backward reaction indicate towards a facilitation of the phase transition process, but as key properties of the electrolyte, such as viscosity and diffusion coefficient and therefore also the conductivity are functions of the temperature, their influence cannot be fully excluded. Possibly experiments at even higher temperatures would be more conclusive, but were not possible in the given cell setup. As will be seen in the following sections, other electrochemical techniques such as chronoamperometry could be even more useful to study temperature dependencies.

4.3. Differential Scanning Calorimetry

With differential scanning calorimetry it is possible to measure the heat flux caused by phase transitions such as melting, glass transition or crystal structure rearrangement during heating and cooling of a sample. The temperature at which the process occurs is also recorded. Therefore it can be possibly applied to find similarities between changes of the sample during heating and those that appear as a consequence of an electric potential. While

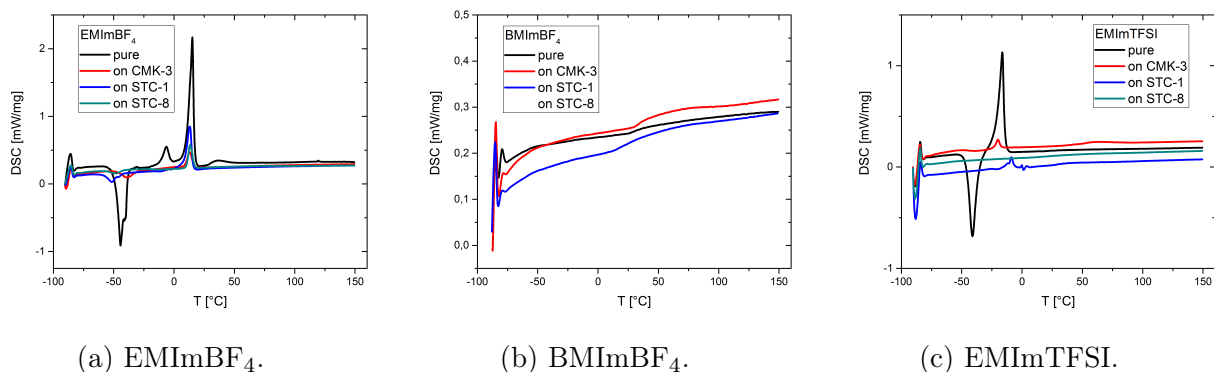


Figure 4.22.: DSC measurements of EMImBF₄, BMImBF₄ and EMImTFSI pure and confined in CMK-3, STC-1 and STC-8.

the calorimetric behaviour of pure ionic liquids has been already extensively studied,^[44,45] the measurements in this work are extended to ionic liquids under confinement in purely microporous (STC-1), mesoporous (CMK-3) and micro-/mesoporous carbon (STC-8). With this approach it was tried to find out, whether and in which way a porous environment can influence the phase transitions of an RTIL in general. For that, the ionic liquids were impregnated onto the carbon sample as described in the experimental section in such a ratio that all of the ionic liquid could be accommodated in the pores, i.e. the volume of the RTIL was always much lower than pore volume of the sample. The resulting DSC curves are depicted in figure 4.22. While the normalization of the heat flux in the diagrams refers to total sample mass, later enthalpy calculations consider the actual mass of ionic liquid in the sample.

Bulk EMImBF₄ was found to have two endothermic solid state rearrangements at temperatures of -44 °C and -6 °C, while in the literature those two are reported at lower temperatures of -58 °C and -18 °C respectively.^[44] While these findings could imply a systematic error as the values both differ by about 12 °C, the melting points found in this work and in the literature are practically identical (13 vs 15 °C). Note that Nishida et al.^[44] discuss the onset of the transition, while herein the peak temperature is considered, which explains the discrepancy of the melting points. The same group furthermore discusses a featureless DSC curve for BMImBF₄ (besides of a glass transition at -85 °C) as it was measured here. Pure EMImTFSI features a solid state transition at -41 °C and a melting point of -16 °C, which is in line with literature values.^[45] From integration of the peaks over time one can derive phase transition enthalpies according to equation 4.3. For ionic liquids impregnated on carbon the mass ratio of IL to carbon was taken into consideration as a factor in that equation, where x is the

Table 4.6.: Overview over temperatures (in °C) and molar enthalpies (in kJ mol⁻¹) of phase transitions observed in DSC.

	EMImBF ₄						EMImTFSI			
	SST ₁		SST ₂		fusion		SST ₁		fusion	
	<i>T</i> ₁	$\Delta_n G_1$	<i>T</i> ₂	$\Delta_n G_2$	<i>T</i> _f	$\Delta_n G_f$	<i>T</i> ₁	$\Delta_n G_2$	<i>T</i> _f	$\Delta_n G_f$
bulk IL	-45	-9.5	-6	1.4	15	13.0	-41	-12.7	-16.3	13.9
CMK-3	-40	-1.8	-	-	13	1.8	-38	-1.4	-20	1.5
STC-1	-51	-6.0	-	-	13	2.1	-	-	-9	2.8
STC-8	-48	-2.5	-	-	13	0.9	-	-	-	-

carbon/ionic liquid ratio and $\Delta_n G$ is the molar enthalpy of transformation.

$$\Delta_n G = xM \int_{t_{start}}^{t_{end}} P dt \quad (4.3)$$

The phase transition enthalpies have been calculated in this manner for all DSC peaks and can be taken from table 4.6. It is evident that a porous environment has a strong influence on temperatures as well as enthalpies of the RTILs' phase transitions. In EMImBF₄ the first solid state transition is found at slightly shifted temperatures from that in bulk and also the transition's enthalpy is significantly reduced by up to 83 %. The second solid state transition is not observed on carbon-confined ionic liquid at all and the melting process is found at reduced temperatures and proceeds at an enthalpy reduced by approximately one order of magnitude. Analogously, the for EMImTFSI the solid state transition is possible only in CMK-3 carbon with a $\Delta_n G$ of 1.4 kJ mol⁻¹. The melting point of EMImTFSI is likewise affected by pore confinement, but not as systematically as in EMImBF₄. The fusion enthalpies are reduced in the same fashion.

Two main conclusions can be drawn from DSC measurements. First, the phase transition suspected to be observed in cyclic voltammetry is most likely not one of those, thermally induced during DSC. If that would be the case, then BMImBF₄, which shows the respective signal in the CV, should also have a phase transition in the thermal analysis. Also it can be imagined that the short range structure is a completely different one with a high potential applied, than it is the case for the neutral ionic liquid. The second and even more important finding is that porosity can largely influence the phase transition behaviour of an ionic liquid (and probably also other compounds) in general, which can be explained by the concept that solid state rearrangements and melting processes require many particles to be in close contact to each other. In pore confinement this is not possible any more, as one ion can only

be surrounded by a few layers of other ions so that the new crystal phase can have only a very limited grain size. That implies that assuming a change in ion coordination of ionic liquids induced by application of an electric potential to a porous carbon surface is not too far-fetched.

4.4. Chronoamperometry

In cyclic voltammetry a linear potential ramp is applied to the cell, where a rather complex to describe competition between reaction kinetics and diffusion is induced, so that the current in classical, solvent based electrolytes traverses a peak that is caused by the nature of the measurement. On the other hand, in chronoamperometry the cell is subjected to a constant potential and the current-time response follows a solely diffusion controlled inverse square root proportionality as described by the Cottrell equation. In the case of a capacitor no chemical reaction occurs, but the double layer builds up according to the applied potential. If there is indeed a phase transition present that is triggered by an electrical potential, then it should be measurable not only in cyclic voltammetry, but also upon a potential acting on the electrode, depending on the type of cell either over the background of the Cottrell equation (in case of a chemical reaction) or a first order exponential decay (for a capacitor). By this reasoning, the following experiment has been performed on CMK-3 in EMImBF₄:

1. Conditioning of the cell in cyclic voltammetry during five cycles between 0 and 3.5 V at 2 mV s⁻¹ scanrate.
2. Discharging the cell to 0 V and stabilizing.
3. Charging to 4.0 V, which from previous CV-experiments should be sufficiently high, to trigger order/disorder transitions, but not yet in the decomposition region.
4. Discharging to OCP, to possibly see a relaxation process, opposite to that expected at 4.0 V.

Figure 4.23 shows the result of this measurement series. The first cycle is as expected featureless, unfortunately also the charging step to 4.0 V, both can be fitted well to a declining exponential function with the parameters of the cell ($C \approx 1$ F, $R \approx 7$ Ω). Most interesting is the relaxation step, as at OCP there can clearly be seen a signal underneath the normal capacitive behaviour. The signal could be reproduced even when the duration of

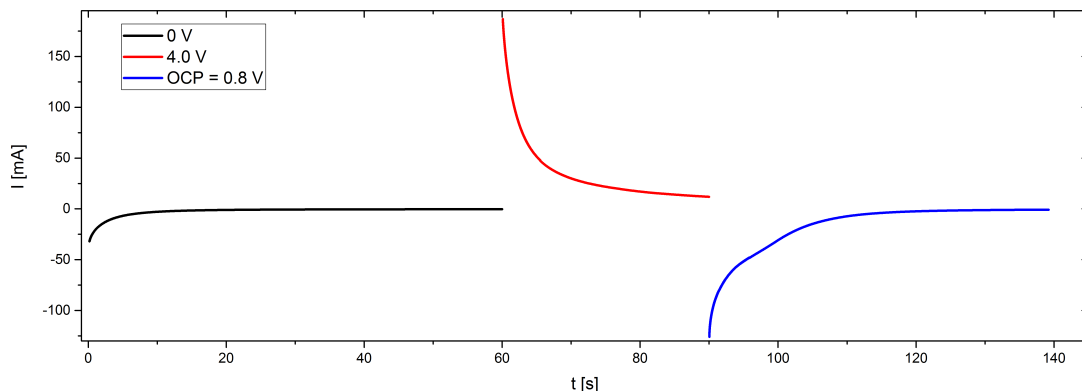


Figure 4.23.: Chronoamperometry of CMK-3. Conditioning at 0 V, charging at 4 V, discharging at OCP (0,8 V). "Shoulder" can be observed approximately 8 s after returning to OCP.

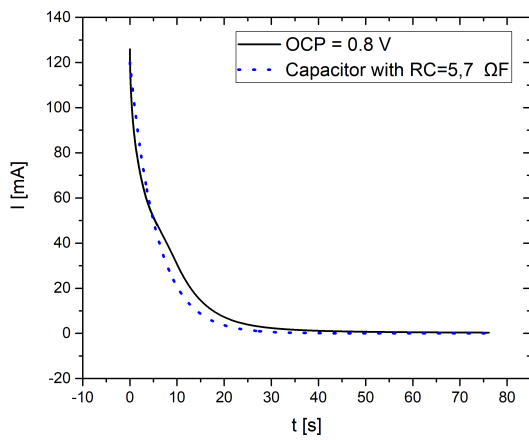
the individual steps or the charging potential are varied. It was therefore decided, to fit the background current with an exponential function.

$$I = I_0 \exp\left(-\frac{t}{RC}\right) \quad (4.4)$$

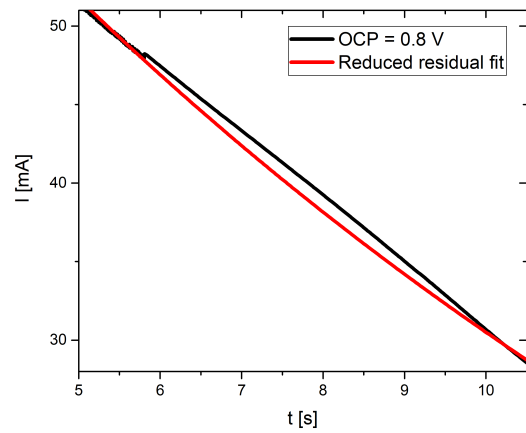
The chosen parameters R and C slightly deviate from the cell parameters, but reproduce the background current better as can be seen from figure 4.24a. The residual however still showed a significant fraction of interference from the capacitance, so the fit was restricted to the region more strictly around the suspected peak (figure 4.24b, to yield a residual as shown in figure 4.24c. It is important that position and shape of the residual do not differ significantly from that, generated from the one, matching the cell parameters. The residual contains the current i.e. the temporal change of charge plotted against the time, but we are interested in the charge difference between beginning and end of the phase transition. For that reason, the integral of the residual was calculated numerically with respect to time and the curve was normalized, so that the phase transition begins at $t = 0$ and fraction of the new phase $x_{phaseb} = 0$. The resulting curve (figure 4.24) was fitted to the JMAK equation (equation 2.7) and yielded a rate constant B of 0.12 s^{-k} and a JMAK exponent k of 2.25 was obtained. The latter can be interpreted to draw conclusions about the dimensionality of the phase transition and according to $k = 1 + D$ equals 1. While the rate constant is not very informative, the exponent k being very close to 2 implies that the structure change proceeds only into one direction, which is in line to the expectation that the potential induces a rearrangement perpendicular to the electrode surface. A potential triggered phase transition

of the ionic liquid that causes a change in surface charge on the electrode can therefore be regarded as proven. The only concerns about this measurement are that the current, caused by the rearrangement is rather small and that no corresponding signal can be found in the charging step. This could be due to a too high rate of the forward process, so that it happens already in the beginning of the potential step, when the current slope is still very steep and can consequently not be observed.

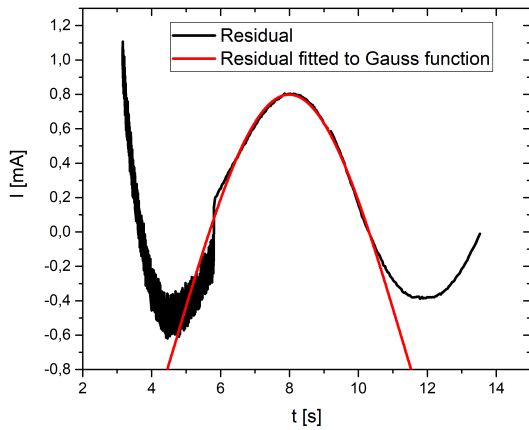
Discharging the cell at OCP on the other hand could render the reaction just slow enough,



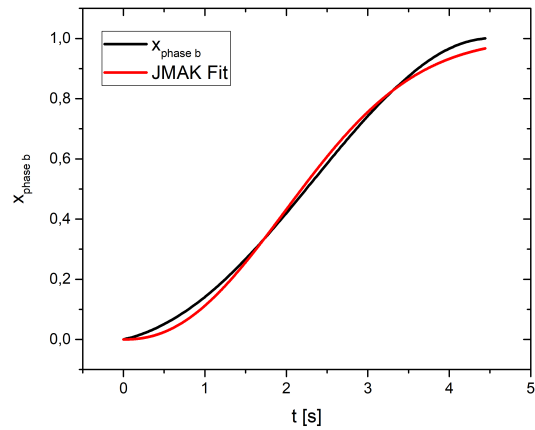
(a) Fit with actual cell parameters. $C \approx 1 \text{ F}$,
 $R \approx 7 \Omega$



(b) Fit of the enlarged region to reduce the local residual.



(c) Residual of the optimized background fitted to a Gauss function.



(d) Integral of the residual fitted to JMAK equation.

Figure 4.24.: Exponential decay fitted of the relaxation cycle of chronoamperometry and further analysis of the current anomaly.

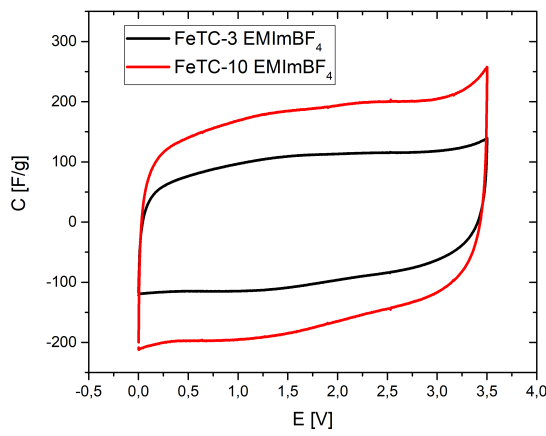
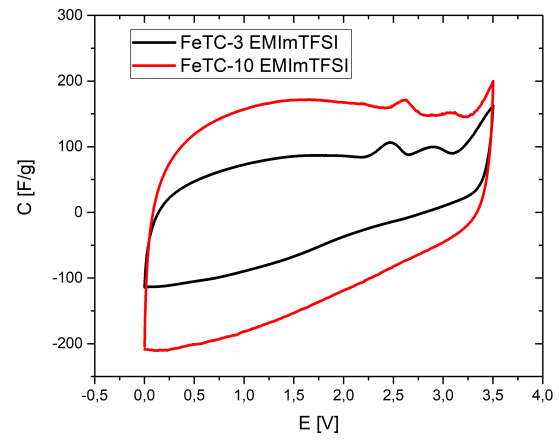
to be measurable at the chronoamperometry time scale. This experiment could be further supported, by extending the measurements to several temperatures, as the rate constant should show Arrhenius behaviour according to theory. Furthermore, other ionic liquid/carbon combinations should definitely be studied.

4.5. Iron(III)-chloride templated carbon

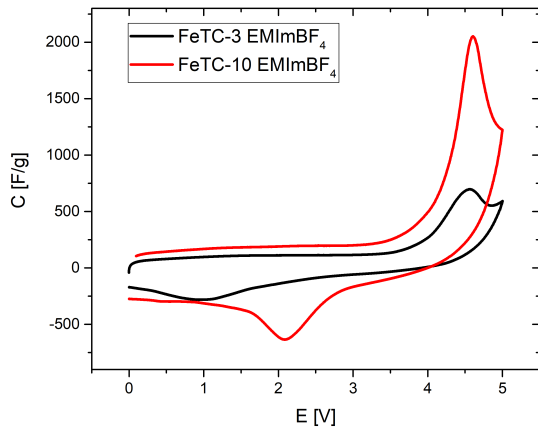
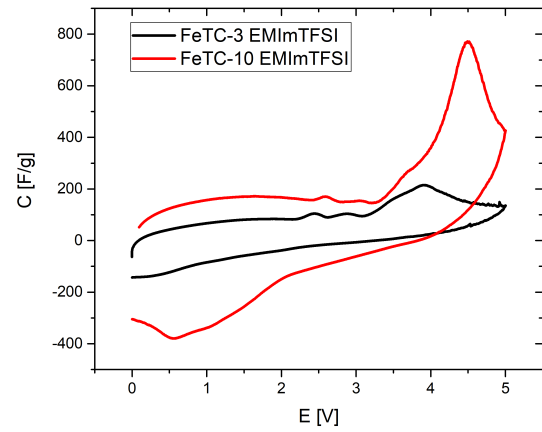
Finally, the newly prepared iron(III)-chloride templated carbon has been investigated in terms of its electrochemical properties. Cyclic voltammetry was conducted under the same conditions as previously in the potential ranges up to 3.5 V and 5.0 V in ionic liquids EMImBF₄ and EMImTFSI, as their CV-response has proved most sensitive to pore structure changes. Until 3.5 V FeTC-3 shows a comparable capacitance to that of STC-1 (87 F g⁻¹ vs 116 F g⁻¹ in EMImBF₄, as estimated from cyclic voltammetry) and for EMImTFSI it even has the same small peaks at 2.5 V and 3.0 V that have been ascribed to micropore filling and emptying previously. This underscores the relationship between micropore size and electrochemical properties. More interestingly, the addition of even a small degree of mesoporosity, as it is the case in FeTC-10 increases the capacitance from 87 F g⁻¹ to 172 F g⁻¹, even though the microporosity is decreased according to nitrogen and carbon dioxide physisorption. The features of the CV remain mostly the same. This has been similarly observed for the series of salt templated carbons from STC-1 to STC-2.

Extending the scan to higher potentials (5.0 V), the usual peak is observed in both materials and both ionic liquids. For their height, the same trend as before has been measured. While in EMImBF₄ for purely microporous carbon FeTC-3 only exhibits a small signal beginning at 3.7, running through a maximum at 4.6 V with a peak differential capacitance at 697 F g⁻¹, while the mesopore containing FeTC-10 shows the peak at the same potential but with a height of 2051 F g⁻¹. In EMImTFSI with its significantly larger anion the high potential peak is found at somewhat lower potentials (onset: 3.3 V, peak 3.9 V) with a maximum differential capacitance of 215 F g⁻¹ in FeTC-3, while in FeTC-10 it occurs as always at 4.6 V and comprises a differential capacitance of 767 F g⁻¹. The peak currents are therefore lower in both carbons in EMImTFSI due to its larger ions and the peak is significantly larger in carbons with even small volumes of mesopores. Templating with iron(III)-chloride can therefore provide a carbon of considerable value for the use as an electrode material in supercapacitors, while the exact synthesis conditions are yet to be optimized. The electrochemical properties can be tuned in a similar way as in ZnCl₂ derived materials.

However, the actual viability of these carbons that made them worth mentioning herein, is that they prove the structure-property relationship between pore size distribution and electrochemical behaviour during CV measurements, as now a material derived from different porogens and synthesis conditions behaves in the exactly the way, it is predicted by its pore structure. Once again it is proved that micropores, large enough to accomodate the ionic liquid enable an energy storage mechanism that is related to their filling and emptying. Moreover, mesoporosity of minimum suitable size leads to a jump wise increase in capacitance and is necessary to induce the phase transition peak.


 (a) EMImBF₄.


(b) EMImTFSI.


 (c) EMImBF₄


(d) EMImTFSI.

Figure 4.25.: Cyclic voltammograms of FeTC-3 and FeTC-10 in EMImBF₄ and EMImTFSI ((a) and (b) 0-3.5 V, (c) and (d) 0-5.0 V, $\nu = 2 \text{ mV s}^{-1}$).

5. Conclusion and Outlook

The interaction of RTILs with porous carbon electrodes in supercapacitor applications was studied by means of cyclic voltammetry on systematically chosen carbon/electrolyte combinations. The energy storage mechanism of such devices was elucidated and can be attributed to two physical processes.

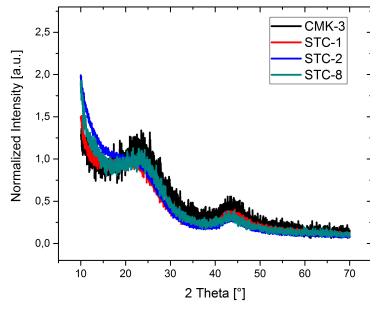
Pore filling and emptying was observed to have an important influence on the differential capacitance of an EDLC cell especially at lower potentials. Using carbons with micropores slightly larger than the RTIL ions in diameter (i.e. ZnCl_2 templated carbons) as the electrodes has been found to vastly increase the capacitance of the cell regardless of the RTIL studied. Additionally, only in those carbons were measured small reversible CV peaks at rather low cell voltages, the shape and potential of which was specific for each RTIL and particularly dependent on the RTIL's anion. From these results it was obvious, that the peaks appear, when ions enter the previously empty carbon micropores, leading to a transient increase of surface charge density and an increased specific capacitance.

The second mechanism occurs at higher potentials and can be attributed to a structural rearrangement of the electrochemical double layer. It is measured as a current peak in the CV, beginning at cell voltages of 3.5 V and higher and was observed only in mesoporous carbons with pore diameters above 3-4 nm, especially for larger anions. As a peak of comparable size is also observed in the backward scan, the process may be even reversible. The signal can be strongly influenced by electrolyte dilution and addition of salts to the electrolyte and proceeds independently of electrolyte degradation. The peak occurs at lower potentials in smaller mesopores and the size of the peak correlates well with the mesopore volume. The charging process at a mesoporous carbon electrode can therefore be described as follows: RTIL ions are adsorbing to the electrode surface until a full monolayer coverage is achieved. When the potential is further increased, the charge of the electrode is reaching out into the bulk of the electrolyte, causing multilayer adsorption of co-ions to the pore walls. At some point the entire mesopore is filled mostly with co-ions, that undergo a phase transition upon reaching a certain potential. The energy difference between old and new phase can be exploited for energy storage.

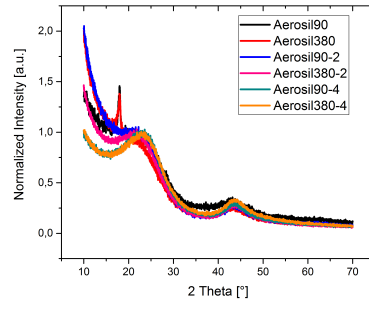
The presence of a potential induced phase transition proved with chronoamperometry and even its dimensionality of propagation could be identified. By subjecting the cell to its OCP after charging it at 4.0 V for 30 s, a peak was measured in addition to the capacitive current. As the current corresponds to a change in charge with respect to time and the charge in the cell is different before and after the phase transition, the current peak could be integrated and normalized to obtain a sigmoidal curve, that represents the extent of transformation of the initial to the final phase. Fitting this curve to the established nucleation and growth kinetics indicated a one-dimensional growth of the new phase.

During this work only the pore structure of the carbon was considered. Future studies could focus more on the chemical surface properties and investigate the effect of introduction or removal of functional surface groups, e.g. by reduction under hydrogen atmosphere, oxidation or nitrogen doping. Maybe even a porous non-carbon material could be considered. Of course, variation of the ionic liquid would possibly yield more interesting results. Most importantly, the attempt should be undertaken, to directly prove the structural rearrangement by means of X-ray or neutron diffraction or scattering techniques, before and after cycling to different potentials or in the best case even *in situ*, as the in depth comprehension of the phenomenon is the key to its utilization in future applications.

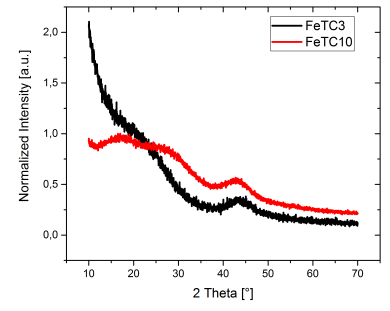
A. Appendix



(a) STCs and CMK-3.

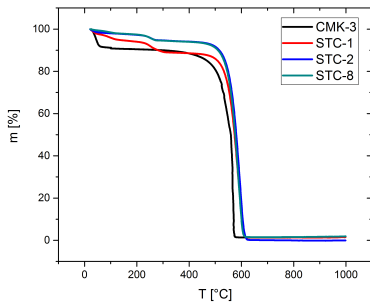


(b) Aerosil[®]-carbons.

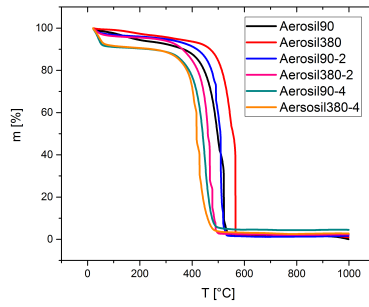


(c) FeTC.

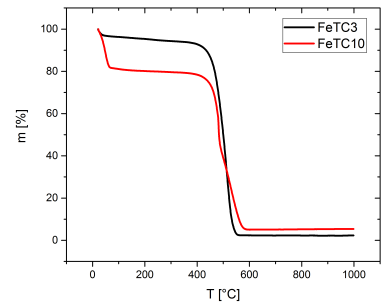
Figure A.1.: XRD-patterns of investigated carbons.



(a) STCs and CMK-3.



(b) Aerosil[®]-carbons.



(c) FeTC.

Figure A.2.: Thermogravimetric analysis of investigated carbons.

APPENDIX

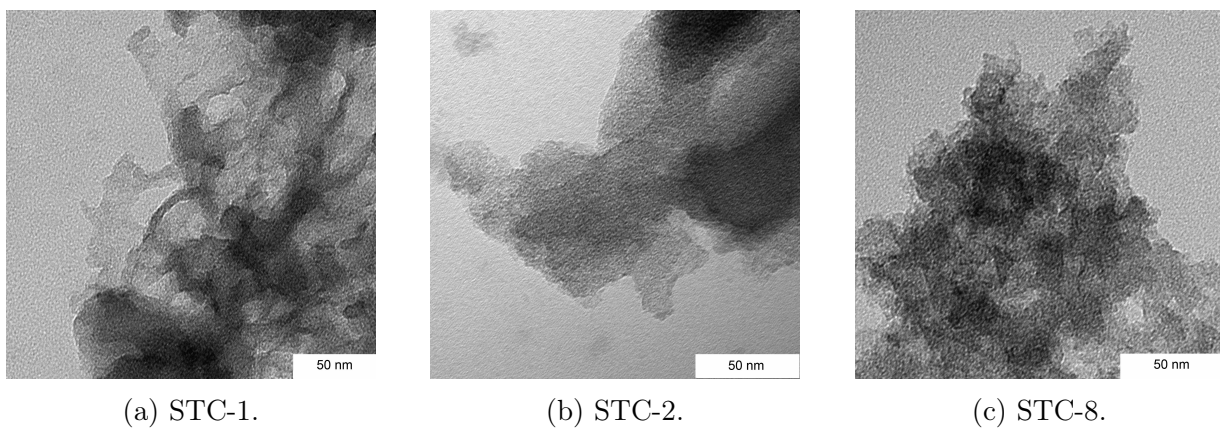


Figure A.3.: TEM images of STCs.

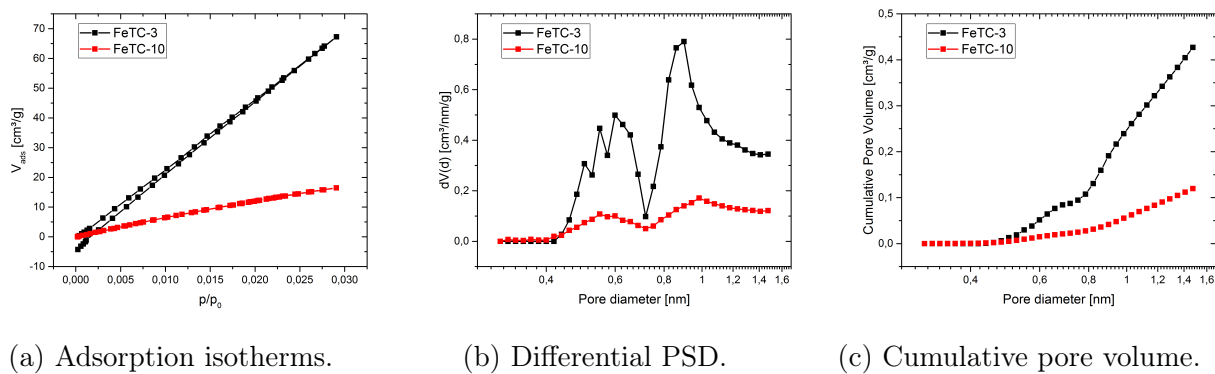


Figure A.4.: CO₂ physisorption measurements at 273 K and corresponding pore size distributions of iron(III)-chloride templated carbons.

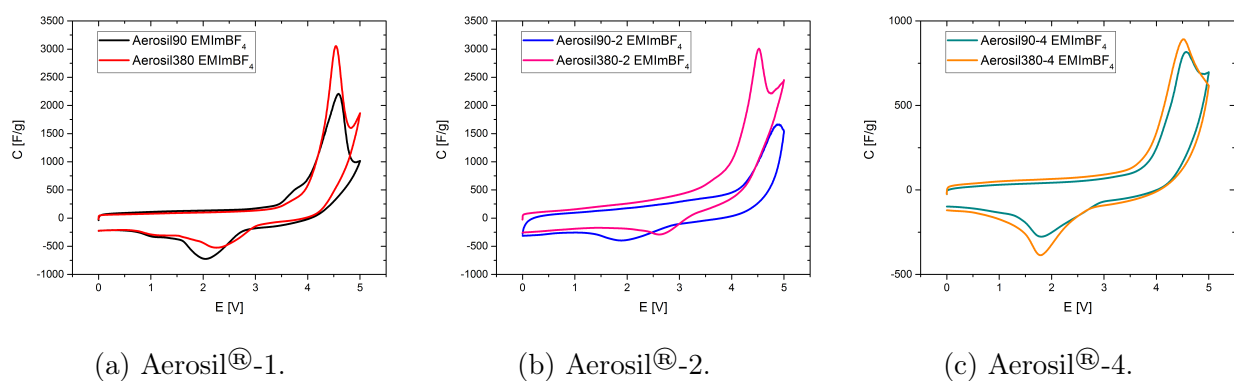
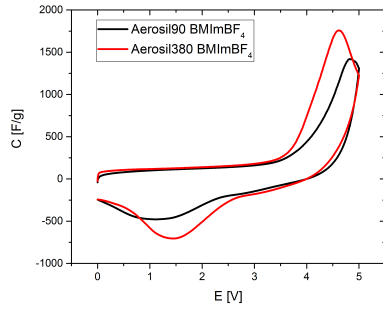
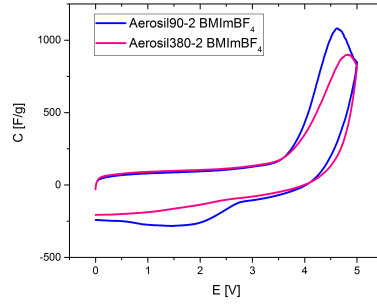


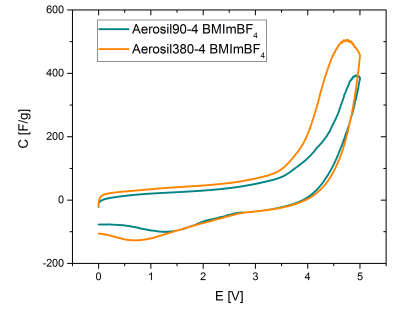
Figure A.5.: Comparison of cyclic voltammograms of Aerosil®-carbons in EMImBF₄ depending on pore sizes and pore volumes.



(a) Aerosil[®]-1.



(b) Aerosil[®]-2.



(c) Aerosil[®]-4.

Figure A.6.: Comparison of cyclic voltammograms of Aerosil[®]-carbons in BMImBF₄ depending on pore sizes and pore volumes.

Bibliography

- [1] A. Manthiram, *ACS Central Science* **2017**, *3*, 1063–1069.
- [2] A. González, E. Goikolea, J. A. Barrena, R. Mysyk, *Renewable Sustainable Energy Reviews* **2016**.
- [3] K. Kiyohara, T. Sugino, K. Asaka, *The Journal of Chemical Physics* **2011**, *134*, 154710.
- [4] M. V. Fedorov, A. A. Kornyshev, *Chemical reviews* **2014**, *114*, 2978–3036.
- [5] R. Futamura, T. Iiyama, Y. Takasaki, Y. Gogotsi, M. J. Biggs, M. Salanne, J. Ségalini, P. Simon, K. Kaneko, *Nature Materials* **2017**, *16*, 1225–1232.
- [6] C. Largeot, C. Portet, J. Chmiola, P.-L. Taberna, Y. Gogotsi, P. Simon, *Journal of the American Chemical Society* **2008**, *130*, 2730–2731.
- [7] R. Yan, M. Antonietti, M. Oschatz, *Advanced Energy Materials* **2018**, 1800026.
- [8] R. Hayes, G. G. Warr, R. Atkin, *Chemical reviews* **2015**, *115*, 6357–6426.
- [9] P. Walden, *Bulletin of the Russian Academy of Sciences* **1914**.
- [10] M. Galiński, A. Lewandowski, I. Stepniak, *Electrochimica acta* **2006**, *51*, 5567–5580.
- [11] B. Welch, R. Osteryoung, *Journal of Electroanalytical Chemistry and Interfacial Electrochemistry* **1981**, *118*, 455–466.
- [12] J. S. Wilkes, M. J. Zaworotko, *Journal of the Chemical Society Chemical Communications* **1992**, 965–967.
- [13] P. Bonhote, A.-P. Dias, N. Papageorgiou, K. Kalyanasundaram, M. Grätzel, *Inorganic chemistry* **1996**, *35*, 1168–1178.
- [14] J. P. Hallett, T. Welton, *Chemical Reviews* **2011**, *111*, 3508–3576.
- [15] B. A. Neto, E. C. Meurer, R. Galaverna, B. J. Bythell, J. Dupont, R. G. Cooks, M. N. Eberlin, *The journal of physical chemistry letters* **2012**, *3*, 3435–3441.
- [16] H. Weingärtner, A. Knocks, W. Schrader, U. Kaatze, *The Journal of Physical Chemistry A* **2001**, *105*, 8646–8650.

- [17] E. I. Izgorodina, D. R. MacFarlane, *The Journal of Physical Chemistry B* **2011**, *115*, 14659–14667.
- [18] M. A. Gebbie, M. Valtiner, X. Banquy, E. T. Fox, W. A. Henderson, J. N. Israelachvili, *Proceedings of the National Academy of Sciences of the United States of America* **2013**, *110*, 9674–9679.
- [19] B. Rotenberg, M. Salanne, *The Journal of Physical Chemistry Letters* **2015**, *6*, 4978–4985.
- [20] R. Wen, B. Rahn, O. M. Magnussen, *Angewandte Chemie (International ed. in English)* **2015**, *54*, 6062–6066.
- [21] M. Z. Bazant, B. D. Storey, A. A. Kornyshev, *Physical Review Letters* **2011**, *106*, 046102.
- [22] A. Elbourne, S. McDonald, K. Voïchovsky, F. Endres, G. G. Warr, R. Atkin, *ACS Nano* **2015**, *9*, 7608–7620.
- [23] F. Lai, J. Feng, R. Yan, G.-C. Wang, M. Antonietti, M. Oschatz, *Advanced Functional Materials* **2018**, *28*, 1801298.
- [24] E. Wiberg, N. Wiberg, *Lehrbuch der anorganischen Chemie*, Walter de Gruyter & Co., Berlin, New York, **1995**.
- [25] N. Fechler, T.-P. Feller, M. Antonietti, *Advanced Materials* **2013**, *25*, 75–79.
- [26] S. Jun, S. H. Joo, R. Ryoo, M. Kruk, M. Jaroniec, Z. Liu, T. Ohsuna, O. Terasaki, *Journal of the American Chemical Society* **2000**, *122*, 10712–10713.
- [27] M. Oschatz, S. Boukhalfa, W. Nickel, J. Lee, S. Klosz, L. Borchardt, A. Eychmüller, G. Yushin, S. Kaskel, *Journal of Materials Chemistry A* **2014**, *2*, 5131–5139.
- [28] D. Barrera, M. Dávila, V. Cornette, J. A. de Oliveira, R. H. López, K. Sapag, *Micro-porous and Mesoporous Materials* **2013**, *180*, 71–78.
- [29] L. Borchardt, M. Oschatz, S. Kaskel, *Materials Horizons* **2014**, *1*, 157–168.
- [30] M. Avrami, *The Journal of chemical physics* **1939**, *7*, 1103–1112.
- [31] M. Avrami, *The Journal of Chemical Physics* **1940**, *8*, 212–224.
- [32] M. C. Weinberg, D. P. Birnie III, V. A. Shneidman, *Journal of non-crystalline solids* **1997**, *219*, 89–99.
- [33] M. Fanfoni, M. Tomellini, *Il Nuovo Cimento D* **1998**, *20*, 1171–1182.

- [34] A. J. Bard, L. R. Faulkner, *Electrochemical Methods: Fundamentals and Applications*, 2nd ed., Wiley, **2001**.
- [35] S. Kondrat, N. Georgi, M. V. Fedorov, A. A. Kornyshev, *Physical Chemistry Chemical Physics* **2011**, *13*, 11359.
- [36] A. D. McNaught, A. Wilkinson, *Compendium of Chemical Terminology*, 2nd ed., Wiley Blackwell, **1997**.
- [37] P. Yang, D. Zhao, B. F. Chmelka, G. D. Stucky, *Chemistry of Materials* **1998**, *10*, 2033–2036.
- [38] M. Thommes, K. Kaneko, A. V. Neimark, J. P. Olivier, F. Rodriguez-Reinoso, J. Rouquerol, K. S. W. Sing, *Pure and Applied Chemistry* **2015**, *87*.
- [39] Evonik Resource Efficiency GmbH, Aerosil Technical Overview.
- [40] Iolitec GmbH Heilbronn, Technical Reports Ionic Liquids, **2012**.
- [41] S. Zhang, S. Brahim, S. Maat, *Journal of Materials Research* **2018**, *33*, 1179–1188.
- [42] M. Gouverneur, F. Schmidt, M. Schönhoff, *Physical chemistry chemical physics : PCCP* **2018**, *20*, 7470–7478.
- [43] J. Asenbauer, N. B. Hassen, B. D. McCloskey, J. M. Prausnitz, *Electrochimica Acta* **2017**, *247*, 1038–1043.
- [44] T. Nishida, Y. Tashiro, M. Yamamoto, *Journal of Fluorine Chemistry* **2003**, *120*, 135–141.
- [45] A. Platek, J. Piwek, K. Fic, T. Schubert, P. Gentile, G. Bidan, E. Frackowiak, *Journal of Materials Chemistry A* **2017**, *5*, 22708–22716.

Abbreviations and Variables

Abbreviations

EDLC	Electrical Double Layer Capacitor
RTIL	Room Temperature Ionic Liquids
ECW	Electrochemical Stability Window
CV	Cyclic Voltammetry
EMIm	1-Ethyl-3-Methylimidazolium
BMIm	1-Butyl-3-Methylimidazolium
TFSI	Bis-(trifluoromethylsulfonyl)amide
DEME	Diethylmethyl(2-methoxyethyl)ammonium
STM	Scanning Tunneling Microscopy
AFM	Atomic Force Microscopy
OCP	Open Circuit Potential
STC	Salt Templated Carbon
FeTC	FeCl ₃ templated carbon
QSDFE	Quenched-solid Density Functional Theory
NLDFT	Non-linear Density Functional Theory
XRD	Powder X-ray Diffraction
TGA	Thermogravimetric Analysis
ADN	Adiponitrile
TEM	Transmission Electron Microscopy
PSD	Pore Size Distribution

Variables

t/z	time, depends on context	s
T	absolute temperature	K
U	Voltage	V
R	resistance	Ω
C	capacitance	F
R	gas constant	8.3144 J (mol K) ⁻¹
F	Faraday constant	96485 C mol ⁻¹
A	area	m ²
\overline{N}	density of germ nuclei	

Variables

$N = N(t)$	number of germ nuclei at time t	
v'	nonoverlapping volume	
v_{1ex}	extended volume	
V	volume of new phase	
B	growth rate constant	
ΔG	Gibbs free energy, depends on context	J mol ⁻¹
E_F	Fermi energy	eV
E	Electrode potential	V
σ	differential charge density	C cm ⁻²
ϵ_0	permittivity of the vacuum	F m ⁻¹
ϵ	relative permittivity	
d	distance, depends on context	
C	concentration	mol l ⁻¹ , vol%
D	diffusion coefficient	m ² s ⁻¹
I	current	A
J	current density	A g ⁻¹ , A m ⁻²
k	reaction rate constant	s ⁻¹
v	reaction rate	mol (s l) ⁻¹
E^0	standard electrode potential	V
E_{eq}	equilibrium electrode potential	V
n	number of transferred electrons	
ν	scan rate	V s ⁻¹
p/p_0	relative pressure	
C_d	differential capacitance	F g ⁻¹

Eigenständigkeitserklärung

Hiermit versichere ich, dass ich die vorliegende Arbeit selbständig verfasst habe. Ich versichere, dass ich keine anderen als die angegebenen Quellen benutzt und alle wörtlich oder sinngemäß aus anderen Werken übernommenen Aussagen als solche gekennzeichnet habe, und dass die eingereichte Arbeit weder vollständig noch in wesentlichen Teilen Gegenstand eines anderen Prüfungsverfahrens gewesen ist.

Berlin, 24.09.2018

Ort, Datum

Unterzeichner